



Universiteit
Leiden
The Netherlands

Two-photon luminescence of gold nanorods: applications to single-particle tracking and spectroscopy

Carozza, S.

Citation

Carozza, S. (2017, July 4). *Two-photon luminescence of gold nanorods: applications to single-particle tracking and spectroscopy*. *Casimir PhD Series*. Retrieved from <https://hdl.handle.net/1887/50407>

Version: Not Applicable (or Unknown)

License: [Licence agreement concerning inclusion of doctoral thesis in the Institutional Repository of the University of Leiden](#)

Downloaded from: <https://hdl.handle.net/1887/50407>

Note: To cite this publication please use the final published version (if applicable).

Cover Page



Universiteit Leiden



The handle <http://hdl.handle.net/1887/50407> holds various files of this Leiden University dissertation.

Author: Carozza, S.

Title: Two-photon luminescence of gold nanorods: applications to single-particle tracking and spectroscopy

Issue Date: 2017-07-04

Two-Photon Luminescence of Gold Nanorods

Applications to Single-Particle Tracking and Spectroscopy

PROEFSCHRIFT

ter verkrijging van
de graad van Doctor aan de Universiteit Leiden,
op gezag van Rector Magnificus prof. mr. C.J.J.M. Stolker,
volgens besluit van het College voor Promoties
te verdedigen op dinsdag 4 juli 2017
klokke 10.00 uur

door

Sara Carozza

geboren te Bergamo, Italië
in 1987

Promotores: Prof. dr. ir. S. J. T. van Noort
Prof. dr. T. Schmidt

Promotiecommissie: Prof. dr. E. R. Eliel
Prof. dr. M. A. G. J. Orrit
Prof. dr. A. Kros
Prof. dr. W. H. Roos (Rijksuniversiteit Groningen)
Dr. D. M. Heinrich
Dr. M. J. M. Schaaf

©2017 Sara Carozza. All rights reserved.

Casimir PhD Series, Delft-Leiden, 2017-19

ISBN 978-90-8593-303-8

An electronic version of this thesis can be found at

<https://openaccess.leidenuniv.nl>

The work described in this thesis is part of the research programme of the Foundation for Fundamental Research on Matter (FOM), which is part of the Netherlands Organisation for Scientific Research (NWO).

Luminescent gold nanorods in a dark sample resemble stars in the dark sky, and like for stars a map may be used to indicate their unique distribution. The cover and backcover show a constellation map of the Northern hemisphere and one of the Southern hemisphere respectively.

To my parents

CONTENTS

1	Introduction	1
1.1	Single-molecule imaging	2
1.1.1	Probes and labeling	2
1.1.2	Single-molecule microscopy	3
1.2	Two-photon microscopy	5
1.2.1	Principles of two-photon excitation	5
1.2.2	Two-photon microscopes	6
1.2.3	A two-photon multifocal scanning microscope	8
1.3	Metal nanoparticles	12
1.3.1	Surface plasmons, absorption and scattering	12
1.3.2	Gold nanorods	15
1.4	Photoluminescence of gold nanorods	20
1.4.1	One-photon photoluminescence	20
1.4.2	Two-photon photoluminescence	22
1.5	Outline of the thesis	25
2	Accuracy of the detection of binding events using 3D single-particle tracking	33
2.1	Introduction	34
2.2	Materials and methods	36
2.3	Theory	38
2.3.1	Localization accuracy	38
2.3.2	Accuracy of mean square displacement analysis	39
2.3.3	Detection of changes in the diffusion coefficient	41
2.4	Results and discussion	44
2.4.1	Spatial and temporal resolution	44
2.4.2	Factors that determine the uncertainty in the de- tection of the diffusion coefficient	45
2.4.3	Experimental validation of the diffusion coefficient accuracy using gold nanorods in glycerol	46

2.4.4	Detection of changes in diffusion in single particle trajectories	48
2.5	Conclusion	55
2.6	Supplementary figures	57
3	Delivery and single-particle tracking of gold nanorods in live cells	67
3.1	Introduction	68
3.2	Materials and methods	69
3.3	Results	77
3.3.1	Delivery in cells and considerations on cell viability	77
3.3.2	Mobility of gold nanorods in cells	80
3.4	Discussion and conclusion	85
3.5	Supplementary figures	91
4	Functionalization and nuclear targeting of single gold nanorods in live cells	99
4.1	Introduction	100
4.2	Materials and methods	101
4.3	Results	106
4.3.1	Reproducibility of single-cell microinjection	106
4.3.2	Localization of functionalized gold nanorods inside cells	107
4.3.3	Mobility of functionalized gold nanorods	109
4.4	Discussion and conclusion	112
4.5	Supplementary figures	117
5	Two-photon excitation spectroscopy of single gold nanorods with multifocal scanning microscope	131
5.1	Introduction	133
5.2	Materials and methods	134
5.3	Results and discussion	137
5.3.1	Excitation spectra of gold nanorods	137
5.3.2	Characterization of gold nanorod samples with electron microscopy	144
5.3.3	Excitation spectrum of Rhodamine-B	147
5.3.4	Characterization of the setup	148
5.4	Conclusion	151
5.5	Supplementary figures	154

CONTENTS

vii

Summary	159
Samenvatting	165
List of Publications	171
Curriculum Vitae	173
Acknowledgements	175

CHAPTER 1

INTRODUCTION

Imaging single molecules in live cells reveals details of cellular processes that cannot be seen using traditional averaging techniques. A proper choice of the microscope and the labels is essential to get the best results from a single-molecule imaging experiment. In this thesis we used gold nanorods for applications in single-particle imaging, tracking and spectroscopy, using a two-photon multifocal scanning microscope. A two-photon microscope is advantageous due to the possibility to image deep in the sample and the limited photodamage induced in cells by using low-energy photons. As labels, gold nanorods have great potential due to their high brightness and photostability and can be excited in two-photon.

This chapter introduces single-molecule imaging and summarizes the most common labels and microscopes used for these experiments. Then, we present the principles of two-photon excitation and discuss more in detail its advantages over one-photon excitation. We present the structures of a typical two-photon microscope and of the particular two-photon multifocal scanning microscope that we used for our experiments. Finally, we describe noble metal nanoparticles and explain the optical properties that make them such a powerful tool for single-molecule imaging.

1.1 Single-molecule imaging

This section introduces SM imaging experiments and gives a brief overview of the possible labels and imaging techniques to use for these experiments.

Cells are the basic structural and functional unit of all living organisms, and all processes occurring inside and between cells, such as gene replication, growth, diseases and immune defense, are regulated by particular molecules in the cells, mainly proteins and nucleic acids. For a deep understanding of cellular processes, it is necessary to study them at the single molecule level. Following each individual molecule reveals the distribution of all possible behaviors instead of only a population average. This way, intermediate states, rare events and non-synchronized processes within the sample can also be detected. The advantages of SM techniques are particularly valuable in live cells, where large spatial and temporal variations occur.

The first optical detection of a single molecule was achieved by Moerner in 1989, measuring the absorption of pentacene [1]. In 1990, Orrit and Bernard detected the fluorescence signal emitted by single molecules for the first time [2]. These experiments were performed at cryogenic temperatures, where the absorption cross-section of fluorophores increases by several orders of magnitude and the suppression of thermal vibrations makes molecules more stable relative to room temperature. Thanks to new high-sensitivity detectors, such as avalanche photodiodes and charge-coupled devices, the weak signals from single fluorophores could later be detected also at room temperature. In 1995 Funatsu [3] visualized the movement of single proteins *in vitro*. Since then, SM imaging techniques became more and more common, and were for example applied to the study of protein dynamics [4], diffusion in phospholipid membranes [5] and cell signaling [6]. From 2000 SM experiments started to be applied *in vivo*: single receptor proteins were tracked on cells surface [7] and inside living cells [8].

1.1.1 Probes and labeling

As most biomolecules do not fluoresce by themselves, light-emitting probes are used to label and follow the molecules of interest. In live cells

many structures naturally absorb and emit light, giving a high background. An accurate choice of labels and imaging techniques is therefore essential to distinguish the weak signal of single molecules from the background. There are three main classes of probes: fluorescent proteins, organic dyes and fluorescent nanoparticles.

Fluorescent proteins (FPs) [7, 9, 10] present good biocompatibility and labelling specificity, as they can be encoded in the gene corresponding to the target protein. However, they have small optical cross-section and suffer from photobleaching. The performance of fluorescent proteins in SM imaging is thus limited: the weak signal limits the localization precision and photobleaching limits the measurement time.

Organic dyes are smaller than proteins, brighter, and cover a wider spectral range [11]. They are more stable than FPs but also suffer from photobleaching.

Nanoparticles, such as quantum dots (QDs) [12], are the most bright and stable among probes. However, they are larger than FPs and organic dyes and can thus influence the movement of the molecule of interest. In addition, QDs are prone to photoblinking. Noble metal nanoparticles, such as gold and silver nanospheres and nanorods, are brighter than QDs and do not bleach nor blink. Therefore they are a good choice to image molecules in cells with high spatial resolution and for long time.

Labeling proteins with organic dyes and nanoparticles is more challenging than genetic encoding of FPs. First, dyes and nanoparticles must be introduced into the cells using methods such as microinjection, electroporation or incubation. Then they must bind to the target protein. Mediating tags, usually proteins and small peptides, can be encoded in the gene of the target protein, and bind to the label upon expression [13].

Single-molecule techniques using nanoparticles are commonly referred to as single-particle (SP) techniques. In the work presented in this thesis we used gold nanorods for single-particle imaging, tracking and spectroscopy applications. A detailed discussion on gold nanoparticles, gold nanorods and their optical properties is presented in Section 1.3.

1.1.2 Single-molecule microscopy

SM imaging experiments typically use inverted microscopes, in wide-field or confocal configuration. In a wide-field microscope [3, 14] a wide area

of the sample is illuminated. To this aim, an expanded beam is focused on the back focal plane of the objective, resulting in a collimated beam that uniformly illuminates the sample. The fluorescence signal emitted by the sample as well as the reflected excitation light are collected by the same objective and separated by a dichroic mirror before imaging with a CCD (charge-coupled device) or a CMOS (complementary metal-oxide semiconductor) camera. This way, however, a large volume is excited and the fluorescence coming from out-of-focus z planes adds to the in-focus signal, compromising the signal to background.

To reduce the excitation volume, wide-field illumination can be obtained by total internal reflection fluorescence (TIRF) [15]: the excitation beam is focused on the back focal plane of the objective, but off-centered. This results in a slanted excitation beam and when the inclination angle exceeds a critical angle it generates an evanescence wave that decays exponentially from the glass interface. Only a thin slice of the sample (about 250 nm) is excited, avoiding the out-of-focus signal. This technique can be used to image thin samples, but it is not suitable, for example, to image several microns inside cells.

Confocal microscopes limit out-of-focus fluorescence by using a highly focused spot to excite a point inside the sample. The light is collected by the same objective, filtered with a dichroic, and a pinhole is used to reject the out-of-focus signal. Confocal microscopy provides a better signal-to-noise ratio compared to wide-field microscopy, due to the limited excitation volume and the use of avalanche photo-detectors that exhibit less dark counts and a higher quantum yield. It can excite deeper inside the sample, making 3D imaging possible. Nevertheless, the image is acquired only one spot at the time and scanning the excitation beam through the sample significantly slows down the imaging process.

In summary, to investigate cellular processes over extended periods of time and with high accuracy we ideally need small, stable and bright labels and fast 3D microscopes. A compromise must be made between the small but weak and unstable FPs and organic dyes, and bright and stable, large nanoparticles. Likewise, an optimum must be found in terms of 3D penetration, out-of-focus fluorescence and acquisition speed to obtain the highest signal and resolution.

1.2 Two-photon microscopy

1.2.1 Principles of two-photon excitation

For our experiments, we decided to use gold nanorods and a special multifocal two-photon scanning microscope.

The microscopy techniques we presented previously are based on the excitation of fluorescent probes by the absorption of one photon that brings an electron to a higher energy state. After rapid thermal relaxation, the electron falls back to the ground state while emitting a photon with an energy equal to the difference between the two levels minus some relaxation energy (Fig. 1.1a). As the excitation is realized by absorption of one photon at the time, we refer to these techniques as one-photon excitation (OPE) techniques.

Simultaneous absorption of two photons can also induce fluorescence excitation. The electron excitation occurs by absorption of two photons whose combined energy equals the energy gap between the ground state and the excited state. This process is called two-photon excitation (TPE). The absorption of the two individual photons must occur within about 0.5 fs [16]. After excitation, the electron follows the same decay pathway as in OPE (Fig. 1.1b).

Using TPE has several advantages over OPE [17]. The excitation wavelength shifts from the visible region in the spectrum to the near infrared (nIR), because both photons carry half the energy. Larger wavelength photons are preferable for *in vivo* imaging, because they are absorbed less by cells and tissues and thus induce less photodamage. The lower absorption of photons by the sample allows for two to up to ten time deeper penetration in the sample than OPE [18, 19]. Moreover, there is a larger spectral gap between the excitation and emission wavelengths than in OPE and the two can better be separated, resulting in a weaker background signal. Another advantage of TPE is that the fluorescence signal scales with the square of the excitation intensity. As a consequence, the absorption is better confined (Fig. 1.2a) and out-of-focus absorption and fluorescence are strongly reduced (Fig. 1.2b). This yields an improvement in signal-to-noise ratio and sectioning in the z direction.

However, the TP absorption cross-section of fluorophores is far smaller

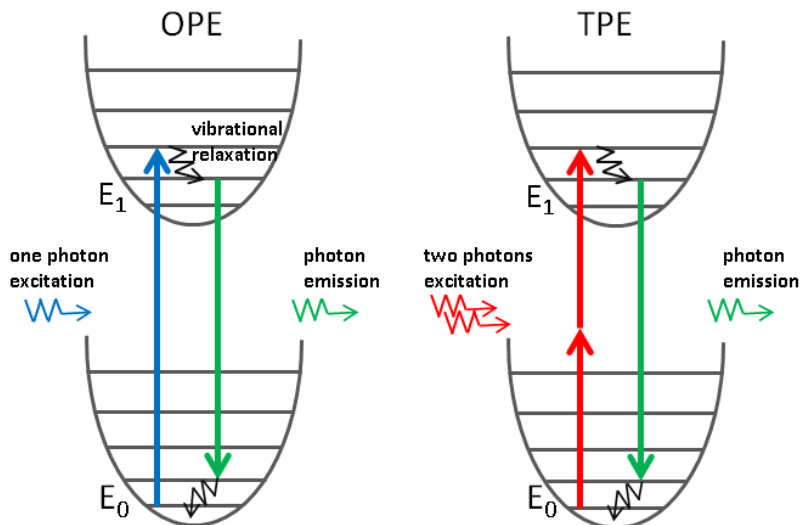


Figure 1.1

Jablonsky diagram for a) one-photon and b) two-photon fluorescence, showing the electronic states of a molecule and the transitions triggered by the excitation. The electronic levels of the molecules (E_0 = ground state, E_1 = first excited state) are represented as wells containing vibrational sub-levels.

than their OP cross-section and a high density of photons in short time is required for the excitation. As a result, photobleaching is more severe than in OPE [22]. As discussed in section 1.3, this is not limiting when metal nanoparticles are used.

1.2.2 Two-photon microscopes

To generate the high density of photons in short time that is required for TPE, titanium-sapphire (Ti-Sa) lasers are typically used. Ti-Sa lasers generate 100 fs pulse trains with wavelengths from 700 to 1000 nm at a rate of about 100 MHz [23].

Besides the nIR excitation source, a TP microscope is similar to a typical confocal microscope [17, 21], though the non-linear response alleviates the need for using a pinhole. Fig. 1.3 shows the typical scheme of a TP microscope. The beam diameter is increased using a telescope, and the light intensity can be controlled using a $\lambda/2$ plate and a polar-

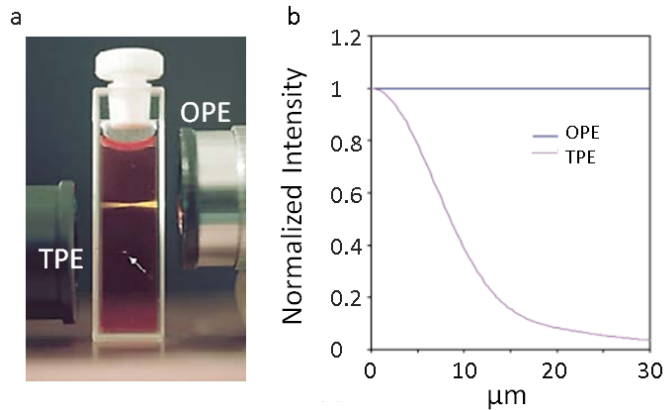


Figure 1.2

Comparison between the excitation profile and the out-of-focus fluorescence in one-photon and two-photon excitation. a) OPE and TPE excitation profiles in a fluorescent solution: while the OPE profile forms a line throughout the cuvet, the fluorescence of TPE occurs only within a small spot, indicated by the arrow. The picture is from [20]. b) Calculated fluorescence at different distances from the focal plane using an objective with numerical aperture = 0.1: within 10 μm the TP fluorescence decreases to 40%, while OP fluorescence hardly changes over several tens of microns. The figure is from [21].

izer, or grey filters. The beam is then scanned using a scanning mirror actuated by a piezo scanner. A scan lens converts the beam deflection into x-y movement. The scan lens is coupled to a second lens to adjust the beam size and direct it to the back aperture of the objective. When performing 3D imaging, a piezo stage is used to move the objective in the z direction. Alternatively the sample can be scanned by adjusting the focus. A dichroic mirror filters the reflected excitation light and directs the fluorescence to the detector.

For high resolution and high sensitivity, objectives with high numerical aperture (NA) are preferred. Higher NAs optimize the excitation efficiency by collecting light from a wider angle and confining the intensity to a smaller excitation volume. The optics used in a TP setup must be optimized for high power nIR light.

Though TP microscopes provide higher signal-to-noise ratio, deeper penetration into the sample, better 3D sectioning and less photodamage

compared to OP microscopes, a drawback common to both TP and OP confocal microscopes is the long acquisition time due to the sequential scanning.

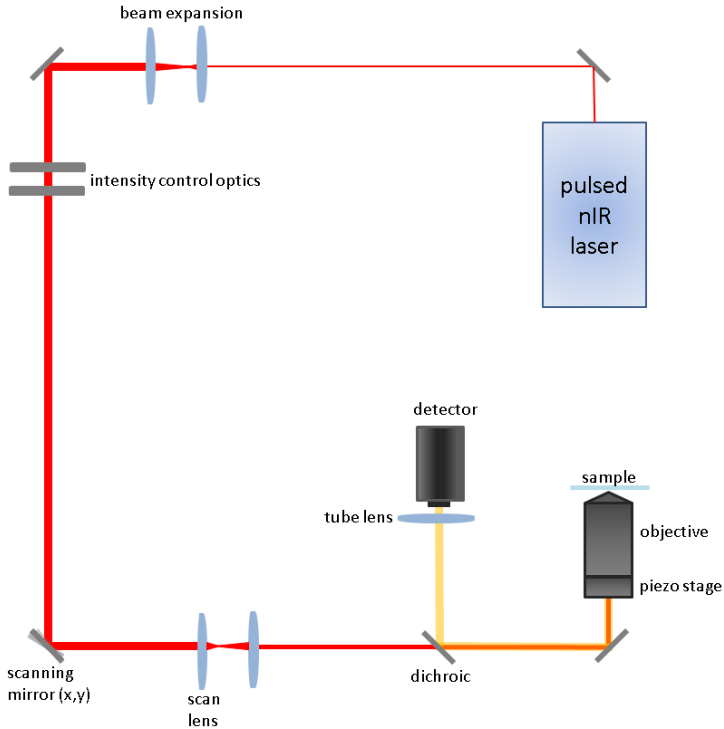


Figure 1.3
Basic scheme of a typical TP scanning microscope.

1.2.3 A two-photon multifocal scanning microscope

A way to reduce the acquisition time in a scanning microscope is to excite multiple foci in parallel. The first multifocal configuration was realized by Buist et al. [24] using a microlens array to create a 2D array of equidistant, diffraction-limited spots. However, the spots generated by microlenses in different parts of the array did not all have the same

intensity, resulting in a heterogeneous excitation pattern. A diffractive optical element (DOE) is a better solution, being able to generate a grid of spots of equal intensity [25].

For the experiments presented in this thesis we therefore used a two-photon multifocal scanning microscope exploiting a DOE. A scheme of the setup is shown in Fig. 1.4. This setup was presented previously by Van den Broek et al [26]. We made few modifications to the original scheme.

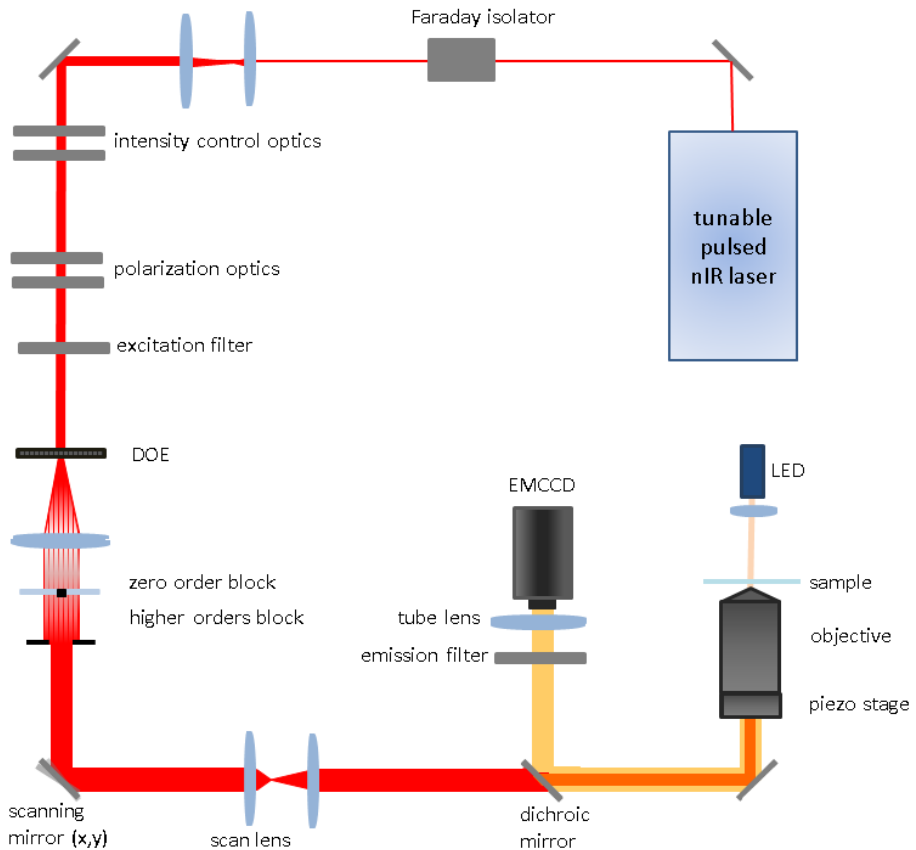


Figure 1.4
Scheme of a two-photon multifocal scanning microscope.

The excitation source is a Ti-Sa laser (Chameleon Ultra, Coherent, USA) with a pulse width of 140 fs at a rate of 80 MHz; the beam wavelength is automatically tunable in the range 690-1020 nm. A Faraday optical isolator (Broadband Faraday isolator, Newport, USA) prevents back-reflections from entering in the laser cavity. After expanding the beam with two lenses, the intensity is controlled by a $\lambda/2$ plate (WPH05M, Thorlabs, USA) and a beam splitter cube. Grey filters (NDA units, Thorlabs, USA) are used to further reduce the beam power. The diffractive optical element (custom-made by Holoeye Photonics, Germany) generates a 25x25 hexagonal array of focal spots. The beam is then collimated and sent through a glass coverslip, on to which a drop of solder alloy was deposited to block the zero order of the diffraction pattern. Orders of diffraction higher than the first one are filtered using a diaphragm. A $\lambda/4$ plate (WPQ05M, Thorlabs, USA) is used to convert the polarization of the light from linear to circular. A fast steering mirror (FSM-300, Newport) deflects the beam in two directions. The deflections are then converted to movements in the x and y plane by a scan lens. The beam is then expanded to fill the back aperture of the objective (Apo TIRF 60x, NA = 1.49, oil immersion, Nikon, Japan). A piezo-actuator (P-726, Pifoc, PI, Germany) moves the objective in the z direction to acquire 3D images. The sample is placed on an XY stage (PKTM50, Owis, Germany) driven by a stepper motor board (TMCM-610, Trinamic, Germany). A white light LED is used to obtain transmission images of the sample. The fluorescence light emitted by the sample is collected by the objective and deflected by a dichroic mirror (700dextr, Chroma, USA) to an electron-multiplier-charged-coupled-device (EMCCD) camera (QuantEM 512SC, Photometrics, USA). An excitation filter (692LP, Semrock, USA) is placed before the dichroic, to block the residual visible light from the laser excitation. An emission filter (720SP, Semrock, USA) is placed before the tube lens, to block the residual excitation and scattering light. All the mirrors, filters and polarizers in the setup are optimized for high power nIR light.

The size of a pixel in the images acquired with this setup is 0.175 μm . The array of focal spots produced by the DOE (Fig. 1.5a) covers an area of approximately 350 x 350 pixels on the image, corresponding to about 60 μm x 60 μm . The distance between adjacent focal spots is approximately 17 pixels (about 3 μm). To obtain a homogeneous illumi-

nation of the sample, the scanning mirror is driven by an Archimedean spiral function, such that every focal spot develops into a 2D Gaussian profile. Scanning such a pattern was proven to provide the most homogeneous excitation pattern as compared to stochastic and raster scanning [26] (Fig. 1.6). The mirror scanner is synchronized with the camera exposure, to perform a complete spiral cycle within a single exposure (typically 50-100 ms). In the two directions, the Archimedean spiral function sent to the scanner is:

$$x = A\tau \sin(2\pi n\tau) \quad (1.1)$$

$$y = A\tau \cos(2\pi n\tau) \quad (1.2)$$

$$\tau = \sqrt{\frac{t}{T} \exp\left(\frac{(t/T)^2}{2\sigma^2}\right)} \quad (1.3)$$

where A is the amplitude of the scanning signal, n is the number of spiral branches, σ is the width of the Gaussian profile, and T is the exposure time of the camera. A homogenous excitation profile is obtained if the neighboring focal spots sufficiently overlap when scanned [26]. We obtained the most homogeneous excitation pattern using $A = 2 \mu\text{m}$, $\sigma = 1.4 \mu\text{m}$ and $n = 12$. The pattern obtained is shown in Fig. 1.5b.

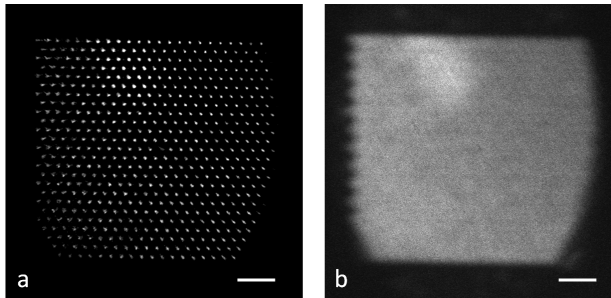


Figure 1.5

a) The 25x25 focal spots array generated by the DOE in our setup and b) the excitation profile obtained by scanning the array. The images are produced by reflecting the excitation beam with a mirror placed on the sample stage. The bottom right corner of the pattern is cut off along the beam path, due to the limited size of one of the mirrors. The bars in the images correspond to $10 \mu\text{m}$.

The mirror scanner, the camera, the piezo actuator and the LED are connected to a data acquisition (DAQ) card (USB-6229, National Instrument, USA) that communicates between the computer and the devices. A LabVIEW program is used to synchronize the devices and acquire images.

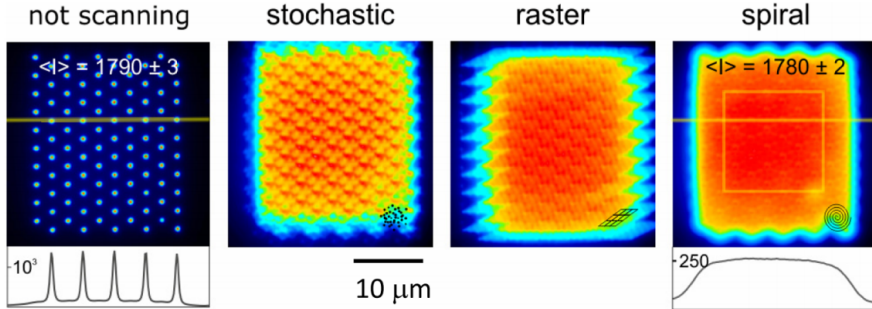


Figure 1.6

Comparison between stochastic, raster and spiral scanning. The image is from [26], where a 10×10 DOE was used to generate a grid of focal spots. Spiral scanning provides the most homogeneous distribution of the intensity.

1.3 Metal nanoparticles

In the first section of this chapter we presented the possible labels for SM imaging experiments: fluorescent proteins, organic dyes and nanoparticles. For our experiments we chose a particular kind of nanoparticles: gold nanorods. Here we discuss the optical properties that make metal nanoparticles in general, and gold nanorods in particular, so advantageous for SM imaging.

1.3.1 Surface plasmons, absorption and scattering

When a noble metal particle is irradiated by an external electric field, a collective oscillation of the free conduction electrons on the surface is generated. This oscillation is called surface plasmon (SP). During

the oscillation, the electron cloud moves away from the nuclei in the lattice, and a restoring force is generated by the Coulomb interactions between the nuclei and the displaced electrons (Fig 1.7a). Plasmons are therefore dipole oscillations. Multipole oscillations can also occur, such as quadrupole oscillations: one half of the electrons moves parallel to the excitation field and the other half moves antiparallel [27].

The plasmon excitation decays through a non-radiative or radiative pathway. Non-radiative pathways include energy transfer to the lattice or to the environment. Radiative decay occurs by recombination of the electrons with the holes in the lattice, with consequent emission of photons. The probability of radiative decay is low, due to the high efficiency of the non-radiative processes.

As opposed to fluorescent proteins and dyes, in metal nanoparticles all the surface electrons participate in the plasmonic oscillation. This makes the extinction (absorption + scattering) cross-section very large. The absorption and scattering cross sections of metal nanoparticles can be up to respectively 5-6 and 4-5 orders of magnitude larger than the cross-sections of organic dyes [28, 29]. In addition, noble metals do not react with the environment, resulting in a more stable signal compared to the signal from organic dyes and fluorescent proteins. Therefore, bleaching and blinking are generally not an issue when using these nanoparticles as labels.

A theoretical description of surface plasmons was presented by Mie [30, 31]. Solving the Maxwell equations to calculate the scattering produced by an irradiated sphere, he obtained a field that can be approximated by a dipole. This dipole is the plasmon oscillation. The dipole approximation is valid when the particle is much smaller than the wavelength of the incident light, like in case of nanoparticles.

The polarizability of a spherical metal particle is:

$$\alpha = 4\pi r^3 \epsilon_0 \frac{\epsilon_\lambda - \epsilon_0}{\epsilon_\lambda + 2\epsilon_0} \quad (1.4)$$

where r is the radius of the particle, ϵ_0 the dielectric constant of the medium and ϵ_λ the dielectric constant of the particle that depends on the wavelength of the incoming light λ . For $\epsilon_\lambda = -2\epsilon_0$ the polarizability is maximal and a resonant dipole oscillation is established in the particle. This condition is referred to as surface plasmon resonance (SPR) and is satisfied for a particular wavelength value. For gold spheres, the

SPR wavelength is around 520 nm (Fig. 1.7b). In Mie's approximation the SPR is independent from the particle size. Experimentally, a weak dependence of the SPR on the size of a gold sphere was found [32, 33] (Fig. 1.8).

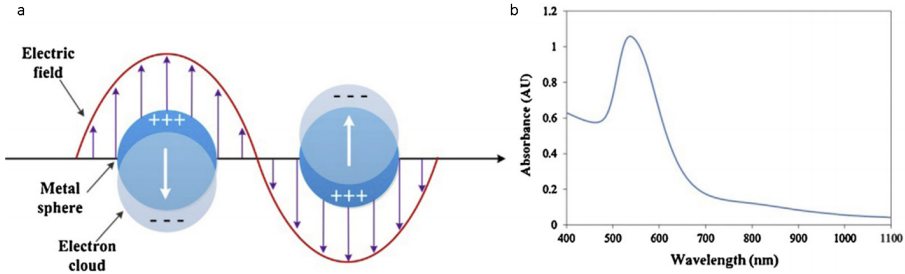


Figure 1.7

Surface plasmon resonance in a metal nanosphere. a) The plasmons enhance the absorption cross-section, resulting in a peak in the absorption spectrum (shown in b) at the plasmon resonance wavelength. The figure is from [32].

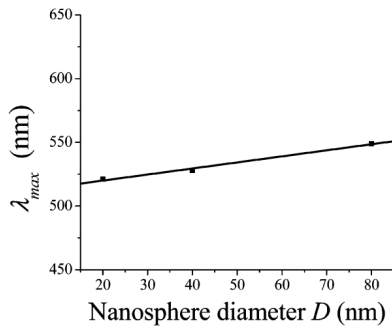


Figure 1.8

Dependence of the plasmon resonance peak on the sphere size. The figure is from [33].

The absorption and the scattering cross sections of the particle are functions of the polarizability [34]:

$$\sigma_{ext} = \sigma_{scat} + \sigma_{abs} \quad (1.5)$$

$$\sigma_{scat} = \left(\frac{2\pi}{\lambda}\right)^4 \frac{|\alpha^2|}{6\pi} \quad (1.6)$$

$$\sigma_{abs} = \frac{2\pi}{\lambda} \text{Im}(\alpha) \quad (1.7)$$

which has a maximum in the resonance condition (see Eq. 1.4). Consequently, the absorption and scattering spectra feature a peak at the SPR energy (Fig. 1.7b).

Combining Eq. 1.4 with Eq. 1.6, 1.7 shows the dependence of absorption and scattering cross-section from the size of the particle. As the particle size increases, the contribution of scattering in the extinction cross-section becomes dominant. Smaller particles are thus more suitable for applications involving absorption, while bigger particles are used for scattering applications [34].

The dipole approximation presented here is valid for particles smaller than about 50 nm. For larger particles the external electric field cannot be considered constant and the contribution of higher modes of oscillation increases [35].

1.3.2 Gold nanorods

Among noble metal nanoparticles, gold nanoparticles are easy to synthesize and conjugate to biomolecules and present low toxicity due to the lower reactivity and lower release of free ions compared to silver and copper nanoparticles [32, 33].

Among gold nanoparticles, gold nanorods (GNRs) are commonly used. The synthesis of GNRs is well established and they present some advantages over nanospheres. Nanorods have two different plasmon oscillation modes: a longitudinal one and a transversal one. The transversal mode, corresponding to the oscillations of electrons in the direction of the two shorter axes, has the same energy as the plasmon of a nanosphere. The longitudinal plasmon, corresponding to the electronic oscillation in the direction of the longer axis of the rod, appears at higher wavelengths (Fig. 1.9).

The optical properties of gold nanorods were derived by Gans, using a version of Mie's theory that approximates rods to prolate ellipsoids.

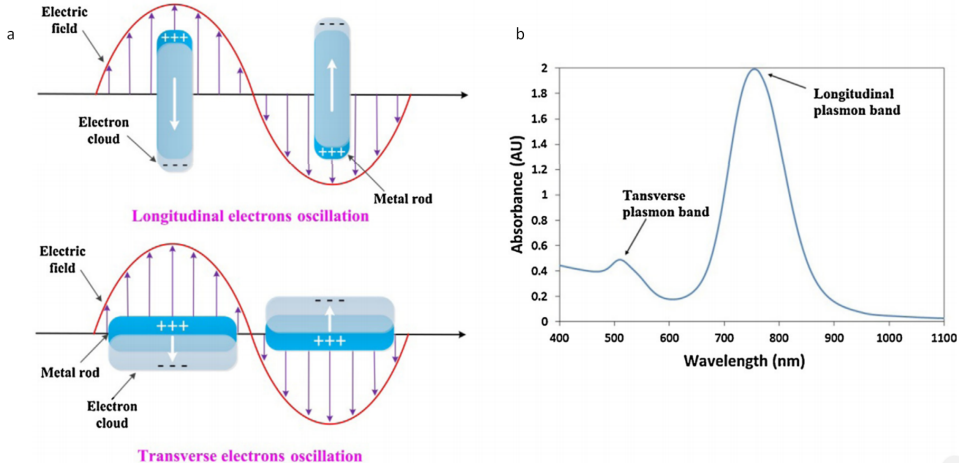


Figure 1.9

a) Surface plasmon resonance in a nanorod: the longitudinal and transversal electron oscillations in the particle generate two peaks in the absorption spectrum (shown in b)). The figure is from [33].

In Gans's calculation, the polarizability of an ellipsoid under irradiation parallel to one of its axes i is [36, 37]:

$$\alpha_i = 4\pi V \frac{\epsilon_\lambda - \epsilon_0}{\epsilon_0 + L_i(\epsilon_\lambda - \epsilon_0)} \quad (1.8)$$

where V is the volume of the particle and L_i are the depolarization factors for each axis (for the spherical case, $L_i = 1/3$). Defining a as the longer axis and $b=c$ the shorter axes, L_i are defined as:

$$L_a = \frac{2}{R^2 - 1} \left(\frac{R}{R^2 - 1} \ln \frac{R + \sqrt{R^2 - 1}}{R - \sqrt{R^2 - 1}} - 1 \right) \quad (1.9)$$

$$L_{b,c} = \frac{1 - L_a}{2} \quad (1.10)$$

L_a is the depolarization along the long axis, and $L_{b,c}$ are the depolarizations along the two short axes; R is the aspect ratio of the particle, defined as a/b . Combining Eq. 1.8 with Eq. 1.9 and 1.10 shows that the polarization in a nanorod depends not only on the dielectric constants of the particle and of the medium, but also on the aspect ratio of the

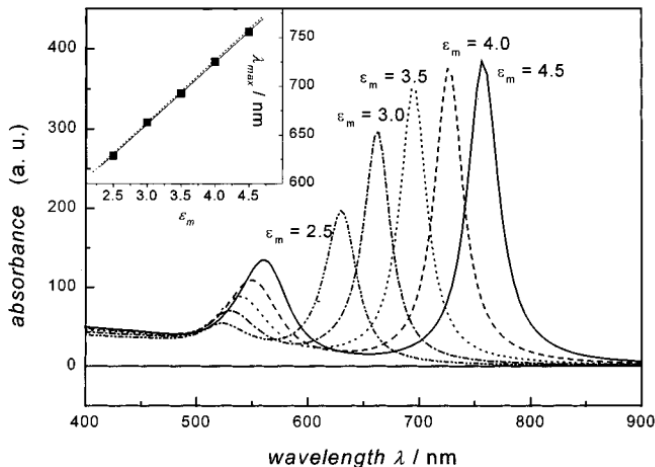


Figure 1.10

Dependence of the absorption peaks of nanorods from the dielectric constant of the environment. A linear dependence (inset) is obtained for the longitudinal peak. The figure is from [39].

particle.

The absorption and scattering cross-sections of rods are [38]:

$$\sigma_{abs} = \frac{2\pi}{3\lambda} V \epsilon_0^{3/2} \sum_i \frac{\frac{\text{Im}(\epsilon)}{L_i^2}}{\text{Re}(\epsilon) + \epsilon_0 \frac{1-L_i}{L_i} + \text{Re}(\epsilon)^2} \quad (1.11)$$

$$\sigma_{scat} = \frac{8\pi^3}{9\lambda^4} V^2 \epsilon_0^2 \sum_i \frac{\frac{\text{Re}(\epsilon) - \epsilon_0^2 + \text{Im}(\epsilon)^2}{L_i^2}}{\text{Re}(\epsilon) + \epsilon_0 \frac{1-L_i}{L_i} + \text{Im}(\epsilon)^2} \quad (1.12)$$

Due to the resonance condition, the absorption and scattering cross-sections depend on the dielectric constant of the particle and of the medium (Fig. 1.10).

Having a larger polarizability, the longitudinal plasmon presents a stronger dependence on the size of the GNR, while the transversal plasmon is only weakly dependent on the particle shape, as in the case of nanospheres. In particular, the resonant wavelength of the longitudinal plasmon red-shifts for increasing aspect ratios [39] (Fig. 1.11a). It is

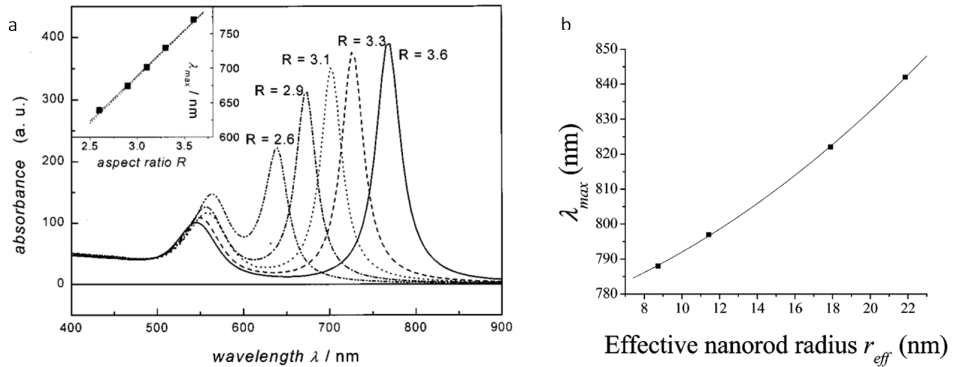


Figure 1.11

Dependence of the longitudinal peak on the shape and size of the GNR. a) Red shift of the longitudinal plasmon wavelength for increasing aspect ratios. The dependence is linear (inset). The figure is from [39]. b) Absorption peak for nanorods with different effective radius, at constant aspect ratio $R = 3.9$. The figure is from [33].

thus possible to synthesize nanorods with a range of longitudinal plasmon wavelengths by tuning their aspect ratio, up to the nIR region of the light spectrum. In this region, especially within the 650-1350 nm window, the damage caused by light in tissues is minimized, making gold nanoparticles very useful for biological applications [31].

The dependence of the longitudinal mode on the volume of the particle is stronger than in nanospheres: this dependence can be expressed in terms of GNR effective radius, defined as the radius of a sphere with equivalent volume (Fig. 1.11b). The longitudinal plasmon exhibits also a stronger dependence on the dielectric constant of the particle and the environment, making gold nanorods useful for sensing purposes.

A final advantage of nanorods over nanospheres is the dependence of absorption and emission on the polarization of the light. It is then possible to detect different orientation of the nanorods and study rotational dynamics. While the spectrum of a nanosphere is independent from the polarization of the excitation light, the scattering spectrum of GNRs shows a \cos^2 dependence (Fig. 1.12).

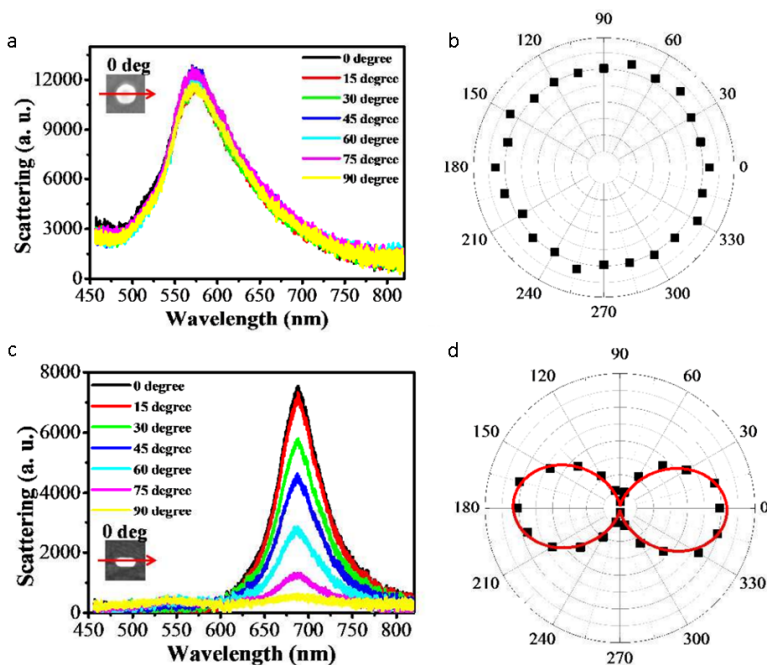


Figure 1.12

Scattering spectra of a) a nanosphere and b) a nanorod excited under light with varying polarization. The scattering intensity exhibits no dependence on the polarization in case of nanospheres, and a \cos^2 dependence in case of nanorods. The image is from [40].

Similarly to nanospheres, scattering dominates for larger nanorods and absorption for smaller ones [41] (Fig. 1.13). Therefore larger GNRs may be more suitable for imaging experiments, while small ones are preferred for applications using absorption and heating [42]. In our experiments, we chose gold nanorods with sizes ranging from about 40 nm x 10 nm to 60 nm x 20 nm. This size may be rather large for applications in which a single protein is labeled and tracked in a cell. Moreover, in such a crowded environment a large size leads to an increased possibility of getting stuck as compared to smaller particles. However, nanorods of this size provide an exceptional brightness and consequently very high localization accuracy inside the cell.

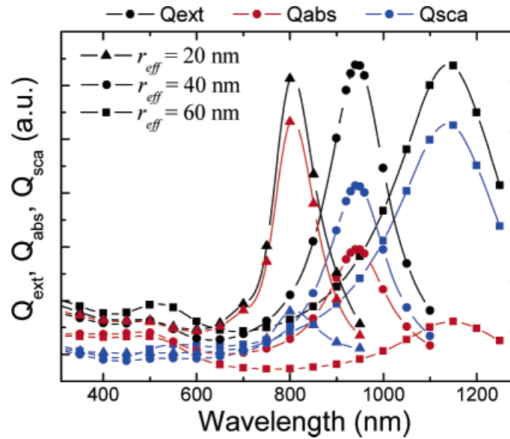


Figure 1.13

The relative contribution of absorption and scattering to the extinction cross-section depends on the GNR size. The figure is from [41].

1.4 Photoluminescence of gold nanorods

1.4.1 One-photon photoluminescence

In our experiments we image gold nanorods taking advantage of their two-photon photoluminescence. In this section we discuss the origin of the photoluminescence of gold nanoparticles, both in one-photon and in two-photon.

Bulk gold exhibits a weak photoluminescence, that can be explained as the result of a three-steps process [43]:

1. Upon light irradiation, the electrons in the d band are excited and migrate to the sp or d conduction band, generating electron-hole couples.
2. The electrons relax, losing energy via scattering with other electrons or phonons

3. The excited electrons can recombine with holes in the d band, causing emission of photons.

The energy levels in metals are more closely spaced than in molecules, and excited electrons can relax till the lowest energy above the Fermi level. The relaxation processes are faster than electron-pair recombinations, hence the low quantum yield of gold (about 10^{-10}). However, an enhancement by several orders of magnitudes is obtained by increasing the surface roughness of the metal [44]. This enhancement is due to the "lighting-rod effect": a rough surface has protrusions where the electron motions gets confined, establishing local surface plasmons. This also occurs in nanoparticles [45]: in gold nanorods an increase in quantum yield of a million times was observed, compared to bulk gold. Surface plasmons enhance both the recombination rate between electrons and holes and the photon emission, resulting in increased absorption and luminescence efficiency [46]. Therefore, the photoluminescence process in metal nanoparticles, though excited at any energy, is strongly enhanced by SPR [47]. As a consequence, the photoluminescence spectrum overlaps with the scattering and absorption spectrum [48], as shown in Fig. 1.14.

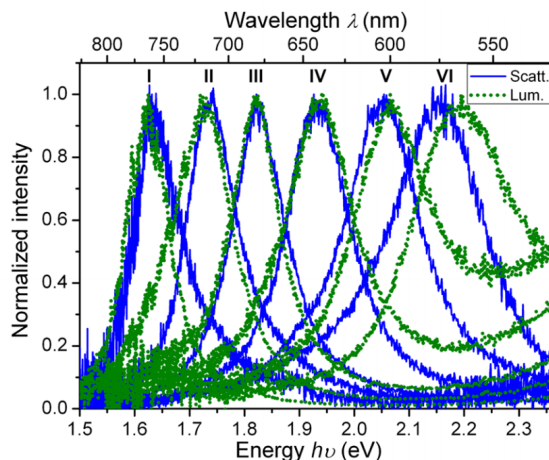


Figure 1.14

Correlation between the scattering (blue continuous line) and one photon luminescence spectrum (green dotted line) of GNRs with different aspect ratios. The figure is from [48].

The same dependence on the aspect ratio of the rods and on the dielectric constant of the environment has been reported [45, 46].

In GNRs, the luminescence quantum yield is weakly dependent on the volume. In large rods a slight decrease of the quantum efficiency was observed and was explained by partial reabsorption of the radiation by the particles [48].

1.4.2 Two-photon photoluminescence

In addition to one-photon luminescence, gold nanorods exhibit strong two-photon photoluminescence (TPPL). This phenomenon can be explained as a process involving two sequential one-photon steps [49–51] (Fig. 1.15):

1. Upon light excitation, the first photon excites an intraband transition within the sp band, from below to above the Fermi level, creating a hole.
2. The second photon excites an electron in the d band to recombine with the sp hole left from the first excitation, creating a second hole in the d band. The excited electron in the sp band can now recombine with the hole in the d band, emitting a photon.

Therefore, similar to one-photon luminescence, TPPL is also enhanced by SPR. The TPPL spectrum overlaps with the OP and scattering spectrum (Fig 1.16, [52]) and depends on the aspect ratio of the nanorod and on the dielectric constant of the medium.

TPPL exhibits a quadratic dependence on the excitation intensity, resulting in a narrower TP spectrum than the scattering spectrum (Fig. 1.17a). In sensing applications, it is important to precisely localize the peak in the spectrum of a GNR, to be able to detect small variations in its position due for example to the interaction with a molecule. Using TP spectra can thus be advantageous over OP and scattering spectra.

As a consequence of quadratic dependence on the excitation, TPPL is proportional to the \cos^4 of the polarization of the excitation light (Fig. 1.17b).

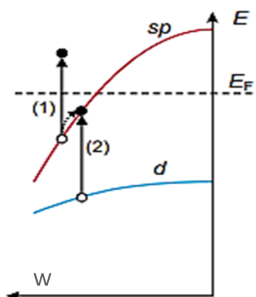


Figure 1.15

TPPL excitation process in GNRs. Excitation of one electron from the sp band to above the Fermi level and excitation of another electron from the d band to the sp band. The x and y axes indicate the wave number and the energy of the electronic levels. The figure is from [51].

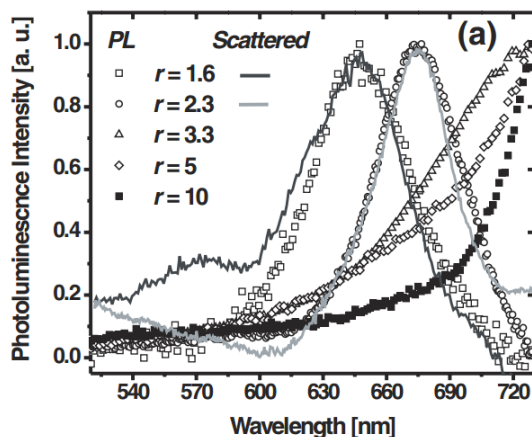


Figure 1.16

Correlation between the scattering (lines) and the TPPL spectra (dots) for GNRs with different aspect ratios. The figure is from [52].

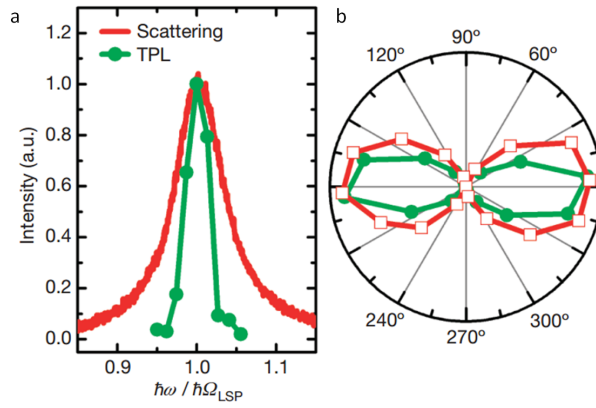


Figure 1.17

a) Comparison between the scattering (red line) and the TPPL spectrum (green dots and line) of a gold nanorod and b) dependence of their intensities from the polarization of the incident light. The figure is from [53].

1.5 Outline of the thesis

In this thesis we applied the two-photon photoluminescence of gold nano-rods in single-particle tracking and spectroscopy experiments, using a multifocal scanning microscope.

In **Chapter 2** we characterized the accuracy of our microscope in localizing GNRs and detecting their diffusion. The precision of single-particle tracking results depends on the features of the setup and the stochasticity intrinsic to diffusion. Using simulations and experiments *in vitro*, we adjusted the parameters used in mean squared displacement analysis to obtain the most accurate measure of diffusion. We applied the analysis to the detection of temporal changes in the simulated diffusion of a GNR, mimicking a transient binding process as it can occur between a protein and a cellular structure. The results show how the detection of the event depends on the mobility of the ligands and of the duration of the binding event.

In **Chapter 3** we explored the use of GNRs for single-particle tracking in living cells. We first tested different delivery techniques in three different cell types. For each delivery technique we evaluated the delivery efficiency and the short-term effect on cell viability. We then analyzed the mobility of the GNRs delivered with each method. We observed immobile GNRs, freely diffusing GNRs and GNRs diffusing within confined areas inside the cells. The quantification of mobility parameters yielded similar results for GNRs delivered with all successful techniques, though delivery efficiency and cell viability varied. Interestingly, GNRs showed a similar mobility in the cytoplasm and in the nucleus of cells.

The final goal of single-particle tracking of GNRs is to follow biomolecules inside cells. To this aim, they need to be specifically functionalized. As described in **Chapter 4**, we functionalized GNRs with nuclear localization signal peptides which induce nuclear targeting. We analyzed the localization of the GNRs inside the cell, and quantified the efficiency of nuclear targeting of functionalized GNRs as compared to GNRs without the peptides. We obtained a low nuclear delivery efficiency that we attributed to the large size of the GNRs used for the experiment. We then analyzed the mobility of functionalized GNRs, that yielded similar results to the ones obtained previously with non-functionalized GNRs.

In **Chapter 5** we explored the use of GNRs for spectroscopy applications. Our setup allows for fast tuning of the laser wavelength, and can be used to acquire two-photon excitation spectra of many GNRs in parallel. The spectra we obtained showed unexpected features, not compatible with single GNRs. We tested several hypotheses to explain the origin of such spectra, and pinpointed the elements in the setup which may underlie the modulation in the signal. We could not perform sensing experiments yet, but the experiments we presented were a necessary step towards the acquisition of TP spectra of single gold nanorods with our setup.

BIBLIOGRAPHY

- [1] WE Moerner and L Kador. “Optical detection and spectroscopy of single molecules in a solid.” In: *Physical review letters* 62.21 (May 1989), pp. 2535–2538. ISSN: 1079-7114.
- [2] M Orrit and J Bernard. “Single pentacene molecules detected by fluorescence excitation in a p-terphenyl crystal.” In: *Physical review letters* 65.21 (Nov. 1990), pp. 2716–2719. ISSN: 1079-7114.
- [3] T Funatsu et al. “Imaging of single fluorescent molecules and individual ATP turnovers by single myosin molecules in aqueous solution.” In: *Nature* 374.6522 (Apr. 1995), pp. 555–9. ISSN: 0028-0836.
- [4] S Weiss. “Measuring conformational dynamics of biomolecules by single molecule fluorescence spectroscopy.” eng. In: *Nature structural biology* 7.9 (Sept. 2000), pp. 724–9. ISSN: 1072-8368.
- [5] G J Schutz et al. “Properties of lipid microdomains in a muscle cell membrane visualized by single molecule microscopy.” In: *The EMBO journal* 19.5 (Mar. 2000), pp. 892–901. ISSN: 0261-4189.
- [6] Akihiko Ishijima and Toshio Yanagida. “Single molecule nanobio-science”. In: *Trends in Biochemical Sciences* 26.7 (July 2001), pp. 438–444. ISSN: 09680004.
- [7] Y Sako, S Minoghchi, and T Yanagida. “Single-molecule imaging of EGFR signalling on the surface of living cells.” In: *Nature cell biology* 2.3 (Mar. 2000), pp. 168–72. ISSN: 1465-7392.
- [8] Hideji Murakoshi et al. “Single-molecule imaging analysis of Ras activation in living cells.” In: *Proceedings of the National Academy of Sciences of the United States of America* 101.19 (May 2004), pp. 7317–22. ISSN: 0027-8424.
- [9] Adam D Douglass and Ronald D Vale. “Single-molecule imaging of fluorescent proteins.” In: *Methods in cell biology* 85 (Jan. 2008), pp. 113–25. ISSN: 0091-679X.

- [10] G S Harms et al. "Autofluorescent proteins in single-molecule research: applications to live cell imaging microscopy." In: *Biophysical journal* 80.5 (May 2001), pp. 2396–408. ISSN: 0006-3495.
- [11] M Sameiro T Gonçalves. "Fluorescent labeling of biomolecules with organic probes." In: *Chemical reviews* 109.1 (Jan. 2009), pp. 190–212. ISSN: 1520-6890.
- [12] Ute Resch-Genger et al. "Quantum dots versus organic dyes as fluorescent labels." In: *Nature methods* 5.9 (Sept. 2008), pp. 763–75. ISSN: 1548-7091.
- [13] Irwin Chen and Alice Y Ting. "Site-specific labeling of proteins with small molecules in live cells." In: *Current opinion in biotechnology* 16.1 (Feb. 2005), pp. 35–40. ISSN: 0958-1669.
- [14] I Sase et al. "Real time imaging of single fluorophores on moving actin with an epifluorescence microscope." In: *Biophysical journal* 69.2 (Aug. 1995), pp. 323–8. ISSN: 0006-3495.
- [15] V Hlady, D.R Reinecke, and J.D Andrade. "Fluorescence of adsorbed protein layers". In: *Journal of Colloid and Interface Science* 111.2 (June 1986), pp. 555–569. ISSN: 00219797.
- [16] Fritjof Helmchen and Winfried Denk. "Deep tissue two-photon microscopy". In: 2.12 (2005).
- [17] W Denk, J. Strickler, and W. Webb. "Two-photon laser scanning fluorescence microscopy". In: *Science* 248.4951 (Apr. 1990), pp. 73–76. ISSN: 0036-8075.
- [18] V E Centonze and J G White. "Multiphoton excitation provides optical sections from deeper within scattering specimens than confocal imaging." In: *Biophysical journal* 75.4 (Oct. 1998), pp. 2015–24. ISSN: 0006-3495.
- [19] Patrick Theer, Mazahir T. Hasan, and Winfried Denk. "Two-photon imaging to a depth of 1000 um in living brains by use of a Ti:Al₂O₃ regenerative amplifier". EN. In: *Optics Letters* 28.12 (June 2003), p. 1022. ISSN: 0146-9592.
- [20] Alberto Diaspro, Giuseppe Chirico, and Maddalena Collini. "Two-photon fluorescence excitation and related techniques in biological microscopy." English. In: *Quarterly reviews of biophysics* 38.2 (May 2005), pp. 97–166. ISSN: 0033-5835.

-
- [21] Peter T C So et al. "Two-Photon Excitation Fluorescence Microscopy". In: (2000), pp. 399–429.
- [22] G H Patterson and D W Piston. "Photobleaching in two-photon excitation microscopy." In: *Biophysical journal* 78.4 (Apr. 2000), pp. 2159–62. ISSN: 0006-3495.
- [23] Joon Myong Song et al. "Determination of Two Photon Absorption Cross Section of Fluorescein Using a Mode Locked Titanium Sapphire Laser." In: *Analytical Sciences* 15.6 (1999), pp. 601–603. ISSN: 0910-6340.
- [24] Buist et al. "Real time two-photon absorption microscopy using multi point excitation". In: *Journal of Microscopy* 192.2 (Nov. 1998), pp. 217–226. ISSN: 0022-2720.
- [25] L. Sacconi et al. "Multiphoton multifocal microscopy exploiting a diffractive optical element". EN. In: *Optics Letters* 28.20 (Oct. 2003), p. 1918. ISSN: 0146-9592.
- [26] Bram van den Broek et al. "Parallel nanometric 3D tracking of intracellular gold nanorods using multifocal two-photon microscopy." In: *Nano letters* 13.3 (Mar. 2013), pp. 980–6. ISSN: 1530-6992.
- [27] K. Lance Kelly et al. "The Optical Properties of Metal Nanoparticles: The Influence of Size, Shape, and Dielectric Environment". In: *The Journal of Physical Chemistry B* 107.3 (Jan. 2003), pp. 668–677. ISSN: 1520-6106.
- [28] Prashant K Jain et al. "Noble metals on the nanoscale: optical and photothermal properties and some applications in imaging, sensing, biology, and medicine." In: *Accounts of chemical research* 41.12 (Dec. 2008), pp. 1578–86. ISSN: 1520-4898.
- [29] Huanjun Chen et al. "Gold nanorods and their plasmonic properties." en. In: *Chemical Society reviews* 42.7 (Apr. 2013), pp. 2679–724. ISSN: 1460-4744.
- [30] Gustav Mie. "Beitrage zur Optik truber Medien, speziell kolloidaler Metallosungen". In: *Annalen der Physik* 330.3 (1908), pp. 377–445. ISSN: 00033804.
- [31] R Weissleder. "A clearer vision for in vivo imaging." In: *Nature biotechnology* 19.4 (Apr. 2001), pp. 316–7. ISSN: 1087-0156.

- [32] Saumyakanti Khatua and Michel Orrit. "Probing, Sensing, and Fluorescence Enhancement with Single Gold Nanorods." In: *The journal of physical chemistry letters* 5.17 (Sept. 2014), pp. 3000–6. ISSN: 1948-7185.
- [33] Prashant K Jain et al. "Calculated Absorption and Scattering Properties of Gold Nanoparticles of Different Size, Shape, and Composition: Applications in Biological Imaging and Biomedicine". In: *The Journal of Physical Chemistry* (2006).
- [34] Meindert Alexander van Dijk and Faculteit der Wiskunde en Natuurwetenschappen. *Nonlinear optical studies of single gold nanoparticles*. en.
- [35] P Zijlstra and M Orrit. "Single metal nanoparticles: optical detection, spectroscopy and applications". en. In: *Reports on Progress in Physics* 74.10 (Oct. 2011), p. 106401. ISSN: 0034-4885.
- [36] R. Gans. "Über die Form ultramikroskopischer Goldteilchen". In: *Annalen der Physik* 342.5 (1912), pp. 881–900. ISSN: 00033804.
- [37] Craig F. Bohren and Donald R. Huffman. *Absorption and Scattering of Light by Small Particles*. Weinheim, Germany: Wiley-VCH Verlag GmbH, Apr. 1983. ISBN: 9783527618156.
- [38] Xiaohua Huang, Svetlana Neretina, and Mostafa A. El-Sayed. "Gold Nanorods: From Synthesis and Properties to Biological and Biomedical Applications". In: *Advanced Materials* 21.48 (Dec. 2009), pp. 4880–4910. ISSN: 09359648.
- [39] S. Link, M. B. Mohamed, and M. A. El-Sayed. "Simulation of the Optical Absorption Spectra of Gold Nanorods as a Function of Their Aspect Ratio and the Effect of the Medium Dielectric Constant". In: *The Journal of Physical Chemistry B* 103.16 (Apr. 1999), pp. 3073–3077. ISSN: 1520-6106.
- [40] Nengyue Gao et al. "Shape-Dependent Two-Photon Photoluminescence of Single Gold Nanoparticles". In: *The Journal of Physical Chemistry C* (June 2014), p. 140611092005007. ISSN: 1932-7447.
- [41] Kyeong-Seok Lee and Mostafa A El-Sayed. "Dependence of the enhanced optical scattering efficiency relative to that of absorption for gold metal nanorods on aspect ratio, size, end-cap shape, and medium refractive index." In: *The journal of physical chemistry. B* 109.43 (Nov. 2005), pp. 20331–8. ISSN: 1520-6106.

-
- [42] Moustafa R K Ali, Brian Snyder, and Mostafa a El-Sayed. "Synthesis and optical properties of small Au nanorods using a seedless growth technique." In: *Langmuir : the ACS journal of surfaces and colloids* 28.25 (June 2012), pp. 9807–15. ISSN: 1520-5827.
- [43] A. Mooradian. "Photoluminescence of Metals". In: *Physical Review Letters* 22.5 (Feb. 1969), pp. 185–187. ISSN: 0031-9007.
- [44] G. T. Boyd, Z. H. Yu, and Y. R. Shen. "Photoinduced luminescence from the noble metals and its enhancement on roughened surfaces". In: *Physical Review B* 33.12 (June 1986), pp. 7923–7936. ISSN: 0163-1829.
- [45] Mona B. Mohamed et al. "The 'lightning' gold nanorods: fluorescence enhancement of over a million compared to the gold metal". In: *Chemical Physics Letters* 317.6 (Feb. 2000), pp. 517–523. ISSN: 00092614.
- [46] Susie Eustis and Mostafa El-Sayed. "Aspect ratio dependence of the enhanced fluorescence intensity of gold nanorods: experimental and simulation study." In: *The journal of physical chemistry. B* 109.34 (Sept. 2005), pp. 16350–6. ISSN: 1520-6106.
- [47] Da-Shin Wang, Fu-Yin Hsu, and Chii-Wann Lin. "Surface plasmon effects on two photon luminescence of gold nanorods". In: *Optics Express* 17.14 (June 2009), p. 11350. ISSN: 1094-4087.
- [48] Mustafa Yorulmaz et al. "Luminescence quantum yield of single gold nanorods." In: *Nano letters* 12.8 (Aug. 2012), pp. 4385–91. ISSN: 1530-6992.
- [49] Haifeng Wang et al. "In vitro and in vivo two-photon luminescence imaging of single gold nanorods." In: *Proceedings of the National Academy of Sciences of the United States of America* 102.44 (Nov. 2005), pp. 15752–6. ISSN: 0027-8424.
- [50] Kohei Imura, Tetsuhiko Nagahara, and Hiromi Okamoto. "Near-field two-photon induced photoluminescence from single gold nanorods and imaging of plasmon modes." In: *The journal of physical chemistry. B* 109.27 (July 2005), pp. 13214–20. ISSN: 1520-6106.
- [51] P. Biagioni et al. "Dependence of the two-photon photoluminescence yield of gold nanostructures on the laser pulse duration". In: *Physical Review B* 80.4 (July 2009), p. 045411. ISSN: 1098-0121.

- [52] A. Bouhelier et al. “Surface Plasmon Characteristics of Tunable Photoluminescence in Single Gold Nanorods”. In: *Physical Review Letters* 95.26 (Dec. 2005), pp. 4–7. ISSN: 0031-9007.
- [53] Peter Zijlstra, James W M Chon, and Min Gu. “Five-dimensional optical recording mediated by surface plasmons in gold nanorods.” In: *Nature* 459.7245 (May 2009), pp. 410–3. ISSN: 1476-4687.

CHAPTER 2

ACCURACY OF THE DETECTION OF BINDING EVENTS USING 3D SINGLE-PARTICLE TRACKING

Nanoparticles can be used as markers to track the position of biomolecules inside living cells. The activity of a protein can sometimes be inferred from changes in the mobility of the attached particle. Mean squared displacement analysis is the most common method to obtain mobility information, such as the diffusion coefficient D , from trajectories of tracked particles. The precision of D sets a limitation to discriminate changes in mobility caused by biological events from the statistical variation inherent to diffusion. This issue is of particular importance in an experiment aiming to quantify dynamic processes.

Here, we present simulations and 3D tracking experiments with gold nanorods freely diffusing in glycerol solution to establish the best analysis parameters to extract the diffusion. We applied this knowledge to the detection of a temporary change in diffusion, as it can occur due to the transient binding of a particle to an immobile structure within the cell. The simulations show that the spatial accuracy of the particle tracking generally does not limit the detection of such binding event. However, changes in mobility can only be detected reliably when they last for a sufficient number of frames.

This chapter is based on: S.Carozza, J. Culin, J. van Noort *Accuracy of the detection of binding events using 3D single-particle tracking*, 2017, BMC Biophysics

2.1 Introduction

Cells present a dynamic environment for the biomolecules that orchestrate life: important processes such as intracellular or intramembrane trafficking [1–3] protein dynamics [4, 5] and gene delivery [6, 7] can be studied in detail by analyzing the mobility of the molecules involved. Single-molecule tracking (SMT) is a powerful tool to investigate such dynamic processes. SMT discloses information unobtainable using ensemble techniques, because following molecules individually can reveal variations in behavior that occur during the process, including rare events that are otherwise obscured in the ensemble. The high precision of SMT relies on the possibility to localize a single molecule with higher accuracy than the diffraction limit [8]. Ultimately, the accuracy of localization depends on the optical brightness of the molecule. Because most biomolecules can not be detected using optical microscopy, they need to be labeled with fluorescent markers like organic dyes or fluorescent proteins. Alternatively, metal or semiconductor nanoparticles have been used as labels to track single molecules. Single-particle tracking (SPT) [9] is advantageous over SMT because nanoparticles are generally brighter than fluorophores and can therefore be tracked with better precision. Moreover, as opposed to single fluorophores, nanoparticles do not bleach, which extends the time span over which a single molecule can be followed. However, nanoparticles are larger than single fluorophores, and will thus affect the mobility of the molecules of interest. A more detailed discussion on the advantages of metal nanoparticles over other labels is presented in Chapter 1, Section 1.1.1.

From SPT one can obtain long time traces of single molecules, that are then analyzed to quantify mobility. The mean squared displacement (MSD) of the particle reveals characteristic modes of mobility like free diffusion, confined diffusion and active transport, which are characterized by parameters such as diffusion coefficient (D), velocity and confinement size. The ability to track individual molecules, labeled with nanoparticles, with nanometer precision and over long times would make it possible to observe transient changes in the mobility of the molecule that could not be observed using other methods. For example, the binding of a transcription factor to its DNA target has been challenging to detect at the single-molecule level. Though fluorescence correlation spectroscopy (FCS) and SMT approaches have been used to study this process [10, 11], the short length of the traces, due to photobleaching and/or diffusion

out of the detection volume, generally directs data analysis to ensemble properties rather than those of single molecules. Therefore, SPT could provide a unique alternative for monitoring the dynamics of an attached molecule.

How reliable are the mobility parameters extracted from such SPT experiments? In the case of active transport, the localization accuracy is the most important factor influencing the precision of the particle velocity [12]. In the case of diffusion an evaluation of the accuracy of D is more complex: diffusion is a stochastic process, and this requires the measurement of many independent localizations to obtain D with high precision. The precision of D is of high relevance for biological experiments, as it sets a threshold to discriminate a biologically meaningful change in diffusion from the intrinsically stochastic variations.

Here we investigated how accurately the diffusion coefficient of a particle can be measured in a SPT experiment, and how well we can detect a transition in its diffusion behavior. The issue of accuracy of diffusion coefficients has been addressed before, with a theoretical approach and simulations [12, 13], but mainly in 2D. 2D SPT can provide higher temporal resolution than in 3D, but the images are limited in space to single planes and the tracking can be performed only as long as the particle stays in the plane: the use of 2D SPT is therefore limited to tracking in cell compartments that can be approximated to 2D such as the cell membrane [14, 15]. The simulations in this report extend the analysis of the accuracy of the detection of D to 3D tracking experiments.

We used a particular kind of nanoparticles, gold nanorods (GNRs), as labels for 3D SP using two-photon excitation. We used a two-photon multifocal scanning microscope to acquire multiple z sections forming a 3D stack of images. Some 3D SPT techniques have a higher temporal resolution compared to z sectioning, like for example the use of cylindrical lens to extract 3D positioning [1]. However, the use of astigmatism is not compatible with two-photon excitation, and thus lacks the benefits of higher signal-to-noise; total internal reflection fluorescence (TIRF) microscopy [16] gives high spatial and temporal resolution, but within a limited 3D area, not sufficient to cover the entire volume of a cell; orbital tracking [17] tracks only one particle at the time and cannot benefit from the high throughput of parallel tracking. A good alternative to two-photon multifocal microscopy is two-photon light sheet microscopy

[18] that provides good penetration depth in the sample and a comparable acquisition speed; for SPT these two techniques present similar challenges.

The outline of this chapter is as follows: first, we addressed the influence of positional accuracy of the 3D tracking scheme on the precision of the extracted MSD with simulations; then we analyzed the accuracy of the obtained diffusion coefficient with simulations and experiments; we optimized the parameters that are used to obtain D from the MSD; finally we simulated traces containing a change in diffusion behavior and established the experimental boundaries for resolving such changes.

2.2 Materials and methods

Experimental setup

The acquisition of 3D movies of single GNRs was performed on a home-built two-photon multifocal scanning microscope as previously reported in [19], with some small changes. A near IR pulsed laser (Coherent Chameleon Ultra) was used for excitation; the laser beam was split in an array of 625 beams by a diffractive optical element (DOE, custom made by Holoeye). A fast scanning mirror, driven with an Archimedean spiral function, was used to scan the array of beams over the sample: this way we obtained a wide and homogenous excitation on an area of about $60\ \mu\text{m} \times 60\ \mu\text{m}$, and collect images of tens of GNRs within this area. A piezo-stage (PIfoc, PI) was used to move the objective in the z -axis to collect 3D images. We acquired images with an EMCCD Camera (Photometrics QuantEM 512SC). The frame size was 400 pixels \times 400 pixels, corresponding to about $60\ \mu\text{m} \times 60\ \mu\text{m}$ and the separation between z slices was typically $0.5\ \mu\text{m}$. We acquired 10 z slices per stack, at a rate of 10 frames/s: the time resolution of our 3D localization was therefore 1 s/stack. A more detailed description of the setup can be found in Chapter 1, Section 1.2.3.

Sample preparation

Samples of GNRs of two different sizes were used: $47\pm 4\ \text{nm} \times 14\pm 2\ \text{nm}$ GNRs were synthesized through a seed-mediated method [20], while $53\pm 6\ \text{nm} \times 16\pm 3\ \text{nm}$ GNRs were purchased from Nanopartz (A12-25-

780-CTAB). Both GNRs samples were coated with a polyethylene glycol (PEG) layer before use. GNR sizes were obtained from transmission electron microscope (TEM, JEOL JEM 1010) images of both batches. The TEM images also provided a measure for the size dispersion within the two samples. The GNR sizes used for our theoretical calculations were increased by the thickness of a PEG layer. The size of the PEG layer (which cannot be seen in TEM) was measured independently using fluorescence correlation spectroscopy (FCS, [21]), yielding an effective PEG layer thickness of 8.1 nm (see Figure S1). GNRs were first suspended in small volumes of demineralized water, then glycerol was added to reach the desired concentration of 95% and 90%. For SPT in glycerol both GNR samples were excited at a wavelength of 770 nm.

Simulations

Simulations of movies of diffusing GNRs were performed in LabVIEW using the following procedure: a set of 3D trajectories was created, according to a given diffusion coefficient D (or multiple values of D , in case of changes in behavior); a stack of empty frames was then filled with a 3D Gaussian peak for each time coordinate, and amplitude and standard deviation of the peak were set using typical values obtained experimentally for single GNRs (amplitude=1000 a.u., s_{xy} =300 nm, s_z =650 nm); Poissonian noise was added to each pixel in the peak in order to simulate shot-noise; an offset (1000 a.u.) and a background noise (1 a.u.) were added to the entire 3D stack of images, reflecting the camera gain settings and detection noise. As opposed to experimental movies, in simulated movies we introduced only one GNR to prevent incorrect trajectory assignments when GNRs would cross. We simulated videos with a frame rate of 10 frames/s, as typically collected by our setup. The frame size was 300 pixels x 300 pixels (corresponding to about 52 μm x 52 μm , and the separation between z slices was 1 μm).

Data analysis

Image analysis was also performed in LabVIEW. The same analysis was applied to simulated and real movies. In each 3D stack of images, peaks were detected and fitted with a 3D Gaussian function: from the fit we obtained position, intensity, offset and width of each peak. When more than one trace was present in the movie, peaks were connected to traces

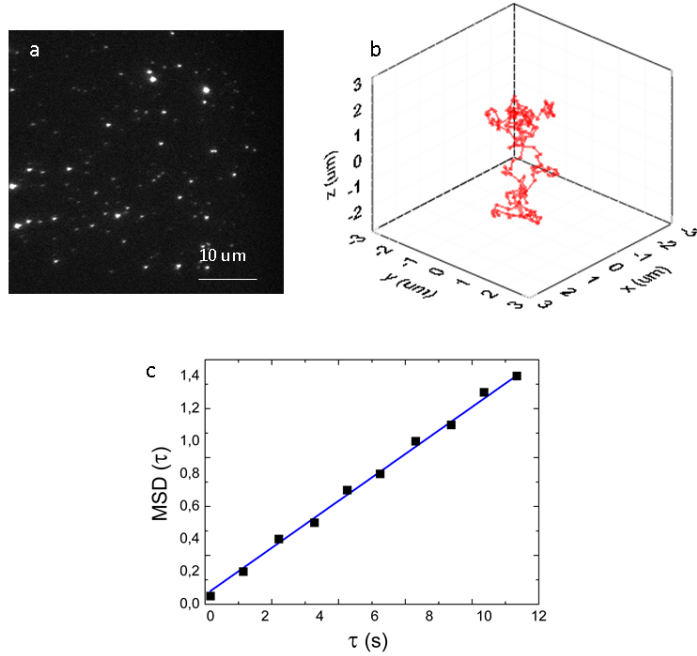


Figure 2.1

Steps to extract the diffusion constant of single GNRs in glycerol. From a movie of 3D stacks of frames (as the frame in a), trajectories of single GNRs were extracted (b), and on each of them a MSD analysis was performed. c) The MSD plot was fitted to a line with a slope that corresponds to the diffusion coefficient, and offset proportional to the 3D positional accuracy (Eq. 2.6).

using a minimal excursion criterion. Once traces were obtained, an MSD analysis was performed. An illustration of the method is shown in Fig. 2.1, and details of the MSD analysis process are described in the next section.

2.3 Theory

2.3.1 Localization accuracy

Figure 2.1a shows a typical 2D image of a number of GNRs, of which peaks are convoluted with the Point Spread Functions (PSFs) of the microscope. The localization uncertainty σ of a single particle in a 2D

fluorescent image was described by Thompson as [8]:

$$\sigma = \sqrt{\frac{s^2}{N_p} + \frac{a^2}{12N_p} + \frac{8\pi s^2 b^2}{a^2 N_p^2}} \quad (2.1)$$

where s is the width of the PSF, N_p is the number of photons, a is the pixel size and b the number of photons in the background noise. The uncertainty in position decreases with increasing number of photons, as is characteristic for shot-noise. Mortensen [22] later modified this equation into:

$$\sigma = \sqrt{\frac{s_a^2}{N_p} \left(\frac{16}{9} + \frac{8\pi s_a^2 b^2}{N_p a^2} \right)} \quad (2.2)$$

where $s_a^2 = s^2 + a^2/12$. To the best of our knowledge, a description of the positional uncertainty in the case of 3D images has never been reported. Previously, we observed an experimental increase in x and y accuracy in 3D data that originated from the additional photons recorded in all frames above and below focus that contribute to a 3D peak ([19]). These measurements were made using fixed, immobile GNRs. In the results section we will quantify this effect. However, changes in positions between slices in a stack will affect the positional accuracy.

2.3.2 Accuracy of mean square displacement analysis

For now we will ignore the movement between slices in the stack and analyze single traces (Fig. 2.1b) by calculation of the mean squared displacement. The MSD of a trajectory is the average of all the squared displacements r^2 occurring within time steps of different duration τ :

$$MSD(\tau) = \frac{1}{n_\tau} \sum_{i=1}^{n_\tau} (r_{i+\tau} - r_i)^2 \quad (2.3)$$

where n_τ is the number of steps, equal to $(T-\tau)/\tau$: T is the total length of the trace and τ is the time lag between displacements. The diffusion of a particle is quantified by the coefficient D , described by the Stokes-Einstein equation:

$$D = \frac{kT}{6\pi\eta R} \quad (2.4)$$

where k is the Boltzmann constant, T the temperature, R the radius of the particle and η the viscosity of the medium. In the case of a rod, an ‘equivalent radius’, the radius of a sphere with equivalent volume, is used. It is defined as:

$$R_{\text{eq}} = (ab^2)^{1/3} \quad (2.5)$$

where a and b are the longer and shorter axis of the rod. For free diffusion in an isotropic medium the MSD has a linear dependence on τ [4], and in 3D it results in:

$$MSD(\tau) = 6D\tau + 6\sigma^2 \quad (2.6)$$

Fitting Eq. 2.6, one can obtain the diffusion coefficient D , as well as the 3D localization accuracy σ . Fig. 2.1c shows an example of an MSD plot and its fit with Eq. 2.6. A parameter that has a large influence on the accuracy of the fit is the number of MSD points that are included in the fit. In the example in Fig. 2.1c, the GNR trace is about 100 points long, and we fitted the first 10 MSD points to obtain D . When dealing with shorter traces though, the points in the MSD plot at larger time delays become increasingly random, due to the stochastic nature of diffusion and the fewer measurements that contribute to the mean. Including these points in the fit may yield an erroneous D . Due to this inherent statistical variance in the MSD, the error on the obtained D can be significant and will depend on the number of points that are included in the fit. The relative error in D is defined as:

$$\rho = \left| \frac{D - D_{\text{measured}}}{D} \right| \quad (2.7)$$

Qian et al. [12] showed that ρ depends on the total length of the trajectory N and on the number of fitting points n , and it approximates to:

$$\rho = \sqrt{\frac{2n}{3K}} \quad (2.8)$$

where $K=N-n$. Weighting MSD points according to the sample size could yield a better accuracy, but Thompson [8] showed that the effect of this correction is negligible. Michalet [13] extended Quian’s analysis to conditions with a finite localization uncertainty to determine the best

number of fitting points for the analysis. He calculates the relative error to be:

$$\rho = \left\{ \frac{n}{6K^2} (4Kn^2 + 2K + n - n^3) + \frac{1}{K} \left[2nx + x^2 \left(1 + \frac{1 - \frac{n}{K}}{2} \right) \right] \right\}^{1/2} \quad (2.9)$$

where x is the reduced positional uncertainty and is defined as:

$$x = \frac{\sigma_2}{D\Delta t} \quad (2.10)$$

and Δt is the sample time. Eq. 2.9 converges to Eq. 2.8 for $x = 0$, large N ($N \approx 1000$) and $K \gg n$ [13]. In our work we use Michalet's formula for ρ as we have a non-zero positional uncertainty and traces shorter than 1000 points. Michalet showed that choosing a non-optimal number of fitting points results in a diffusion coefficient noticeably larger than the actual one. He calculated the best number of fitting points to be:

$$n = 2 + 2.3x^{0.52} \quad (2.11)$$

Therefore, the optimal number of fitting points to use depends on positional uncertainty, diffusion coefficient and sampling time. In a real experiments the expected D is typically not known, so n is not easy to evaluate. An estimate of the order of magnitude of the D to expect is a first good step. A higher sampling rate or a lower precision increases the value of the optimal n to use. We tested Michalet's results with 3D simulations using different positional uncertainties and diffusion coefficients. Then we validated these results with experiments using GNRs with known D , compared D to the value measured with SPT and calculated the relative error ρ .

2.3.3 Detection of changes in the diffusion coefficient

Having a well-defined, constant D , is however highly simplistic when doing SPT in cells: over time a molecule will undergo transitions in the diffusion behavior. We simulated and analyzed traces containing a transition in diffusion, in particular a period with a lower diffusion coefficient (Fig. 2.2a), mimicking for example the binding of a particle to a fixed structure in the cell. To analyze these traces, we needed to detect the transition points. From a rolling window MSD analysis, a

plot of the variations of D within the trace was obtained (Fig. 2.2b). This $D(t)$ plot was then analyzed with a Student's T-test, evaluating the probability that two populations belong to the same distribution. In our case we used a modified version of Student's T-test, the Welch's test [23], optimized for populations with different variances. It calculates the T-statistic as:

$$T = \frac{X_1 - X_2}{\sqrt{\frac{s_1^2}{N_1} + \frac{s_2^2}{N_2}}} \quad (2.12)$$

where X_1 , X_2 are the means of the two samples, s_1 , s_2 their variances and N_1 , N_2 the samples sizes. The probability that the two samples are described by the same distribution is calculated using the T-distribution probability density function [23]:

$$p(T, \nu) = \frac{\Gamma(\frac{\nu+1}{2})}{\sqrt{\pi\nu}\Gamma(\frac{\nu}{2})} \left(1 + \frac{T^2}{\nu}\right)^{-\frac{\nu+1}{2}} \quad (2.13)$$

in which Γ is the gamma function.

The degrees of freedom ν are approximated by the Welch-Satterthwaite equation as:

$$\nu \approx \frac{\frac{s_1^2}{N_1} + \frac{s_2^2}{N_2}}{\frac{s_1^4}{N_1(N_1-1)} + \frac{s_2^4}{N_2(N_2-1)}} \quad (2.14)$$

A p-value is calculated for each point in the D plot, considering two windows of the same size around the point. The minima in the probability plot (Fig. 2.2c) correspond to the points in the trace where a diffusion transition is most likely to happen. Rolling windows with different sizes (N_1 and N_2 in Eq. 2.12 and 2.14) did not show noticeable differences. We chose a rolling window size of 15 steps, and a Welch test sample size of 15 or 10, when the gap was shorter than 15 steps. Transition points were assigned using a threshold for P and the initial trace was divided in subtraces. We tested different values for the threshold, and we obtained the best compromise between false negative and false positive results with a value of 10^{-10} .

As shown in Fig. 2.2c, not all the detected transition points corresponded to real transitions: some were misassigned due to stochastic fluctuations in D . We performed a second Welch test on these subtraces

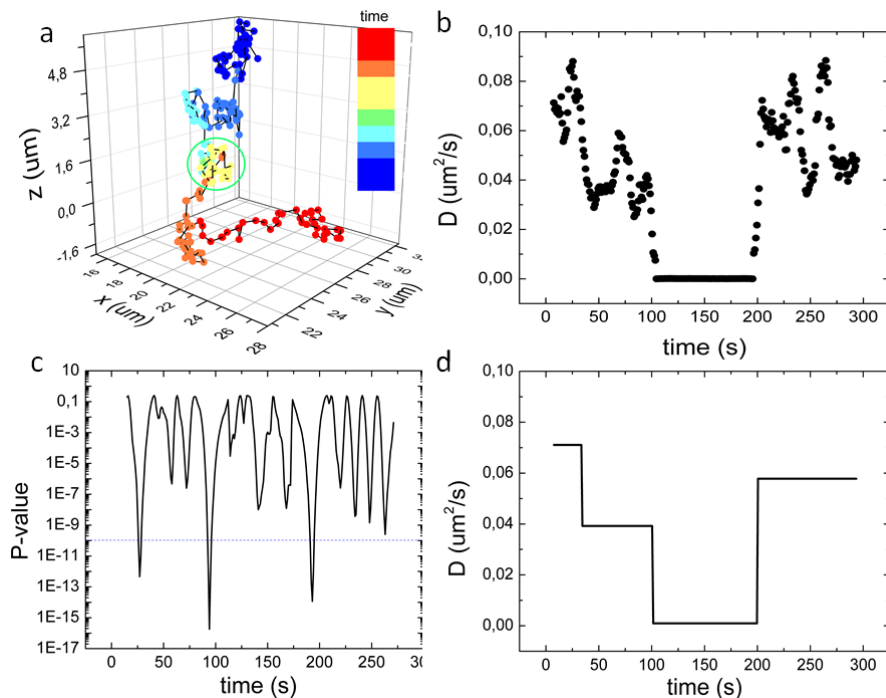


Figure 2.2

Detection of diffusion transitions. a) A simulated trajectory, which contains a brief period of reduced mobility. In this gap D was $0,0001 \mu\text{m}^2/\text{s}$, while the D in the rest of the trace was $0,05 \mu\text{m}^2/\text{s}$. The gap is highlighted with a green circle. b) The diffusion coefficient along the trajectory $D(t)$ was calculated using a 15 points rolling-window method. c) A Welch test yielded minima in the P -value plot, that indicate possible transition points used to divide the trajectory in subtraces. d) D values obtained from the MSD of each subtrace.

using window sizes corresponding to the entire subtraces length. The transitions confirmed by the second test were accepted as real transition points. Despite this second statistical test, it was not always possible to assign each transition point correctly. For example in Fig. 2.2c at $t = 25$ s a change in D was wrongfully detected. A new MSD analysis was finally done on the final subtraces to obtain the mean D , which is plotted in Fig. 2.2d.

2.4 Results and discussion

2.4.1 Spatial and temporal resolution

We first performed simulations to obtain the positional accuracy for 3D images with fixed peak positions. We tested cases with different numbers of photons N at fixed background noise b . We simulated static GNRs: the uncertainty was calculated from the difference between the input coordinates and the coordinates obtained from the Gaussian fit and plotted in Fig. 2.3a. For 2D data only the central frame in each 3D stack was used. In this case, the positional uncertainty was consistently higher than expected based on Thompson's formula (Eq. 2.1). A similar discrepancy between theory and simulations was reported previously [8]. Mortensen's formula (Eq. 2.2) results in a 30% increase in positional uncertainty, that follows closely our 2D data. However, in the case of 3D data, the underestimate positional uncertainty obtained using Thompson's formula compensates for the larger number of photons collected for a peak in a 3D stack. Therefore, in this work we used Eq. 2.1 to calculate the positional uncertainty of 3D peaks.

In the analysis of dynamic data, the temporal resolution plays an important role: the finite time between acquisitions can obscure fast dynamic processes. Moreover, in real experiments, the movement of the particle occurs also between slices within a 3D stack: we simulated this movement within a stack for a range of diffusion coefficients: as shown in Fig. 2.3b, the effect of the movement within stacks can be dramatic for large diffusion coefficients. The positional uncertainty in the x-y plane for the lowest diffusion constant ($D = 0.01 \mu\text{m}^2/\text{s}$) is about $9.5 \pm 0.6 \text{ nm}$, for the highest ($D = 0.5 \mu\text{m}^2/\text{s}$) σ is $143.0 \pm 8.4 \text{ nm}$. In the z direction, the uncertainty follows the same trend but is even more pronounced. In the experiments on GNRs performed with our setup, the number of photons collected was very high, due to the high brightness of the two-photon signal of GNRs and low background. From Eq. 2.1 we calculate a positional accuracy of 4 nm (see Figure S2) for an average N_p of 4000 photons. However, due to the GNR movement between slices, the positional uncertainty is increased: considering the diffusion coefficient range expected for our experiments (between 0.02 and $0.07 \mu\text{m}^2/\text{s}$), we expect the effective positional uncertainty in x,y to be around 20 nm, and in z around 40 nm. The uncertainty values obtained from the MSD fit is

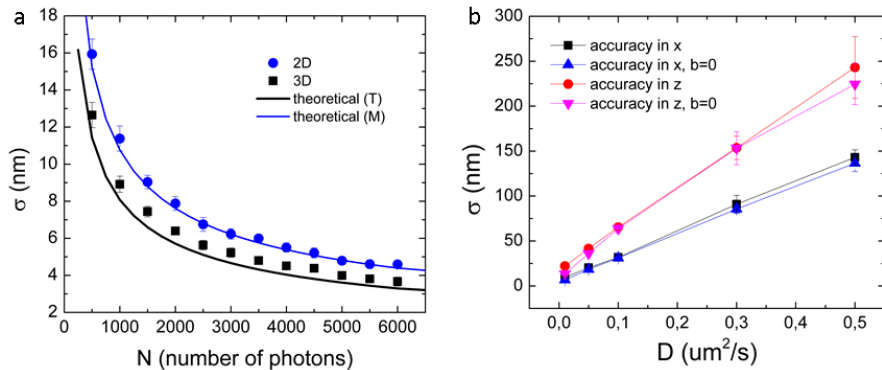


Figure 2.3

The positional uncertainty in 2D and 3D simulations depends on the brightness and the temporal resolution. a) The localization uncertainty improves with increasing number of photons emitted from the GNR. The black line represents the theoretical value obtained from Thompson's Eq. 2.1, the blue line represents the theoretical value obtained using Mortensen's Eq. 2.2. The images obtained from simulations were analyzed in 2D (fitting only one slice per 3D stack, blue dots) and in 3D (fitting the whole 3D stack, black squares). Each point in the graph is an average of 10 sets of 200 simulated images. The background noise was kept constant at $b = 0.5$. b) The effect of the movement of the particle between frames for an acquisition time of 10 fr/s.

around 40 nm: this value includes the x-y and the z components, and is comparable to the σ value in z obtained from simulations.

2.4.2 Factors that determine the uncertainty in the detection of the diffusion coefficient

The stochastic nature of diffusion is another source of uncertainty in the determination of the diffusion coefficient D . Following Eq. 2.8, the length of the trace and the number of MSD fitting points have a large influence on the error in D . In Fig. 2.4a, results from simulations show that the best number of fitting points for data with low positional uncertainty is 2, for different values of D , in accordance with Michalet's results. When the positional uncertainty increases (Fig. 2.4b), it has a large influence on the first MSD points, so more MSD points are required for an accurate determination of D . The length of the traces also affects the precision of the obtained D (Fig. 2.5): longer traces allows for better statistics in

the calculation of the MSD. The positional uncertainty can be calculated from the measurement independently using the number of photons (Eq. 2.1). Fig. 2.5 shows that fixing the positional uncertainty σ in the MSD fit slightly improves the final result.

In summary, these precautions can reduce the error on the obtained D : using long traces, fixing the positional uncertainty of the MSD fit, and limiting the fit to the first two MSD points. Nevertheless, even with high positional accuracy, one will obtain relatively large errors in D when measuring for finite times due to the stochastic nature of diffusion.

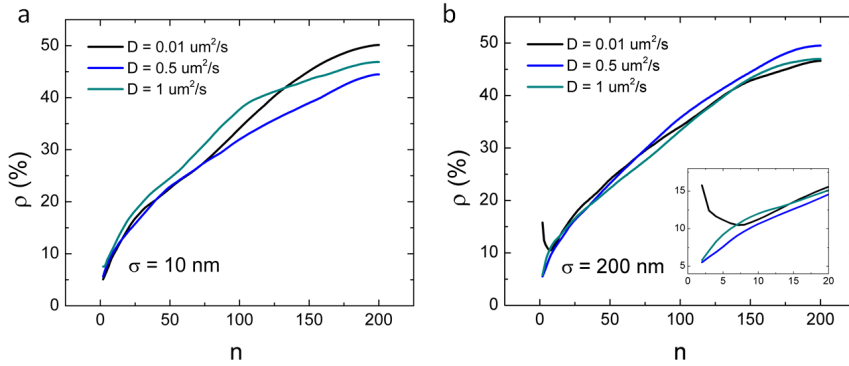


Figure 2.4

Stochastic variations in diffusion limit the accuracy of D measurements. a) In case of low positional uncertainty ($\sigma = 10 \text{ nm}$), the best number of fitting points is 2, for different values of D . b) In case of higher positional uncertainty ($\sigma = 200 \text{ nm}$), errors in position detection dominate the error in D for small displacements, and the best number of MSD points increases (see inset). Each point in the plot is the average ρ obtained from 100 simulations of 200 points traces.

2.4.3 Experimental validation of the diffusion coefficient accuracy using gold nanorods in glycerol

We next tested our results on experimental traces of GNRs diffusing in glycerol with a well-known diffusion coefficient, rather than in a cellular environment, which is not homogeneous and therefore the diffusion coefficient would not be well-defined. We compared the statistical variations in D to the variations predicted based on the size dispersion of our GNR samples. Experiments were performed with two GNRs sizes and

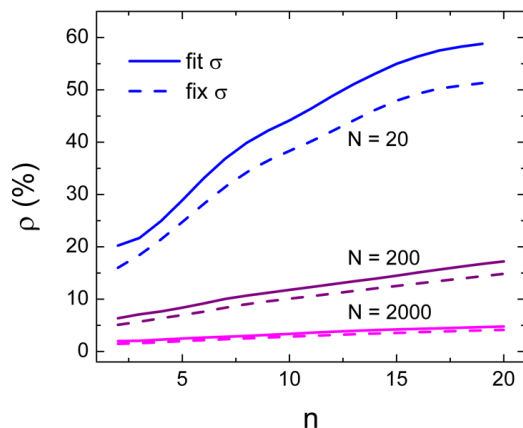


Figure 2.5

Optimizing the accuracy of D measurements for single trajectories. Using longer traces improves the estimate of D , lowering ρ . Fixing the positional uncertainty σ (dashed line) in the MSD fit reduces in the relative error compared to fitting it (continuous line). Each point is the average ρ obtained from 100 simulated traces with length as indicated in the legend and $D = 1 \mu\text{m}^2/\text{s}$.

two glycerol concentrations. The expected values of D , calculated using Eq. 2.4, are listed in Table S1. The values of D are at least two orders of magnitude smaller than the typical diffusion coefficients of proteins, due to the large size of the GNRs. Smaller GNRs may be used, but this would imply a weaker luminescence and a faster diffusion, which make it more difficult to accurately quantify the mobility. What follows are the results obtained from the first sample (52 nm x 16 nm GNRs in 95% glycerol), while the results from the other samples are summarized in Table S1. In Fig.2.6a, the relative errors ρ obtained experimentally are compared to the theoretical errors (Eq. 2.9). Fixing σ lowers the error in the estimate of D , especially when a smaller number of MSD points is used. The collected traces had a large variation in length: as the GNRs were free to move, the trace length was limited to the time the GNRs stayed in the volume of view. Consistent with Eq. 2.8 and 2.9 and the simulations, longer traces feature a more accurate D . In Fig. 2.6b only the traces longer than 80 points were used for analysis: this decreased the relative error from 40% to less than 20%. Curiously, while the theoretical value of the relative error increases with the number of MSD

fitting points, in the experimental values it had little or no influence. Using only the long traces, the precision slightly decreased with a number of MSD points larger than 5. In all cases the errors on D obtained experimentally were smaller than the ones calculated theoretically: this is not surprising, as the theoretical errors correspond to the standard deviation of the MSD curve, hence to the maximum value of the error [12, 13]).

In Fig. 2.6c we compare the experimental values (obtained fixing the positional uncertainty) for all the traces, traces longer than 40 points (about 1 minute) and 80 points (about 2 minutes). The first thing to notice is the dramatic decrease in the D error when using longer traces. For the longest traces, the smallest number of MSD fitting points yields the smallest error. Therefore, the minimum error in the calculation of D is obtained using only traces longer than 2 minutes, fixing the positional uncertainty and using only 2 fitting points: in these conditions we got a relative error as low as 10%.

In Fig. 2.7a the measured values of D are compared with the expected ones, calculated with Eq. 2.4. The variation in D based on the size dispersion of the GNRs, measured in TEM images, is depicted in the histograms using a blue shade around the expected value. As seen before, longer trace lengths improve the accuracy of D : when we limited the analysis to traces longer than 40 points (about 1 minute, Fig. 2.7b) and 80 points (about 2 minutes, Fig. 2.7c) the measured D increases from $0.020 \mu\text{m}^2/\text{s}$ to $0.022 \mu\text{m}^2/\text{s}$ and $0.026 \mu\text{m}^2/\text{s}$, where the expected D was $0.028 \mu\text{m}^2/\text{s}$. The relative errors in D obtained for this GNR sample and other samples are reported in Table S1. In the experiments with shorter GNRs, the relative errors were higher, due to their faster diffusion which results in shorter traces. The variation in the measured D was always larger than the variation predicted based on the size dispersion (reported in the same table), because of the stochastic variations in D that increase its variability.

2.4.4 Detection of changes in diffusion in single particle trajectories

One of the unique possibilities of SPT is to follow a single molecule over a long time, and to directly detect changes in its behavior. The previous discussion on the difficulties to obtain a correct D implies, however, major challenges. In this paragraph we tested how accurately a

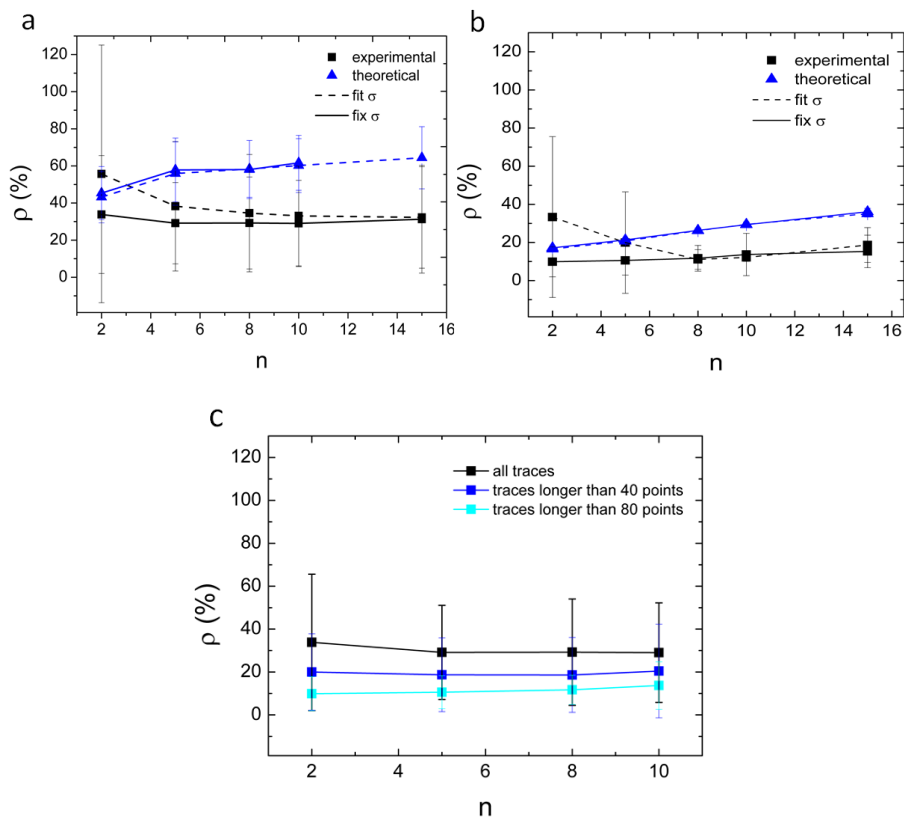


Figure 2.6

Optimal number of MSD points. The squares represent experimental values of ρ , calculated using Eq. 2.7. The data were obtained from traces of 53 nm x 16 nm GNRs in 95% glycerol. The triangles represent the theoretical values of ρ , obtained with Eq. 2.9. In a), traces of all lengths were considered (between 10 and 100 points), while in b) only traces longer than 80 points (about 2 minutes) were considered. In c) we compare the values of $\rho(D)$ obtained from traces of all lengths (from 10 to about 100 points, black squares) with the ones obtained from only traces longer than 40 points (blue squares) and 80 points (cyan); in all three cases the analysis was performed fixing the positional uncertainty.

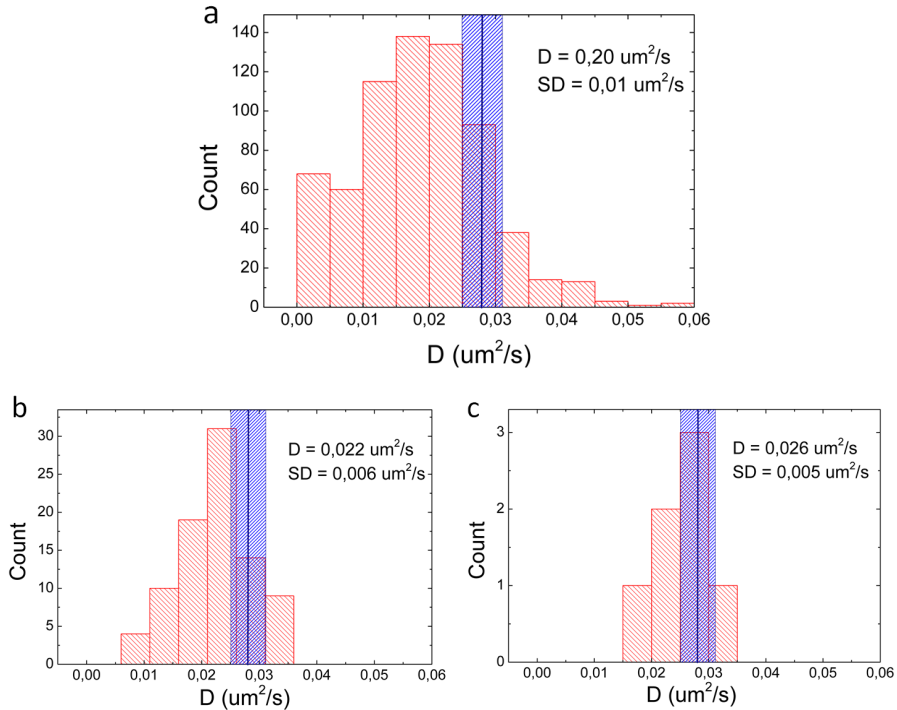


Figure 2.7

The diffusion coefficient measured using single particle trajectories is underestimated when using short traces. The distribution of the measured D is obtained using a) all traces or only traces longer than b) 40 points or c) 80 points for 53 nm x 16 nm GNRs in 95% glycerol. The center of the blue bar represents the expected value (calculated from Eq. 2.4); its width follows from the size dispersion measured from TEM images.

temporary reduction in diffusion constant of a particle (a ‘gap’) can be detected. Following the approach above, MSD analysis was performed with 2 points and fixed positional accuracy calculated from the intensity of the peak. The diffusion coefficient used for the initial and final phases was $0.05 \mu\text{m}^2/\text{s}$, the largest value we typically measure for GNRs inside cells, both in nucleus and cytoplasm (see Chapter 3, Section 3.3.2). We varied the D in the gap within a range of typical values we obtained in cells, from $0.0001 \mu\text{m}^2/\text{s}$ to $0.035 \mu\text{m}^2/\text{s}$. The residual mobility of a protein bound to DNA has been reported to be in this range [24, 25]. The initial and final phases were 100 s, while we tested different lengths

of the gap phase. We evaluated the effectiveness of the detection in the obtained diffusion coefficient and gap duration (D_{gap} and t_{gap}) in every set of 100 simulations. We considered D_{gap} correct when it was within $\pm 20\%$ of the set D , and we considered t_{gap} correct when it was within $\pm 10\%$ of the set length. An example of a trace simulated using a D_{gap} of $0.0001 \mu\text{m}^2/\text{s}$ is shown in Fig. 2.2a. In this figure, the gap is not clearly seen in the trajectory (as the time points are very close to each other), but it is easily distinguishable in the D plot. In real experiments the difference in mobility can be smaller.

First, we simulated traces with different D_{gap} , keeping the gap length constant to 100 s. In Fig. 2.8 the D_{gap} was set to 0.0001, to 0.01 and to $0.035 \mu\text{m}^2/\text{s}$. The scatter plots show the resulting D_{gap} and t_{gap} for 100 different simulations. In the first case ($D_{\text{gap}} = 0.0001 \mu\text{m}^2/\text{s}$, Fig. 2.8a,b) the transition is obvious. The Welch analysis yields reasonable results: in about 65% of the cases a gap with the right length is detected. The average t_{gap} is always overestimated, and therefore also the average D_{gap} . The positional uncertainty also contributes to the overestimate of D_{gap} , especially for low D_{gap} (see Figure S3a, b for $D_{\text{gap}} = 0$ and $0,001 \mu\text{m}^2/\text{s}$). For this reason, only 10% of the cases yield D_{gap} within 20% of the input value.

In the second case, where $D_{\text{gap}} = 0.01 \mu\text{m}^2/\text{s}$ (Fig. 2.8c,d), the transition is also clearly detectable. Both the correct t_{gap} and D_{gap} are detected in about 60% of the cases. In Fig. 2.8d, it is clear that most incorrect values originate from a missed transition, which results in a double duration of the gap phase, and an increased D_{gap} .

In the last case (Fig. 2.8e,f), $D_{\text{gap}} = 0.035 \mu\text{m}^2/\text{s}$, only 30% lower than the D outside the gap. Given an uncertainty of at least 10% in the detection of the single diffusion coefficient (see previous paragraph), we expect this difference to be hard to detect. Indeed, looking at $D(t)$ (Fig. 2.8e) we can still distinguish a change in D in the common trend, but the fluctuations in each single curve obscure transitions in D . In less than 10% of the traces a gap with the correct length is detected, but the correct D_{gap} is detected in 60% of the cases. This is due to the small difference between D inside and outside the gap: in the cases where the transition is detected at a different point in time, the obtained D will still be good enough, being an average between D and D_{gap} . In about 40% of the simulations no transition is detected (Fig. 2.8f). In Fig. S3

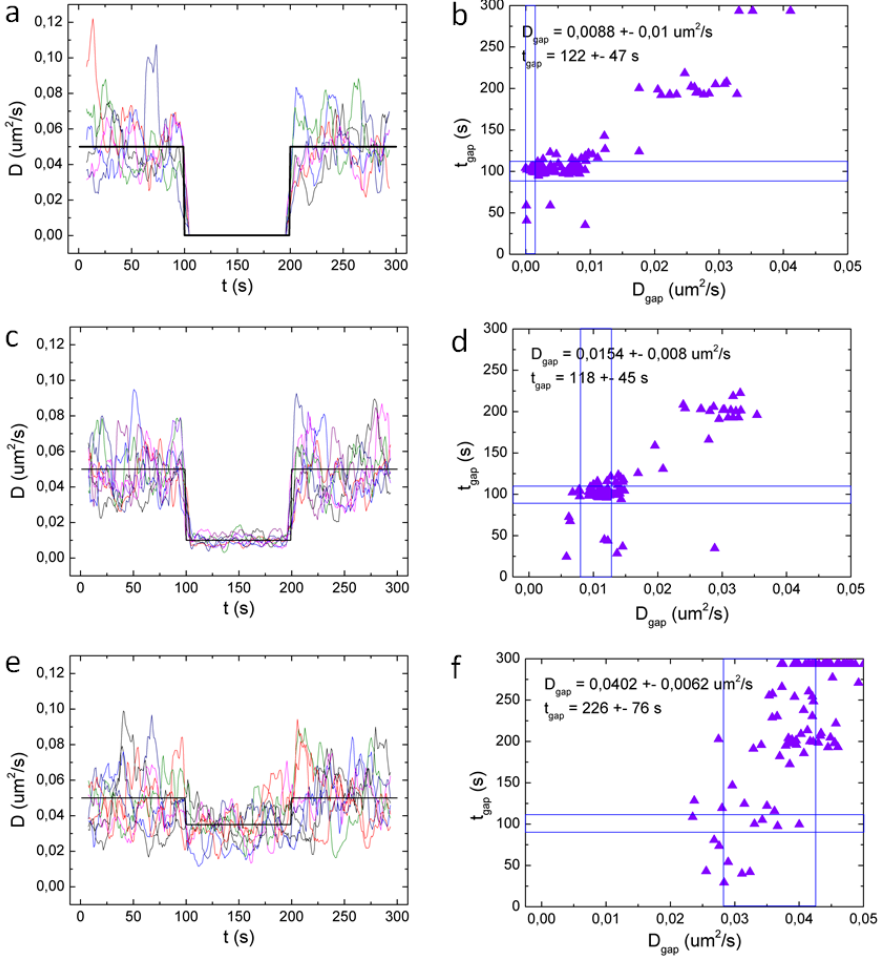


Figure 2.8

Limits to the detection of changes in diffusion. a,c,e) $D(t)$ plots obtained from the rolling-window analysis. b,d,f) Scatter plots of D_{gap} vs the length of the gap. The simulated $D(t)$ is plotted in black line. The D outside the gap was set to $0,05 \mu\text{m}^2/\text{s}$. $D_{\text{gap}} = 0,0001 \mu\text{m}^2/\text{s}$ for a,b, $D_{\text{gap}} = 0,01 \mu\text{m}^2/\text{s}$ for c,d and $D_{\text{gap}} = 0,035 \mu\text{m}^2/\text{s}$ for e,f. For every case, 100 traces were simulated and analyzed: a,c,e) $D(t)$ plot for 8 example traces. b,d,f) $D(t)$ from all 100 traces. The ranges of correct D_{gap} and t_{gap} are highlighted with blue lines in the scatter plot. The traces were analyzed using a rolling window and a Welch sample of 15 points.

more cases with different values of D_{gap} are reported.

Thus, changes in D smaller than 30% can easily be distinguished from averaged data, but in single trajectories a reduction of about 80% is required to detect 60% of such changes.

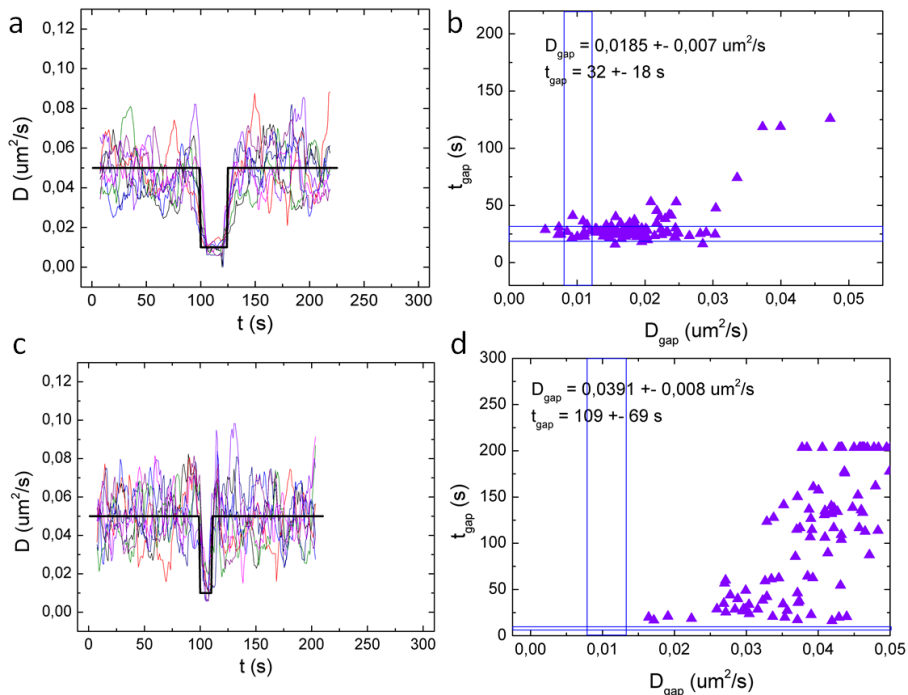


Figure 2.9

Limits to the detection of short-lived changes in diffusion. a,c) $D(t)$ plots obtained from rolling-window analysis. c,d) Scatter plots showing the results of the MSD analysis. The simulated $D(t)$ is plotted in black line. The D_{gap} was $0.01 \mu\text{m}^2/\text{s}$ and the D outside the gap was $0.05 \mu\text{m}^2/\text{s}$. $t_{\text{gap}} = 25 \text{ s}$ in a,b and $t_{\text{gap}} = 10 \text{ s}$ in c,d. The results can be compared to Fig. 2.8c and d, where the same D s were set with a gap length of 100 s . For every case 100 traces were simulated and analyzed. a,c) $D(t)$ for 10 example traces. b,d) $D(t)$ from all the traces. The ranges of correct D_{gap} and t_{gap} are highlighted with blue lines in the scatter plot. The traces were analyzed using a rolling window size of 15 points, and a Welch sample of b) 15 points and d) 10 points.

We expected transient changes to become more obscured as their duration shortens. We performed a similar analysis as function of the length of the gap t_{gap} , keeping D_{gap} constant at $0.01 \mu\text{m}^2/\text{s}$. In Fig. 2.9 the results obtained using a gap length of 25 s and 10 s are plotted. In

the case of $t_{gap} = 100$ s, (Fig. 2.8c,d), both the correct t_{gap} and D_{gap} are detected in about 60% of the cases. Reducing t_{gap} to 25 s (Fig. 2.9a,b), in only 35% of the simulations the correct t_{gap} is detected, and the correct D_{gap} in 20% of the cases. A gap of only 10 s (Fig. 2.9c,d) is very hard to detect: in none of the cases the correct t_{gap} or D_{gap} was detected. More results are reported in Fig. S4.

It is difficult to give an absolute limit of gap detectability in terms of D_{gap} or t_{gap} . A summary of the dependence of the detectability of the gap is plotted in Fig. 2.10. If the gap is long (100 s) and the ratio between D and D_{gap} is more than 50, at least 60% of the gaps are correctly assigned. If the length of the gap is reduced to 25 s we can still detect 50% of the gaps, but for gaps shorter than 20 s the detection rate drops to 0. We still detected a transition in 60% of the cases if $D/D_{gap} = 5$. But for $D/D_{gap} = 2$, the gap was detected in only 20% of the cases, even for long traces (100 s). In conclusion, a transient decrease in D can be detected easily when the D in the gap is very low, and the length of the gap is not too short. A similar conclusion is obtained for the detectability of the correct D_{gap} , with a difference: a small D_{gap} won't be fit correctly due to the noise introduced by the positional uncertainty (Fig. S5).

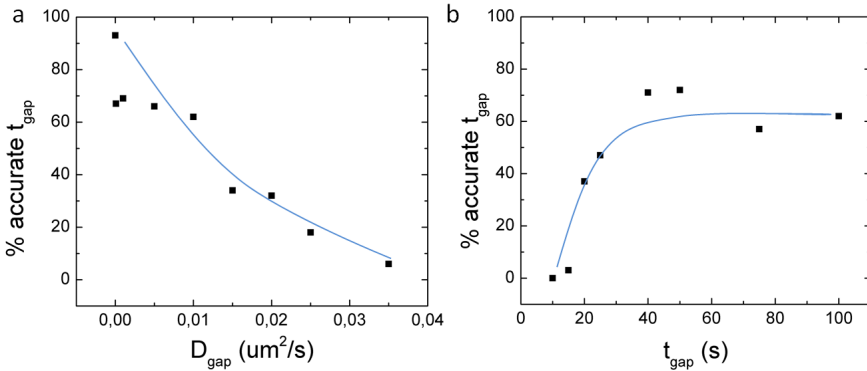


Figure 2.10

Percentage of accurate D_{gap} detections for different values of D_{gap} and t_{gap} . The percentage of the gaps detected with a length within 10% of the input is shown, for different values of a) D_{gap} and b) t_{gap} . Every point was obtained from 100 simulations of a trajectory containing a gap. The D outside the gap is $0,05 \mu\text{m}^2/\text{s}$, $t_{gap} = 100$ s and $D_{gap} = 0,01 \mu\text{m}^2/\text{s}$, if not stated otherwise. Lines are a guide to the eye.

To improve the precision of the results, a more complex measurement and analysis scheme could be used, that makes use of more parameters to detect subsections; for example, one could simultaneously measure the polarization of the signal. When applicable, other mobility parameters such as direction of the motion, velocity or confinement could be fit to the MSD curves. When such parameters are different during the binding of GNRs to cellular structure, Welch analysis can be performed [26, 27]. The final p-value, obtained by multiplying the p-values of different parameters, will give a more correct assignment of the transition points and consequently more precise estimates of t_{gap} and D_{gap} .

In practice, measuring D and D_{gap} of a protein will depend on the size of the protein and on the local viscosity of the environment. The smaller the molecules, the larger the difference in the diffusion coefficient when it binds to its substrate and the easier to detect the event accurately. The size of the GNR will set an upper limit to the diffusion coefficient that will be measured. The affinity of the protein is directly reflected in the ratio of the time between binding events and the lifetime of the bound complex (t_{gap}). The first may be affected by the presence of a GNR. A wide range of binding times have been reported for example for DNA binding proteins *in vivo*, ranging from sub-seconds [24] to several minutes [28]. The ability to track a single protein bound to a GNR will give a more detailed insight in the reaction kinetics and how the complex cellular environment affects this reaction. Here we have shown that using GNRs as labels can, in many conditions, resolve single binding events with nanometer and second accuracy.

2.5 Conclusion

Quantification of diffusion is challenging, especially under experimental conditions with limited accuracy, time resolution and finite length of the measurement. By performing simulations and experiments in controlled conditions, we established few guidelines to minimize the error on the MSD and consequently on D :

1. Use long trajectories: the larger the number of time points in the trace the better the MSD is. In our case, doubling the trace length

from 1 minute to 2 minutes yielded a two-fold improvement of the precision in the detected D .

2. In case of small positional uncertainties, theory and results from simulations suggest to use only the first two points for fitting the MSD.
3. Fixing the positional uncertainty during the MSD fit improves the evaluation of D .

These findings reinforce previous theoretical reports [8, 12]. In our case we tracked GNRs in 3D with an uncertainty of 4 nm based on shot-noise limitations, which increased to about 40 nm due to the movement of particles between each acquisition. With these conditions, the best approximation of D was within 10% of the expected value of D . Such a high precision could not be achieved using fluorophores as GFP or synthetic dyes as quantum dots, because their low signal provides a low spatial resolution, and their bleaching or blinking behavior make it impossible to collect long trajectories.

Given the challenges to extract a precise value of the diffusion coefficient, the analysis of changes in mobility needs extra care. We simulated traces with ‘gaps’ in the diffusion, as it can occur when a particle is temporarily immobilized, for example by specific binding to a cellular structure. The detectability of such gaps depends critically on the difference in the diffusion before and during the binding, determined mainly by the size of the ligands, and the length of the binding event. In our conditions and optimizing the MSD analysis as described, the detection of the gap was possible with a probability equal or higher than 50% only when the gap was longer than 20 s and the D in the gap was less than 5 times smaller than the D in the rest of the trace. These findings are applicable for all types of SPT methods in which individual traces are analyzed without averaging. We expect that many events characterized by a short duration or inducing a limited change in diffusion are overlooked in such experiments because of the stochastic character of diffusion. In any case, using large particles may produce brighter and more stable signals, but reduces the diffusion coefficient, making the difference in D between free and immobile particles smaller.

2.6 Supplementary figures

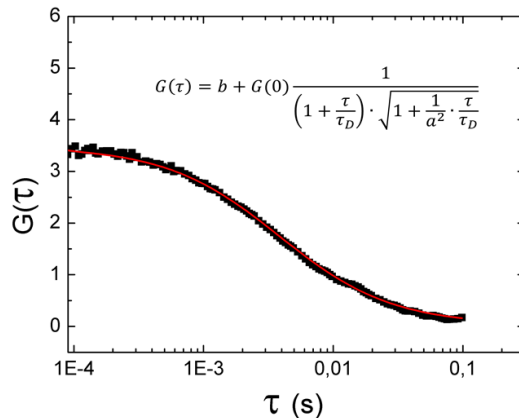


Figure S1

Fluorescence correlation spectroscopy on a solution of 47 nm x 14 nm GNRs in water. The fit gave $\tau_D = 3,85 \times 10^{-3} \text{ s}$. From τ_D a $D = 7,5 \times 10^{-2} \mu\text{m}^2/\text{s}$ is calculated. The hydrodynamic radius, calculated using Eq. 2.4, is 29,1 nm. The equivalent radius of our GNRs is 21 nm. Subtracting this value from the hydrodynamic radius, we obtained a PEG layer radius of 8.1 nm. The FCS experiment was performed on the setup described in [29].

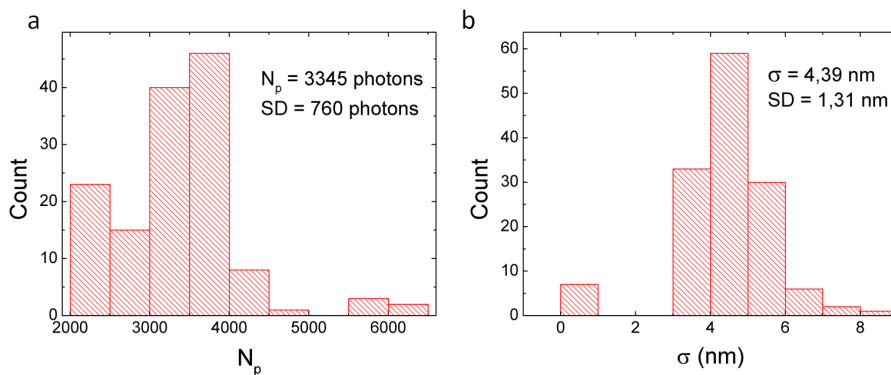
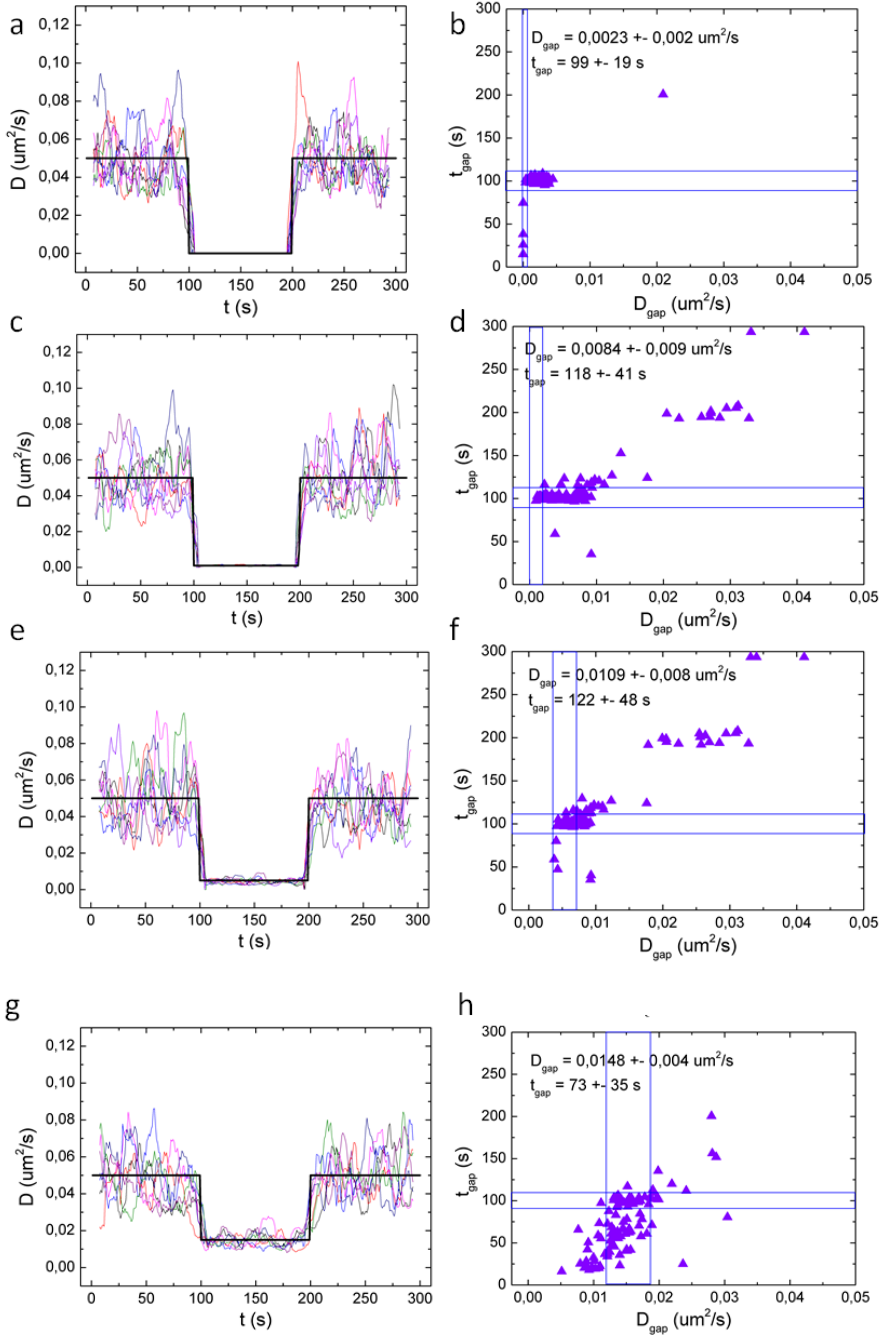


Figure S2

The distribution of a) the number of collected photons N_p and b) the positional accuracies σ obtained in our setup. GNRs of 47 nm x 14 nm and 53 nm x 16 nm in 95% glycerol were used. σ was obtained from N_p using Eq. 2.1.



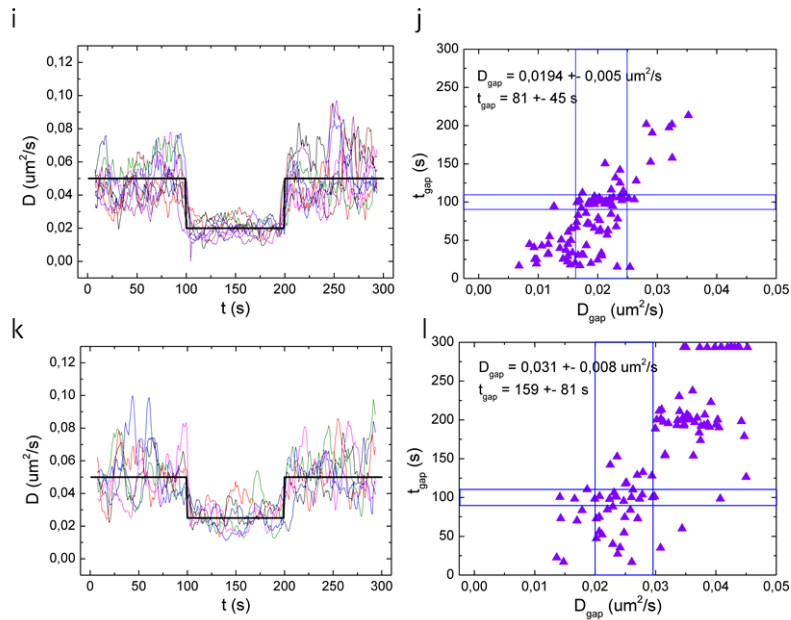
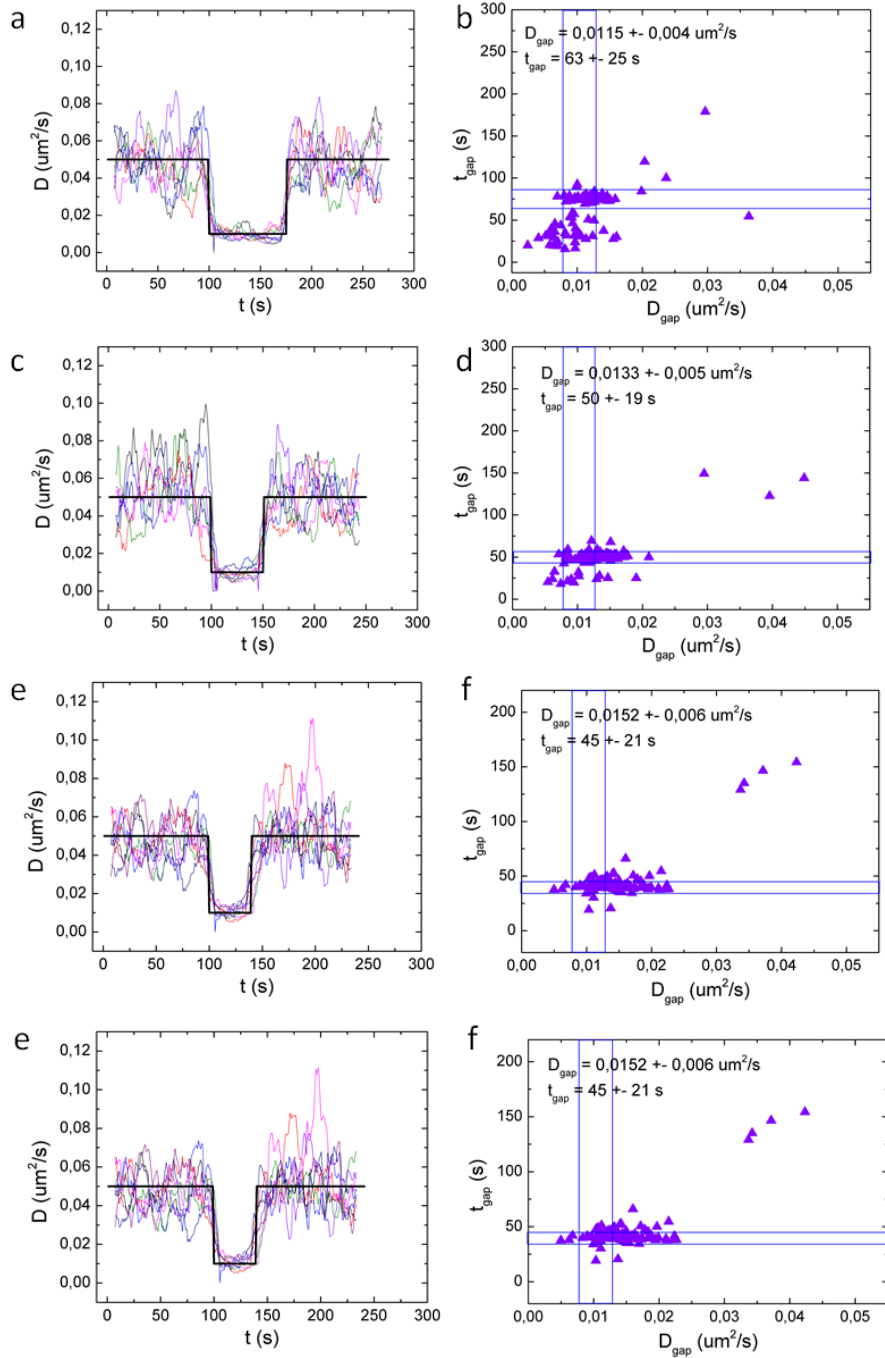


Figure S3

Detectability of changes in mobility in simulated traces with different D_{gap} . a,c,e,g,i,k) $D(t)$ plots obtained from the rolling-window analysis. b,d,f,h,j,l) Scatter plots containing t_{gap} vs D_{gap} . The simulated $D(t)$ (black line) is overlapped to the detected D plots (color lines). The D outside the gap was $0.05 \mu\text{m}^2/\text{s}$; while $D_{\text{gap}} = 0 \mu\text{m}^2/\text{s}$ in a,b, $D_{\text{gap}} = 0.001 \mu\text{m}^2/\text{s}$ in c,d, $D_{\text{gap}} = 0.005$ in e,f, $D_{\text{gap}} = 0.015 \mu\text{m}^2/\text{s}$ in g,h, $D_{\text{gap}} = 0.020 \mu\text{m}^2/\text{s}$ in i,j, and $D_{\text{gap}} = 0.025 \mu\text{m}^2/\text{s}$ in k,l. The ranges of correct D_{gap} and t_{gap} are highlighted with blue lines in the scatter plot. The traces were analyzed using a rolling window size of 15 s and a Welch sample of 15 points.



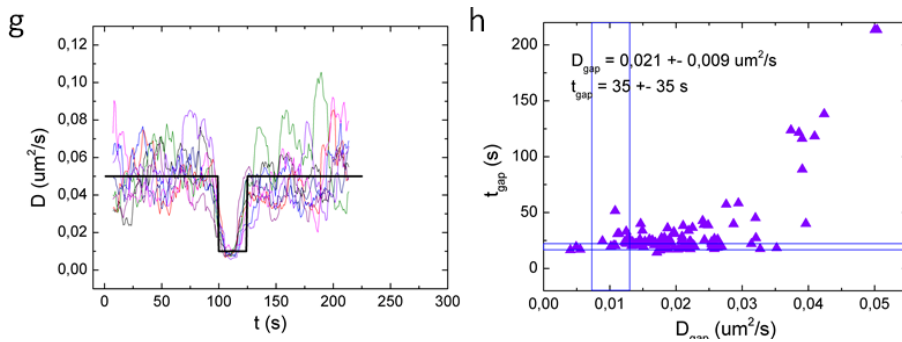


Figure S4

Detectability of changes in mobility in simulated traces for different durations of the gap. a,c,e,g,i) $D(t)$ plots obtained from the rolling-window analysis. b,d,f,h,l) Plots of D in function of the length of the detected gaps are shown for more D s tested. The simulated $D(t)$ (black line) is overlapped to the detected D plots (color lines). The D outside the gap was $0,05 \mu\text{m}^2/\text{s}$ and D_{gap} is $0,01 \mu\text{m}^2/\text{s}$. $t_{\text{gap}} = 75 \text{ s}$ in a,b, $t_{\text{gap}} = 50 \text{ s}$ in c,d, $t_{\text{gap}} = 40 \text{ s}$ in e,f, $t_{\text{gap}} = 25 \text{ s}$ in g,h and $t_{\text{gap}} = 20 \text{ s}$ in i,l. The ranges of correct D_{gap} and t_{gap} are highlighted with blue lines in the scatter plot. The traces were analyzed using a rolling window size of 15 s in all three cases, and a Welch sample of 15 points for the first four cases, and 10 points for the last case.

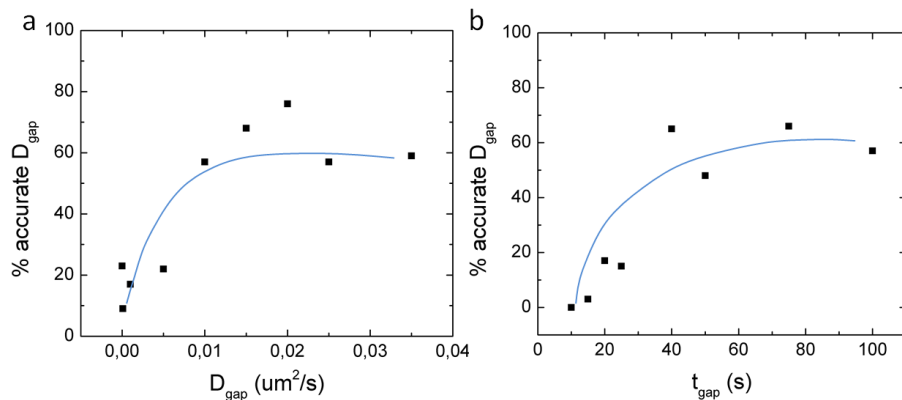


Figure S5

Percentage of detections of accurate D_{gap} detection for different values of D_{gap} and t_{gap} . The percentage of D_{gap} within 20% of the input is shown, for different values of a) D_{gap} and b) t_{gap} . Every point is obtained from 100 simulations of the trajectory containing a gap. The D outside the gap is $0,05 \mu\text{m}^2/\text{s}$, $t_{\text{gap}} = 100 \text{ s}$ and $D_{\text{gap}} = 0,01 \mu\text{m}^2/\text{s}$, if not stated otherwise. Lines are a guide to the eye.

GNR sample	D ($\mu\text{m}^2/\text{s}$)	measured D ($\mu\text{m}^2/\text{s}$)		
		all traces	traces > 40 points	traces > 80 points
47 nm x 14 nm, 90% glycerol	0.065 \pm 0.003	0.04 \pm 0.02	0.043 \pm 0.02	0.05 \pm 0.01
47 nm x 14 nm, 95% glycerol	0.03 \pm 0.001	0.02 \pm 0.01	0.022 \pm 0.005	0.025 \pm 0.003
53 nm x 16 nm, 95% glycerol	0.028 \pm 0.003	0.02 \pm 0.01	0.022 \pm 0.006	0.026 \pm 0.005

Table S1

Comparison of the diffusion coefficients calculated using the Stokes-Einstein relation with experimental data. The expected values were calculated assuming a temperature of 25 degrees and using the equivalent radius (Eq. 2.5). The expected variations in D were calculated according to the size dispersion within the sample. The table reports values of experimental D obtained using all the traces, or only traces longer than 40 points and 80 points.

BIBLIOGRAPHY

- [1] Laurent Holtzer, Tobias Meckel, and Thomas Schmidt. “Nanometric three-dimensional tracking of individual quantum dots in cells”. In: *Applied Physics Letters* 90.5 (Feb. 2007), p. 053902. ISSN: 00036951.
- [2] Ken Ritchie et al. “Detection of non-Brownian diffusion in the cell membrane in single molecule tracking.” In: *Biophysical journal* 88.3 (Mar. 2005), pp. 2266–77. ISSN: 0006-3495.
- [3] Olivier Seksek, Joachim Biwersi, and A.S. Verkman. “Translational Diffusion of Macromolecule-sized Solutes in Cytoplasm and Nucleus”. In: *The Journal of Cell Biology* 138.1 (July 1997), pp. 131–142. ISSN: 0021-9525.
- [4] M J Saxton. “Single-particle tracking: the distribution of diffusion coefficients.” In: *Biophysical journal* 72.4 (Apr. 1997), pp. 1744–53. ISSN: 0006-3495.
- [5] Michael J. Saxton and Ken Jacobson. “Single-Particle Tracking: Applications to Membrane Dynamics”. en. In: *Annual Review of Biophysics* (Nov. 2003).
- [6] Hazen P Babcock, Chen Chen, and Xiaowei Zhuang. “Using single-particle tracking to study nuclear trafficking of viral genes.” In: *Biophysical journal* 87.4 (Oct. 2004), pp. 2749–58. ISSN: 0006-3495.
- [7] J Suh. “Real-time multiple-particle tracking: applications to drug and gene delivery”. In: *Advanced Drug Delivery Reviews* 57.1 (Jan. 2005), pp. 63–78. ISSN: 0169409X.
- [8] Russell E Thompson, Daniel R Larson, and Watt W Webb. “Precise nanometer localization analysis for individual fluorescent probes.” In: *Biophysical journal* 82.5 (May 2002), pp. 2775–83. ISSN: 0006-3495.

- [9] Laurent Cognet, Cécile Leduc, and Brahim Lounis. “Advances in live-cell single-particle tracking and dynamic super-resolution imaging”. In: *Current Opinion in Chemical Biology* 20 (June 2014), pp. 78–85. ISSN: 13675931.
- [10] Johan Elf, Gene-Wei Li, and X Sunney Xie. “Probing transcription factor dynamics at the single-molecule level in a living cell.” en. In: *Science (New York, N. Y.)* 316.5828 (May 2007), pp. 1191–4. ISSN: 1095-9203.
- [11] Ariel Michelman-Ribeiro et al. “Direct measurement of association and dissociation rates of DNA binding in live cells by fluorescence correlation spectroscopy.” In: *Biophysical journal* 97.1 (July 2009), pp. 337–46. ISSN: 1542-0086.
- [12] H Qian, M P Sheetz, and E L Elson. “Single particle tracking. Analysis of diffusion and flow in two-dimensional systems.” In: *Biophysical journal* 60.4 (Oct. 1991), pp. 910–21. ISSN: 0006-3495.
- [13] Xavier Michalet. “Mean square displacement analysis of single-particle trajectories with localization error: Brownian motion in an isotropic medium.” In: *Physical review. E, Statistical, nonlinear, and soft matter physics* 82.4 Pt 1 (Oct. 2010), p. 041914. ISSN: 1550-2376.
- [14] Marija Vrljic et al. “Translational diffusion of individual class II MHC membrane proteins in cells.” In: *Biophysical journal* 83.5 (Nov. 2002), pp. 2681–92. ISSN: 0006-3495.
- [15] Maxime Dahan et al. “Diffusion dynamics of glycine receptors revealed by single-quantum dot tracking.” en. In: *Science (New York, N. Y.)* 302.5644 (Oct. 2003), pp. 442–5. ISSN: 1095-9203.
- [16] V Hlady, D.R Reinecke, and J.D Andrade. “Fluorescence of adsorbed protein layers”. In: *Journal of Colloid and Interface Science* 111.2 (June 1986), pp. 555–569. ISSN: 00219797.
- [17] Valeria Levi, QiaoQiao Ruan, and Enrico Gratton. “3-D particle tracking in a two-photon microscope: application to the study of molecular dynamics in cells.” In: *Biophysical journal* 88.4 (Apr. 2005), pp. 2919–28. ISSN: 0006-3495.

-
- [18] Yu Li, Ying Hu, and Hu Cang. “Light sheet microscopy for tracking single molecules on the apical surface of living cells.” In: *The journal of physical chemistry. B* 117.49 (Dec. 2013), pp. 15503–11. ISSN: 1520-5207.
- [19] Bram van den Broek et al. “Parallel nanometric 3D tracking of intracellular gold nanorods using multifocal two-photon microscopy.” In: *Nano letters* 13.3 (Mar. 2013), pp. 980–6. ISSN: 1530-6992.
- [20] Babak Nikoobakht and Mostafa A. El-Sayed. “Preparation and Growth Mechanism of Gold Nanorods (NRs) Using Seed-Mediated Growth Method”. In: *Chemistry of Materials* 15.10 (May 2003), pp. 1957–1962. ISSN: 0897-4756.
- [21] Elliot L. Elson and Douglas Magde. “Fluorescence correlation spectroscopy. I. Conceptual basis and theory”. In: *Biopolymers* 13.1 (Jan. 1974), pp. 1–27. ISSN: 0006-3525.
- [22] Kim I Mortensen et al. “Optimized localization analysis for single-molecule tracking and super-resolution microscopy”. In: *Nature Methods* 7.5 (May 2010), pp. 377–381. ISSN: 1548-7091.
- [23] B. L. Welch. “The Generalization of Student’s Problem when Several Different Population Variances are Involved”. In: *Biometrika* 34.1/2 (1974), pp. 28–35.
- [24] Femke L Groeneweg et al. “Quantitation of glucocorticoid receptor DNA-binding dynamics by single-molecule microscopy and FRAP.” In: *PloS one* 9.3 (Jan. 2014), e90532. ISSN: 1932-6203.
- [25] Jason Gorman and Eric C Greene. “Visualizing one-dimensional diffusion of proteins along DNA.” In: *Nature structural & molecular biology* 15.8 (Aug. 2008), pp. 768–74. ISSN: 1545-9985.
- [26] Sébastien Huet et al. “Analysis of transient behavior in complex trajectories: application to secretory vesicle dynamics.” In: *Biophysical journal* 91.9 (Nov. 2006), pp. 3542–59. ISSN: 0006-3495.
- [27] R Simson, E D Sheets, and K Jacobson. “Detection of temporary lateral confinement of membrane proteins using single-particle tracking analysis.” In: *Biophysical journal* 69.3 (Sept. 1995), pp. 989–93. ISSN: 0006-3495.

- [28] Petter Hammar et al. “Direct measurement of transcription factor dissociation excludes a simple operator occupancy model for gene regulation”. In: *Nature Genetics* 46.4 (Feb. 2014), pp. 405–408. ISSN: 1061-4036.
- [29] W J A Koopmans et al. “spFRET using alternating excitation and FCS reveals progressive DNA unwrapping in nucleosomes.” In: *Biophysical journal* 97.1 (July 2009), pp. 195–204. ISSN: 1542-0086.

CHAPTER 3

DELIVERY AND SINGLE-PARTICLE TRACKING OF GOLD NANORODS IN LIVE CELLS

Gold nanorods are promising labels for two-photon single-particle tracking in live cells, due to their brightness, stability and the use of low-energy photons, which reduces photodamage. We acquired 3D movies of gold nanorods in cells using a two-photon multifocal scanning microscope. We tested delivery of gold nanorods with different techniques: incubation, electroporation, cell-squeezing and single-cell microinjection in HeLa and COS1 cells, and injection in the yolk of zebrafish embryos cells. For each technique we evaluated the delivery efficiency and the short-term consequences on cell viability. When the delivery of gold nanorods was successful, we analyzed their mobility by mean squared displacement analysis. We found three populations of nanorods: immobile, freely diffusing and diffusing within a confinement. In zebrafish embryos cells all the mobile rods were freely diffusing, in HeLa cells the diffusing rods were about half and in COS1 cells about 70% of the total. The diffusion coefficients were around $0.006 \mu\text{m}^2/\text{s}$, and the confinement radius was around $0.7 \mu\text{m}$. By specific functionalization of gold nanorods with selected proteins, high-precision single-particle tracking of these particles can in the future be used to follow the dynamics of proteins in live cells in 3D with nm accuracy.

Single-Particle Tracking of Gold Nanorods in Live Cells, S.Carozza, V. Keizer, A. Boyle, A. Kros, M. Schaaf, J. van Noort. (in preparation).

3.1 Introduction

Single-molecule imaging has become an important technique for resolving the spatial and temporal distribution of molecules in cells. The choice of a suitable label is extremely important for single-molecule imaging *in vivo*: the brightness of the label determines the localization accuracy of the molecule of interest, and its stability in time limits the duration of the experiment. The signal of fluorescent proteins is typically rather weak for detection with high precision in a noisy environment like a living cell, and they exhibit low photostability due to bleaching or blinking. Organic dyes generally have better photophysical properties, but are still limited in their use.

The advantages of using gold nanoparticles (GNPs) as labels *in vivo* are many. The luminescence of GNPs is higher than the fluorescence of organic dyes, and does not suffer from bleaching or blinking. Among GNPs, gold nanorods (GNRs) can be excited in the IR region of light, where absorption by cells, and consequently photodamage, are minimized. The properties and advantages of GNRs are discussed in more detail in Chapter 1, Section 1.3.

The use of gold nanoparticles for applications in live cells was reported in many publications. Some focused on the mechanisms of uptake and localization of the particles inside cells (for a detailed review on the cell uptake of GNPs see [1]). In some cases, nuclear targeting of GNPs was achieved using nuclear localization signal (NLS) [2–4]. The efficiency of GNPs to generate highly localized heat when excited, joined to their easy functionalizability, makes them a preferred tool for thermal cancer therapy [5]. The uptake of GNRs in HeLa cells was studied by Ding [6] and Oyelere [7], who also functionalized GNRs with NLS for nuclear targeting. Huang and Durr [8, 9] used GNRs to specifically detect cancer cells. To our knowledge, a quantification of the dynamics of GNRs in live cells by single-particle tracking was performed only by Van den Broek [10]. As GNRs are very promising tools to study the dynamic of proteins *in vivo*, we believe that a more detailed study of their mobility inside cells is of high interest.

When passive delivery methods are used, nanoparticles enter the cell by endocytosis, and they remain trapped in vesicles [1, 11]. We used multiple alternative delivery methods to test whether GNRs can be introduced in cells without the internalization into vesicles, and whether

the choice of the delivery method has an influence on the mobility of the GNRs. Based on the images of cells taken shortly after the delivery, we evaluated the delivery efficiency and the impact of each method on the cells health.

Imaging was performed with a two-photon multifocal scanning microscope, which offers wide-field illumination and high localization accuracy in 3D. Trajectories of individual GNRs in the cells were obtained and further analyzed to quantify their mobility. We first inspected the MSD histograms of all traces and identified populations that exhibited different types of mobility. Then we performed a mean squared displacement analysis on single traces, to quantify mobility parameters. The difference in the mobility obtained for GNRs delivered with different methods is presented and discussed.

3.2 Materials and methods

Gold nanorods preparation

GNRs with a size of approximately 40 nm x 10 nm were prepared by seed-mediated synthesis [12]. Bifunctional α -mercapto- ω -amino Polyethylene-glycol-5000 (PEG-5000) was then added in excess to the GNRs solution, resulting in complete coverage of the GNRs surface with a PEG layer. PEGylation of GNRs is used to reduce cytotoxicity in cells [13]. The solution was left to stir at room temperature overnight before the GNRs were centrifuged, the supernatant removed and the GNRs resuspended in phosphate buffered saline (PBS).

Cell culture

We tested two types of mammalian cells: HeLa and COS1. Cells were cultured in Dulbecco's modified eagle's medium (DMEM, Gibco) supplemented with 10% fetal calf serum (FCS) and were kept at 37 °C and 5% CO₂.

Delivery of gold nanorods in cells

Incubation of GNRs with mammalian cells

Incubation is the simplest technique to deliver particles into cells. A solution containing particles is added to the medium and cells are left in incubation, as depicted in Fig. 3.1a. The plasma membrane is impermeable for small solutes, while larger particles or particles with a high surface charge can be taken up by cells via endocytosis. The cells were trypsinized to detach them from the surface they adhered to. After trypsinization, a 30 nM GNR solution in PBS was added to the culture. After 5 minutes cells were placed in a well plate containing a glass coverslip immersed under DMEM containing FCS, and incubated for at least one hour.

Electroporation into mammalian cells

Delivery through electroporation is obtained by placing a cuvette containing cells and particles between two electrodes. Upon application of a voltage difference, the membrane forms temporary nanometer size pores due to local fluctuations in the transmembrane voltage. Small particles diffusing in the cuvette can thus enter the cells. The procedure is depicted in Fig. 3.1b. When fibronectin coated coverslips were used, 250 μ l 10 μ g/ml fibronectin in PBS was placed on coverslips and incubated for one hour at 37 °C. Subsequently, coverslips were washed once with an excess of PBS. HeLa or COS-1 cells were trypsinized, spun down and resuspended in 100 μ l nucleofector solution (Lonza) and placed into cuvettes containing 3 nM of GNR solution. Next, cells were electroporated using the nucleofector II device (Lonza). Cells were spun down and resuspended in 800 μ l DMEM containing 10% FCS. Cells were subsequently plated onto coverslips and left to adhere at least 30 minutes prior to imaging.

Squeezing of GNRs into mammalian cells

This method involves pushing cells contained in a tube through a small microfluidic channel by applying pressure on one side of the tube [14]. Due to the shearing stress that the cells experience in the narrow channel, gaps are created in the plasma membrane. Particles can then enter the cells via diffusion through these gaps. A scheme of the squeezing method is depicted in Fig. 3.1c. Before the experiment, cells were trypsinized, spun down, washed and suspended in 100 μ l PBS. Freshly prepared 15

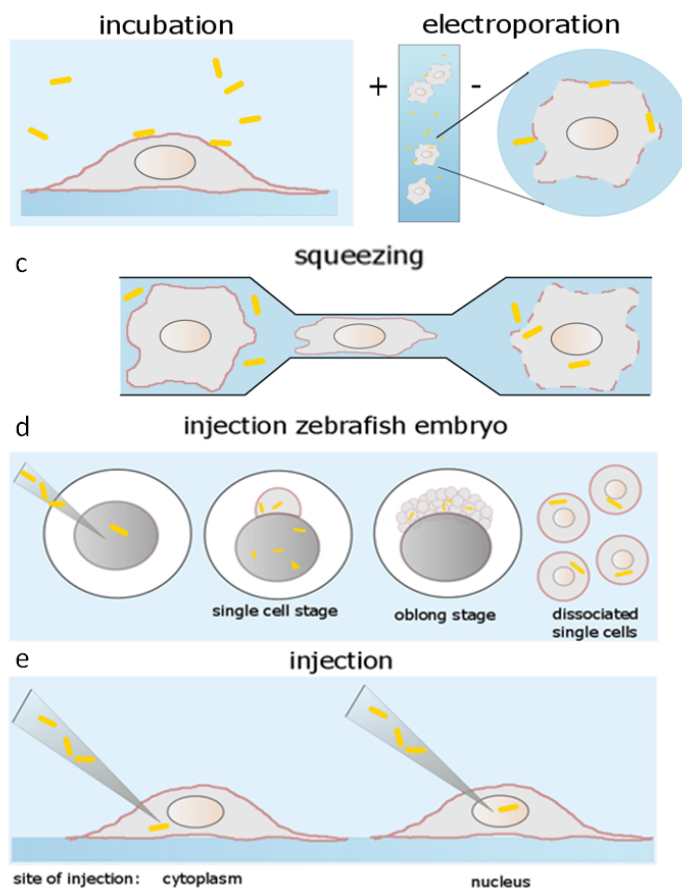


Figure 3.1

Schematic illustration of the methods used to deliver GNRs in cells. a) Incubation with cells, b) electroporation into cells, c) cell-squeezing, d) injection in the yolk of zebrafish embryos cells, e) microinjection in single cells. Drawing are not to scale.

nM GNR solution was added and the solution was flowed through the squeezing device (SQZ Biotech), using a pressure of 344 kPa. After 1.5 minutes 100 μ l DMEM containing 10% FCS was added.

Injection of GNRs into zebrafish embryos

The yolk of a zebrafish embryo egg is surrounded by a chorion that can be easily visualized under a microscope and penetrated using a mi-

micropipette loaded with nanoparticles solution. When the egg is fertilized, a cell develops on top of the chorion. After multiple rounds of cell division, over a thousand cells result that take up the particles that were injected into the yolk. Fig. 3.1d depicts the injection procedure. Zebrafish were raised, grown and kept at 28.5 °C. Embryos were harvested and kept in egg water (Instant Ocean sea salts). Manually pulled micropipettes were loaded with 5 μ l 0.3 nM GNRs. Injections were carried out at the single cell stage according to the protocol reported in [15]. The injected volume was equal to approximately one third of the yolk sac volume. Following injection, embryos were left to develop until the oblong stage at 28 °C. Embryos were then dechorionated using 1 mg/mL pronase (Sigma Aldrich) on a rotating stage for 30 seconds. Subsequent pipetting of the embryos resulted in dechoriation of the embryos. To dissociate the zebrafish cells, the embryos were incubated with 1 ml of calcium/magnesium free solution for 30 seconds. Cells were spun down and resuspended in 500 μ l PBS. Zebrafish embryos cells were allowed to set for at least 30 minutes prior to imaging.

Injection of GNRs into mammalian cells

Fig. 3.1e depicts the direct injection of GNRs in single cells using micropipettes to penetrate the plasma membrane of individual cells. Either the cytoplasm or the nucleus of each individual adhering cell can be injected separately. One day prior to injection, cell samples were placed onto coverslips and covered with 1 ml of DMEM. Using a diamond pen two lines, crossing at a 30° angle, were scratched into the bottom of the coverslip to make a reference marker. Subsequently, the sample was placed under an inverted microscope using a 20x objective (Olympus). This microscope contained an additional support beam holding an injection arm (Eppendorf). A femtoject II needle (Eppendorf) was loaded with 3 μ l 0.12 nM GNR solution in PBS using a microloader tip (Eppendorf). The micropipette was placed in the holder of the injection arm and connected to a femtojet pump (Eppendorf). A constant pressure of 150-250 hPa was supplied inducing a constant flow of GNR solution. Once the tip of the micropipette and cells were focused in the same plane, approximately ten cells were injected without interruption. Cells were incubated at 37 °C and 5% CO₂ for 30 minutes prior to imaging.

Imaging and tracking

We used a home-made two-photon multifocal scanning microscope for imaging. A pulsed IR laser (Chameleon Ultra, Coherent) was used for the excitation. A diffractive optical element (DOE, custom-made by Holoeye Photonics) divided the excitation beam in an array of 25x25 focal spots. The array was then scanned by a fast scanning mirror (FSM-300, Newport) to obtain a squared homogenous illumination. Using a piezo-actuator (P-726 Pifoc, PI) we moved the objective (60x APOTIRF, Nikon) in the z direction to acquire 3D images of the sample. Thanks to the wide-field illumination in 3D, we could image GNRs within the entire volume of one or more cells. A white-light LED placed above the sample was used for transmission images of the cells. A more detailed description of the setup can be found in Chapter 1, Section 1.2.3.

To follow the GNRs and monitor cells at the same time, a stack of fluorescence images and one transmission image were collected for every time point. The image size was typically 400 x 400 pixels (about approximately 60 μm x 60 μm). 3D stacks were made of 15-18 2D images, taken 0.5 μm from each other and acquired with a frame rate of 8 Hz. Fluorescence images were acquired with excitation at 770 nm. Fig. 3.2a shows an example of transmission image. A two-photon luminescence image made by a projection of all slices in a 3D stack is shown in Fig. 3.2b. Fig. 3.2c is a z-y reconstruction of the 3D stack, built by interpolating the pixel intensities between the z slices. Typically we acquired movies that lasted 10 minutes. In every frame of the 3D movie we localized small volumes of interest (typically 10 x 10 pixels in x, y and 5 slices in z) around each bright peak corresponding to a GNR. Then, we performed a 3D Gaussian fit on each volume of interest to obtain nanometer accurate 3D coordinates of the GNRs. Fig. 3.2d shows an example of the GNRs peaks, overlapped with the transmission image. The coordinates of a GNR in each time point were then connected into a trace, using a nearest-neighbor algorithm. In Fig. 3.2e the GNR traces are overlapped with the transmission image.

Mobility analysis

To quantify GNR mobility, we performed a mean squared displacement (MSD) analysis of the traces [16]. The MSD of a trajectory, as described

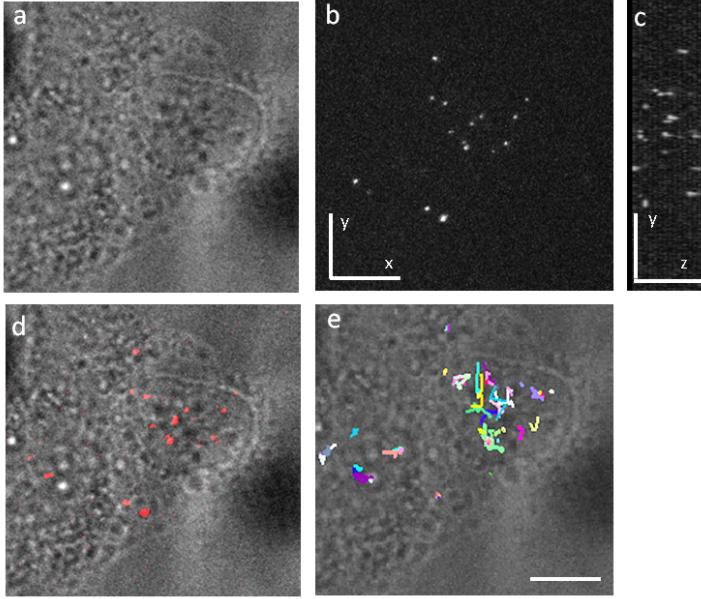


Figure 3.2

Image acquisition and traces reconstruction. a) An image of a HeLa cell microinjected with GNRs. A transmission image is collected for every 3D stack of fluorescence images. b) An example of a single frame in the 3D stack. c) A z-y image of the 3D stack. d) The overlap of a transmission image with the projection of all the two-photon luminescence frames in a stack. The two-photon signal is depicted in red. An overlap of the GNRs traces and the transmission image is shown in e), where each color represents a different trace. The scale bars correspond to 10 μm .

in Chapter 2, is defined as the average of the squared displacements covered by the particle in time steps of duration τ . The diffusion coefficient D is used to quantify the mobility of a particle. D depends on the size of the particle and on the temperature and viscosity of the medium, according to the Stokes-Einstein equation (Eq. 2.4 in Chapter 2).

If the particle is freely diffusing, the MSD is a linear function of τ with a slope that depends on the diffusion coefficient D :

$$MSD(\tau) = 6\sigma^2 + 6D\tau \quad (3.1)$$

and an offset that depends on the localization accuracy σ of the system. Fig. 3.3a shows an example of a freely diffusing GNR. Its MSD plot and

the fit with Eq. 3.1 are shown in Fig. 3.3b.

When the movement of the particle is directional (superdiffusion), a quadratic component, dependent on the velocity v , introduces a positive curvature in the MSD:

$$MSD(\tau) = 6\sigma^2 + 6D\tau + v^2\tau^2 \quad (3.2)$$

If the diffusion of the particle is confined (subdiffusion or confined diffusion) the MSD exhibits a negative curvature. The shape of MSD for a trace confined within a spherical area approximates to [17]:

$$MSD(\tau) = 6\sigma^2 + \frac{6R^2}{5} - 12R^2 \sum_{n=1}^{\infty} \exp\left[-\beta_{1n}^2 \frac{Dt}{R^2}\right] \frac{1}{-\beta_{1n}^2(-\beta_{1n}^2 - 1)} \quad (3.3)$$

where R is the confinement size and β_{1n} are constants given by the solutions of the spherical Bessel function of the first order. An example of a confined trace and its MSD are shown in Fig. 3.3c,d.

The localization accuracy of the system and the number of points in a trajectory determine the precision of its MSD and thus the precision of D (as explained in detail in Chapter 2, Section 2.3.2, [18]). The error on each MSD point is strongly influenced by the length of the trajectory: the MSD points have increasing uncertainties, due to the decreasing number of steps used to calculate the mean (see Eq. 2.3 in Chapter 2). The presence of a curvature in the MSD plot can therefore be hidden in the standard deviation of the MSD points. For this reason, choosing the mobility model based on single traces is not reliable when dealing with large fluctuations in MSD due to short trajectories. Alternatively, we analyzed the distribution of the MSD of all traces at different time steps to identify populations following different models. Based on changes in the ensemble distributions, a threshold was set to divide different modes of mobility. MSD analysis was subsequently performed on individual traces to quantify the mobility parameters of single GNRs. This approach allows for distinguishing free from confined populations, but unfortunately not from active populations.

Traces shorter than 4 time points (about 8 s) were excluded from the analysis. To identify immobile GNRs we used a threshold based on the localization accuracy of the setup, calculated as explained in Chapter 2 (Eq. 2.1). The localization accuracy is inversely proportional to the square root of the photon emission intensity of the GNRs (Fig. S1).

Typically, the localization accuracy in 3D was about 40 nm. GNRs showing a MSD at any time delay lower than the square of the localization accuracy, multiplied by 6 (i.e. $0.0096 \mu\text{m}^2$) were considered immobile. An example of immobile trace, its MSD and fit are plotted in Fig. 3.3e,f.

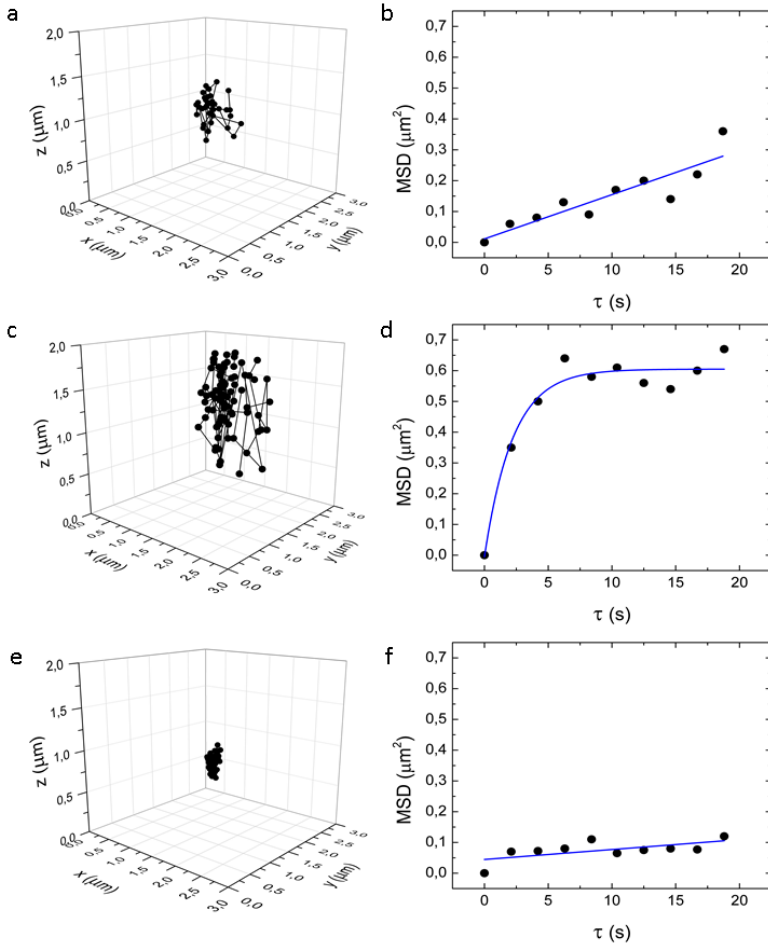


Figure 3.3

Examples of time traces of single GNRs showing 3 different modes of movement, along with the corresponding MSD plot. a) Trace of a freely diffusing GNR and b) its MSD plot fitted to Eq. 3.1. c) Trace of a GNR featuring confined diffusion and d) its MSD fitted to Eq. 3.3. e) Trace of an immobile GNR and f) its MSD plot fitted to Eq. 3.1.

The MSD analysis of GNRs traces was performed in LabVIEW. To

assess the significance of differences in the mobility of GNRs from different samples, we used a Single-Factor Analysis of Variance (ANOVA), with a p-value threshold of 0.05. For non-normal distributions, the Kruskal-Wallis ANOVA test was used.

3.3 Results

3.3.1 Delivery in cells and considerations on cell viability

Fig. 3.4 shows some examples of HeLa cells after delivery of GNRs with different methods. The delivery through incubation in a solution containing GNRs was not successful: GNRs resided in the medium or were stuck around the external membrane (Fig. 3.4a, b). The round shape of the cells is due to the trypsinization process that disrupted the proteins involved in the adherence of the cell to the coverslip. HeLa cells containing GNRs delivered through electroporation are shown in Fig. 3.4c, d. In some cases, the coverslip was functionalized with fibronectin, to facilitate the cell adherence, but we did not observe any difference in cells spreading. The delivery was successful, but not all the cells looked healthy. The cells were imaged about 1 hour after electroporation. Fig. 3.4e, f shows two cells after undergoing cell-squeezing with GNRs. The delivery was not successful: we observed only GNRs outside cells or stuck around the external membrane. All the cells showed very poor conditions after the procedure: a large fraction died, while many of the survivors could not adhere properly to the glass. The images were taken about 1 hour after the squeezing procedure. Two images of HeLa cells microinjected with GNRs in the nucleus (Fig. 3.4g) and in the cytoplasm (Fig. 3.4h) are shown. The delivery was successful and most of the cells appeared in good condition, as judged by their shape. Cells were imaged about half an hour after the injection.

We also tested some of the delivery techniques in COS1 cells. Examples of the results are shown in Fig. 3.5. Incubation (Fig. 3.5a, b) was not successful, as in the case of HeLa cells. Also in the case of COS1 cells, the round shape is due to the trypsinization process. The delivery of GNRs through squeezing (Fig. 3.5c, d) was successful only in few cases. Similarly to HeLa cells, squeezed COS1 cells showed very poor conditions.

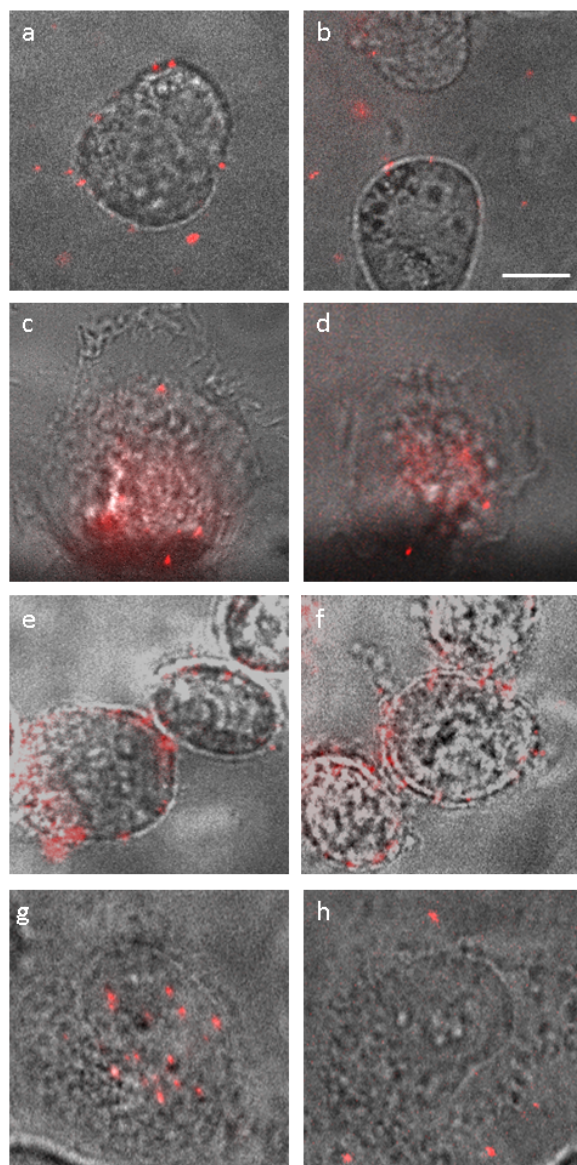
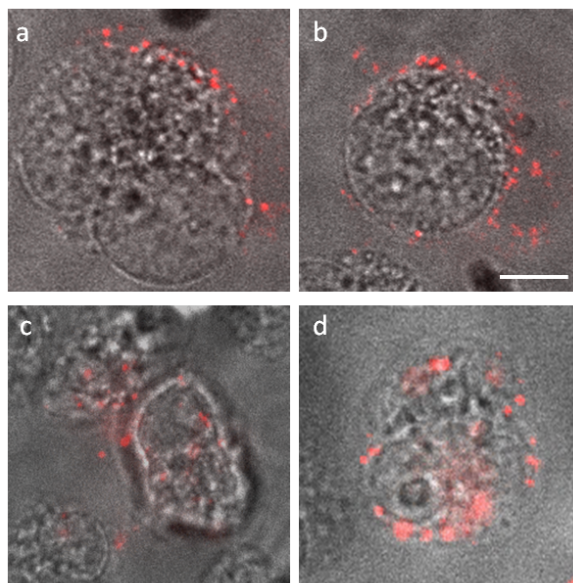
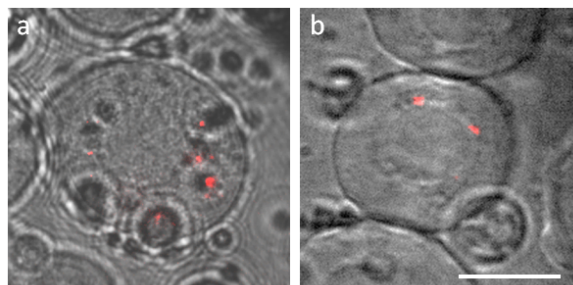


Figure 3.4

Images of HeLa cells after GNR delivery using different techniques. a,b) Two examples of cells incubated with GNRs after trypsinization. c, d) Two cells electroporated with GNRs. e,f) Two images of cells squeezed with GNRs. Two images of HeLa cells, microinjected g) in the nucleus and h) in the cytoplasm. Red marks indicate the two-photon luminescence signal of GNRs. The scale bar corresponds to 10 μm .

**Figure 3.5**

Images of COS1 cells after GNR delivery via different techniques. a,b) Two COS1 cells incubated in a solution containing GNRs after trypsinization. c,d) Two COS1 cells squeezed with GNRs. The scale bar corresponds to 10 μm .

**Figure 3.6**

Zebrafish embryo cells after delivery of GNRs through injection in the egg yolk. The scale bar corresponds to 10 μm .

Fig. 3.6 shows two zebrafish embryos cells after injection in the embryo yolk. The delivery efficiency was high and cells were in good conditions. Imaging was performed 6 hours after injection.

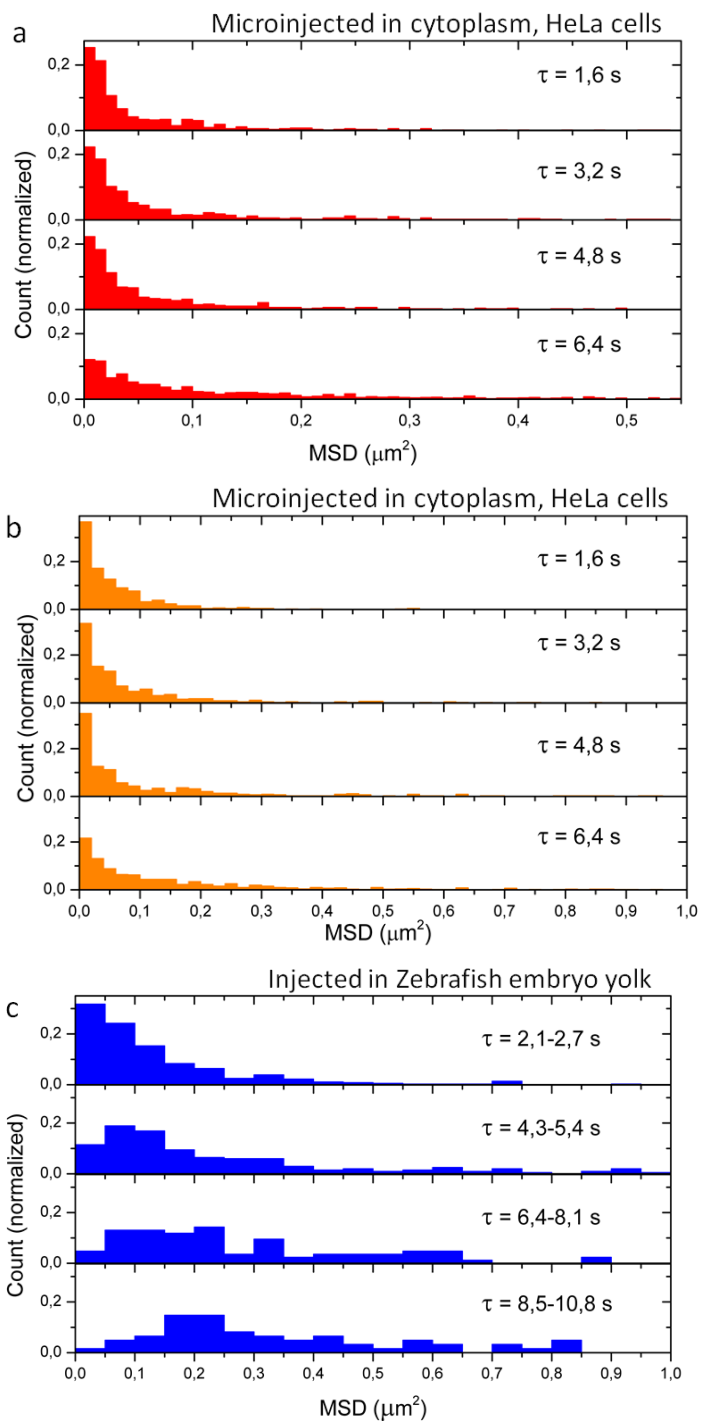
In conclusion, successful delivery was observed using electroporation and single-cell microinjection in HeLa cells, squeezing in COS1 cells and injection in the yolk of zebrafish embryos cells, though differences in cell viability were observed.

3.3.2 Mobility of gold nanorods in cells

We next analyzed the mobility of GNRs microinjected in the cytoplasm and in the nucleus of HeLa cells, delivered through electroporation in HeLa cells, through cell-squeezing in COS1 cells and injected into zebrafish embryos cells. In none of the cells we observed translocation of GNRs from the cytoplasm to the nucleus in the duration of the experiment (up to 3 hours after delivery).

In most of the cases, the GNRs traces were shorter than 1 minute (Fig. S1). A short trajectory results in relatively large errors in the MSD points. Thus, we could not reliably choose a model to fit the trace based on the slope of the MSD curve. Instead, we plotted the distributions of the MSD at different delays. Fig. 3.7 shows the histograms of the MSD for each GNR sample, for each time step, normalized for the total number of traces in the distribution. Next, we divided the traces in populations following different models by a visual inspection and thresholding of the MSD histograms in time.

The MSD histograms representing GNRs microinjected in cytoplasm are shown in Fig. 3.7a. We observed the presence of a stable population with MSD below $0.2 \mu\text{m}^2$ in all four time points, probably due to the presence of a confinement. Note that these MSDs all exceed the threshold for immobilization. MSD values higher than $0.1 \mu\text{m}^2$ for $\tau = 6.5 \text{ s}$, typically increased over time, a sign of free diffusion. We tested whether this mobile fraction is compatible with a population with a single diffusion coefficient D . From the center of the distribution at the last time point ($\tau = 6.4 \text{ s}$), we estimated D to be around $0.01 \mu\text{m}^2/\text{s}$. The width of the MSD expected for traces with a typical length of 20 points and a diffusion coefficient of $0.01 \mu\text{m}^2/\text{s}$ is however significantly smaller (Fig. S2) than the distribution shown in Fig. 3.7a.



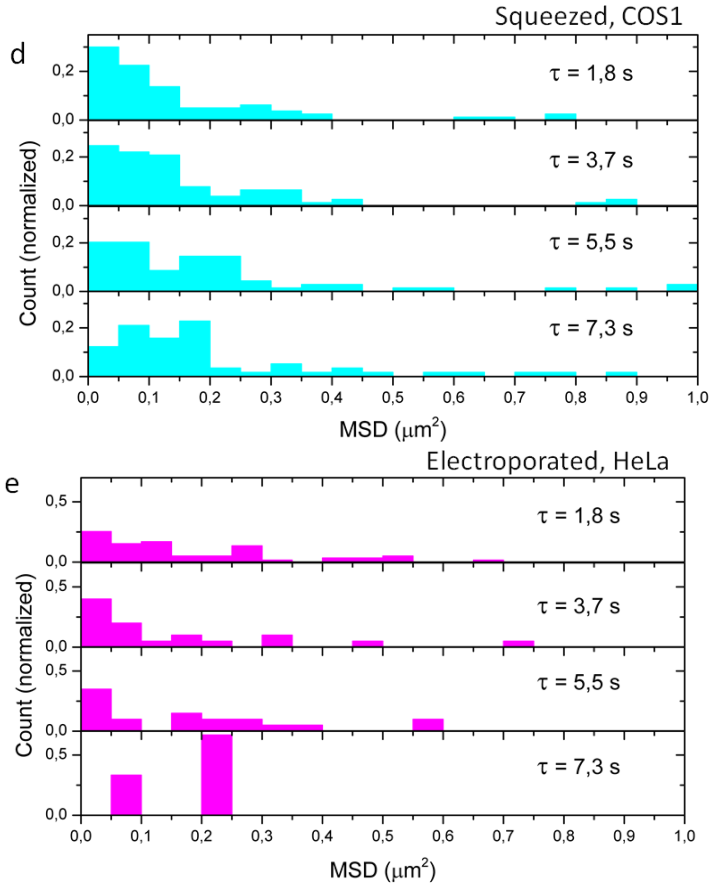


Figure 3.7

Histograms of MSD divided by time step. MSD histograms from traces of GNRs a) microinjected in cytoplasm of HeLa cells, b) microinjected in nucleus of HeLa cells, c) microinjected in zebrafish embryos cells, d) in squeezed COS1 cells and e) in electroporated HeLa cells. A small fraction, typically < 5%, exceeding $\text{MSD} = 1 \mu\text{m}^2$, is not shown. We attribute such fraction to artifacts originating from erroneous connection of peaks.

This result points to a variety of diffusion constants in this population that can be only be revealed by single-particle analysis.

Using a MSD threshold of $0.1 \mu\text{m}^2$, we distinguished between two populations. The first one appears to have a constant MSD, consistent with confined diffusion. The second population shows a growth of MSD with increasing time lags, indicative of free diffusion. We divided the traces into these two categories by setting a threshold of their MSD at 6.4 s. We fitted the MSD of individual traces belonging to the first population with Eq. 3.3, and we used Eq. 3.1 for the MSD of traces of the second population.

The MSD histograms of the GNRs injected in nucleus of HeLa cells (Fig. 3.7b) are very similar to the histogram of GNRs in cytoplasm. Therefore the two samples were analyzed in the same manner.

The MSD histograms of GNRs injected in zebrafish embryos cells reveal a different behavior (Fig. 3.7c). As opposed to GNRs in HeLa cells, we did not observe a population with MSD independent of the time lag: therefore we analyzed all traces with the free diffusion model. In this case, movies with different frame rates were acquired, resulting in multiple MSD series. To increase the sample size, we aggregated the MSD into single histograms.

In squeezed cells both a stable and a mobile population were found in the MSD histograms (Fig. 3.7d). The statistic was quite small as compared to microinjected GNRs. Because it is harder to draw a threshold between the two populations, we used the same threshold as used for the HeLa cells at $0.1 \mu\text{m}^2$. A time lag of 7.3 s was used to distinguish the two populations.

The MSD histograms of GNRs in electroporated cells are shown in Fig. 3.7e. The size of this sample is small, but nevertheless we can see a stable population at low MSD values. Note that the histogram at the fourth time point is built from only three traces; we considered these peaks to be outliers due to large fluctuations. We used again a threshold of $\text{MSD} = 0.1 \mu\text{m}^2$ at $\tau = 5.5$ s and distinguished two populations.

After dividing the populations in each sample, we analyzed the single traces with the corresponding diffusion (Eq. 3.1) or subdiffusing model (Eq. 3.3). We obtained a distribution of the diffusion coefficients and of the confinement sizes as shown in Fig. 3.8. The independence of the MSD of time lag of the confined population suggests that the particles reached the confinement within the first step: therefore we expected not to be able to fit the diffusion coefficient correctly in these traces, but only the confinement size. Given a confinement radius of 0.2-0.6 μm , we

estimate the diffusion coefficient of confined GNRs to be around 0.02-0.06 $\mu\text{m}^2/\text{s}$. Note that the MSD is larger than the expected positional accuracy, so these confined GNRs are indeed mobile.

The mobility parameters obtained are summarized in Table S1. In the table we reported the number of traces for each mode and the relative percentage on the total population, the median, the 1st and the 3rd quartiles of the parameter distribution. In both injected and electroporated HeLa cells, we found a fraction of immobile GNRs equal to about 15%. This fraction is almost absent in squeezed COS1 cells (1%), and it is higher in zebrafish embryos cells (30%). The freely diffusing population amounts to 42% of the traces in the case of GNRs microinjected in cytoplasm and 49% of the GNRs microinjected in nucleus, 57% of the GNRs in electroporated cells and 76% of the GNRs in squeezed cells. In zebrafish embryos cells we did not observe confined diffusion: all mobile rods (71%) appear to be freely diffusing.

Population	Parameter	Injection HeLa Cytoplasm	Injection HeLa Nucleus	Injection ZF embryos yolk	Squeezing COS1	Electrop. HeLa
Immobile	Pop. Size	125; 13%	107; 16%	24; 30%	1; 1%	7; 15%
Confined	Pop. Size	449; 45%	225; 35%	0	14; 23%	13; 28%
	Confinement (μm)	0.2 (0.1-0.4)	0.3 (0.2-0.4)		0.3 (0.2-0.5)	0.4 (0.3-1)
Freely Diffusing	Pop. Size	418; 42%	316; 49%	59; 70%	47; 76%	26; 57%
	D ($\mu\text{m}^2/\text{s}$)	0.006 (0.003-0.009)	0.007 (0.004-0.01)	0.004 (0.003-0.006)	0.006 (0.004-0.01)	0.006 (0.004-0.01)

Table 3.1

Mobility parameters of GNRs delivered in cells with different methods. The number of traces used for the statistics, the percentage relative to the total number of traces, the median, 1st and 3rd quartiles of the diffusion coefficient and of the confinement sizes are reported for the free and confined population.

The distribution of diffusion coefficients (Fig. 3.8a) presents comparable characteristics for different delivery methods. In none of the cases

we observed a normal distribution: the histograms are shown in Fig. S3. The diffusion coefficients (Table S1) have median values between 0.004 and 0.007 $\mu\text{m}^2/\text{s}$. No significant difference between the diffusion coefficients was found using a non-parametric ANOVA (Kruskal-Wallis) test.

In squeezed COS1 cells and in both injected and electroporated HeLa cells, we found a fraction of GNRs with mobility that appears to be confined. This fraction consists of 55% of the GNRs in the cytoplasm and 46% in the nucleus of microinjected cells, 23% in squeezed cells and 35% in electroporated cells. The distributions of confinement sizes are shown in Fig. 3.8b. In all four distributions a wide range of confinement sizes was observed, from 70 nm (below this limit we define GNRs as stuck) to 10 μm . The median values are between 0.2 μm and 0.4 μm . Outliers with large confinement sizes are present in all the cases but are especially numerous among GNRs in cytoplasm and nucleus of microinjected HeLa cells. However, we measured a larger number of samples for those measurements. The confinement sizes in squeezed and electroporated cells are a bit larger than in microinjected HeLa cells, but there is no significant difference between the four populations. Histograms of the confinement sizes distributions are plotted in Fig. S4.

3.4 Discussion and conclusion

In this study, we tested different methods to deliver GNRs in live cells: incubation with HeLa and COS1 cells, electroporation into HeLa cells, cell-squeezing of HeLa and COS1 cells, injection in zebrafish embryos cells and microinjection in single HeLa cells. We analyzed the mammalian cells shortly after delivery of GNRs, but had to wait a few hours in the case of zebrafish embryos cells to allow cell division. In the case of incubated cells we obtained a low number of GNRs. It is possible that not enough time was given to the GNRs to enter the cells [19]. Also for electroporated cells, waiting a longer time before imaging might increase the delivery efficiency [20], even though successful delivery has been reported few minutes after electroporation [21].

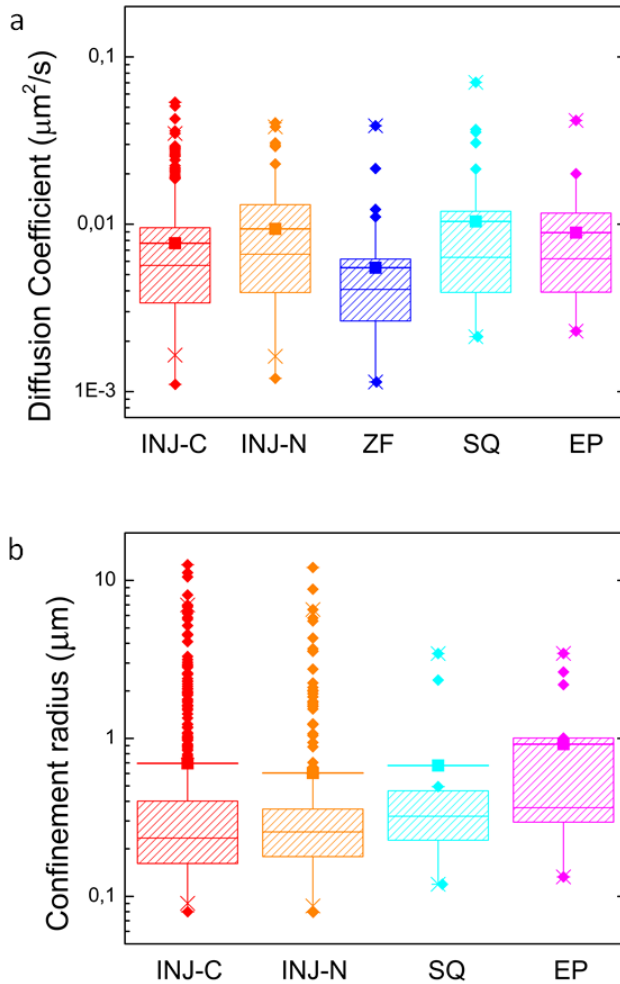


Figure 3.8

Distribution of mobility parameters for GNRs in cells. a) Distribution of diffusion coefficients of GNRs freely diffusing in cells and b) distribution of confinement sizes of GNRs undergoing confined diffusion in cells, split out by delivery technique. The box-plots are defined as follows: the box include data from the 25th to the 75th percentile; the vertical line goes up to the 90th percentile. Outliers above the 90th percentile are plotted. Crosses mark the 1st and 99th percentiles. The square on horizontal line indicates the average of the distribution, and the horizontal line without square indicates the median. Note that the sample sizes of microinjected cells in cytoplasm and nucleus (INJ-C and INJ-N) are much larger, explaining the larger number of outliers for these fractions.

Squeezed cells showed low delivery efficiency. Although cell-squeezing was reported to be successful with small particles [14], it was never performed using particles of a size comparable to our GNRs: it is possible that the pores created in the cell membrane by this method were not large enough. Nevertheless, we observed poor cell viability after squeezing that was not mentioned in previous reports [14, 22].

The delivery yield of injection in zebrafish embryos yolk and microinjection in single HeLa cells was good, as well as the cell viability. These methods appeared the most gentle for delivering GNRs in cells. However, each of them has a downside: in the case of injection in yolk the imaging cannot be performed till few hours after the delivery, while in case of single cell microinjection there is a limited throughput. An advantage of microinjection in single cell is the possibility to selectively deliver in the cytoplasm or in the nucleus.

When the delivery was successful, we localized GNRs inside cells and analyzed their trajectories to obtain mobility information. We recorded GNRs traces ranging from few seconds to 7 minutes long, even though the typical duration of our movies was of about 10 minutes. Most of the traces we obtained were shorter than 1 minute. It was not clear why GNRs disappeared (or appeared) during the movie. It is possible that the index of refraction around a GNR changed, due to non-specific interaction with molecules or to the diffusion inside an area with different characteristics. A change in the dielectric constant induces a shift in the plasmon resonance peak of the GNR (as explained in Chapter 1, Section 1.3.2). As a result, the GNR cannot be excited anymore at the same wavelength. A similar 'blinking' behavior of gold nanoparticles in cell was already observed, but not investigated in detail [19]. Alternatively, reshaping of GNRs could occur, inducing a blue-shift in the spectrum. The excitation intensity range we used (typically around 0.1 kW/cm^2) is several orders of magnitude lower than threshold for complete GNR melting *in vitro* [23]. However, it could be sufficiently high to start the reshaping proces of the nanorods. Several studies about GNRs reshaping have been reported, both in solution [24, 25] and at single nanorod level [26], that revealed a strong dependence of the reshaping threshold on the size and aspect ratio of the particles and on the excitation pulse width. In addition, the medium and the presence of a PEG layer around the GNRs can also influence the reshaping threshold, by changing the ther-

mal conductivity [27]. For future experiments it should be investigated whether GNRs reshaping occurs in the excitation energy range we use, also taking into consideration the non-linear nature of the two-photon process.

Due to the short trace length and consequently the large error on MSD points, we could not characterize the mobility of individual traces with sufficient detail to identify different modes of mobility. We instead distinguished different mobility characteristics from the ensemble MSD histograms, and then fitted the traces belonging to each population accordingly.

In microinjected and electroporated HeLa cells we found a fraction of immobile GNRs equal to about 15% of the total number of traces. In zebrafish embryos cells this fraction is larger (30%), whereas it is almost absent in squeezed cells (1%). These immobile GNRs could be attached to immobile structures in the cell, such as stuck vesicles. Squeezed cells showed very poor viability, and it may be that most of the cellular structures were destroyed, explaining the extremely low percentage of stuck GNRs. The fraction of immobile GNRs was twice as large in zebrafish embryos cells. The difference in the cellular structure between zebrafish embryos cells and mammalian cells could explain the difference in the immobile fraction. The immobility of GNRs cannot be explained by the presence of large GNR clusters that would diffuse slower: from the distribution of the GNRs intensities, we estimated a percentage of clusters of only about 3% (Fig. S1).

Two populations of mobile GNRs were found: a freely diffusing one and one diffusing within a confined space. The diffusing population was 42% of the total in the nucleus of microinjected HeLa cells, 49% in the cytoplasm, 57% in electroporated cells and 76% in squeezed cells. In zebrafish embryos cells all the mobile rods (71%) were freely diffusing. Note that the size of the diffusing fraction is calculated based on a manually set threshold, and therefore it must be interpreted as indicative. All the GNRs in zebrafish embryos cells were freely diffusing.

The expected diffusion coefficient of GNRs inside cells can be calculated from the size of the particles and the viscosity of the environment (Eq. 2.4 in Chapter 2). GNRs are covered with a layer of PEG that increases their size: we calculated the hydrodynamic radius of PEG using fluorescence correlation spectroscopy (FCS) measurements (see Chapter

2, S1). The hydrodynamic radius of the GNRs is approximately 24 nm, though variations can occur due to the size variability within the GNRs sample. The value of intracellular viscosity is more difficult to quantify: it was reported to be similar [28, 29] to up to 3.2 times higher than the viscosity of water [30]. A recent review on the chemistry of the cytoplasm [31] however, concludes that it is inaccurate to consider the cytoplasm as a homogeneous solution with a single viscosity value: areas with different viscosities are present, due to phase-separation phenomena induced by crowding. The viscosity inside the nucleus was reported to be the same as in the cytoplasm, as the two compartments are communicating [32]. Assuming an intracellular viscosity between 1 and 4 times the viscosity of water yields a diffusion coefficient between 2 and 10 $\mu\text{m}^2/\text{s}$, about three to four orders of magnitudes higher than the values we obtained, around 0.006 $\mu\text{m}^2/\text{s}$ in all cases. Our results are compatible with the diffusion coefficients obtained previously in our group [10]. To explain such low values, we hypothesized at the time that GNRs were internalized into vesicles, in agreement with other authors that claim that nanoparticles can hardly escape internalization into vesicles [1]. This was also the motivation to explore alternative delivery methods that do not depend on endocytosis. However, the diffusion coefficients that we obtained here are surprisingly similar both in the cytoplasm and in the nucleus. As a vesicles system is not present in the nucleus, this claim cannot hold. The GNRs diffusion could be slowed down by the high crowding present in the nucleus, resulting in a value similar to the diffusion of vesicles in the cytoplasm. Another hypothesis is that the calculation of the diffusion coefficient should consider the presence of obstacles and temporary stickiness of the GNRs, which would effectively slow down the GNRs. However this would require detailed knowledge of the precise structure in each cell.

In HeLa and COS1 cells we found a population of GNRs with a MSD independent of the time lag, compatible for example with the enclosure by structural elements within the cellular environment. From the MSD analysis of this GNR population we obtained a wide range of confinement radii, from about 100 nm to 1 μm . These values are compatible with the range of sizes of compartments in cells: from vesicles of few hundreds of nm [33], to accessible spaces in the nucleus or between the plasma membrane and the nuclear membrane. Some outliers are present in the distribution (less than 10%), going from 1 μm up to 10 μm . As our

traces are too short for the GNRs to be able to encounter such large confinements, we therefore hypothesize that these confinement radii are the result of the large stochastic variations of the MSD for short traces. On the other hand, some freely diffusing GNRs can have a MSD lower than the threshold we set for confined particles, but they cannot be distinguished a priori.

The absence of a confined population in zebrafish cells can be due to a lower density of cellular structures as compared to mammalian cells. This could also suggest that injection in yolk is an effective way to escape the GNRs internalization into organelles.

Overall, we found a large similarity in the mobility of GNRs in HeLa and COS1 cells with a relatively large fraction of confined GNRs. The diffusion coefficient of GNRs in zebrafish embryos cells was a bit lower than in HeLa and COS1 cells, yet in the same order of magnitude. The values we obtained are lower than the D expected for particles of the same size moving inside cells, but the calculation of the expected D does not take into account stickiness, obstacles nor variations in viscosity.

The precision of our analysis could be improved by acquiring longer GNRs trajectories that would reduce the error on the MSD points. In this way, a reliable attribution to a mobility model could be carried out for every single trajectory, making possible also to distinguish superdiffusive from diffusive traces. Including an analysis of the direction of the movement [34], which also becomes more reliable for longer traces, can further help to quantify the deviation from purely diffusive motion. Longer traces can be achieved by increasing the frame rate of the microscope, or by extending the duration of the GNR signal. More investigation must be carried on the apparent blinking/bleaching behavior of GNRs that we observe in cell.

As next step, we will verify the functionalization of GNRs in order to target specific structures or proteins in the cell. High precision and long-time single-particle tracking of GNRs has a great potential for the study cellular processes in live cells.

3.5 Supplementary figures

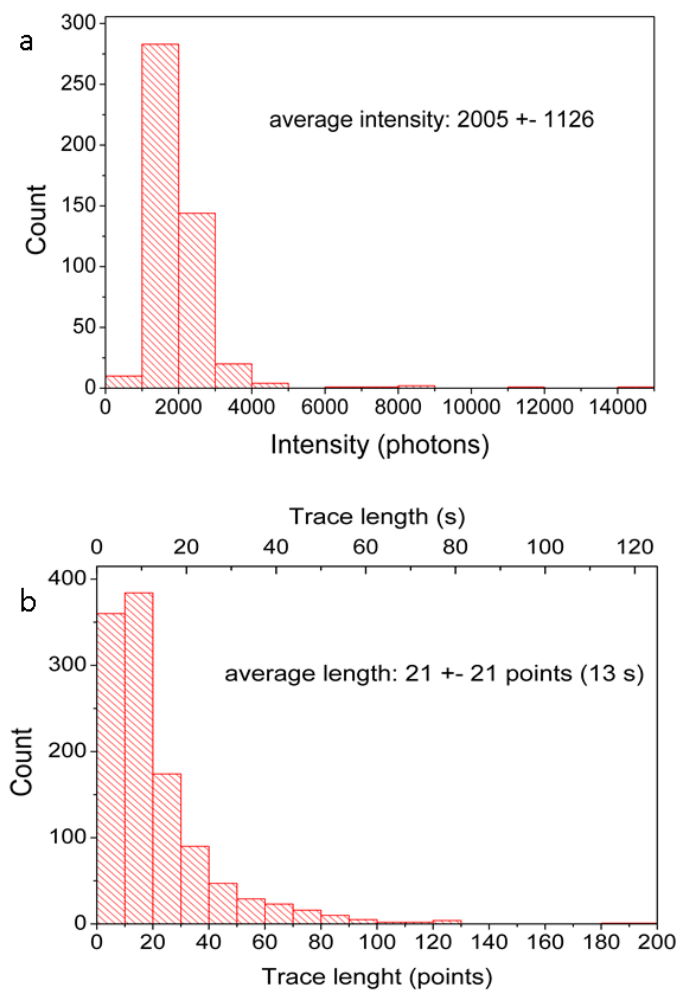
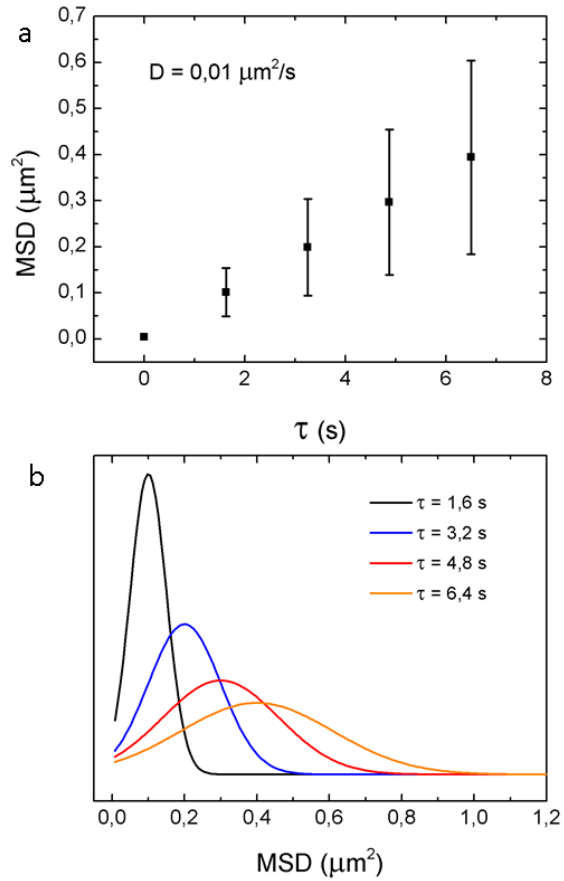


Figure S1

Distribution of a) intensities and b) trace lengths of GNRs microinjected in cytoplasm of HeLa cells.

**Figure S2**

Simulated MSD of a particle moving with $D = 0,01 \mu\text{m}^2/\text{s}$ in a trace of 20 points. a) MSD plot vs time step τ . b) Simulation of the distributions of the MSD populations at each time step τ .

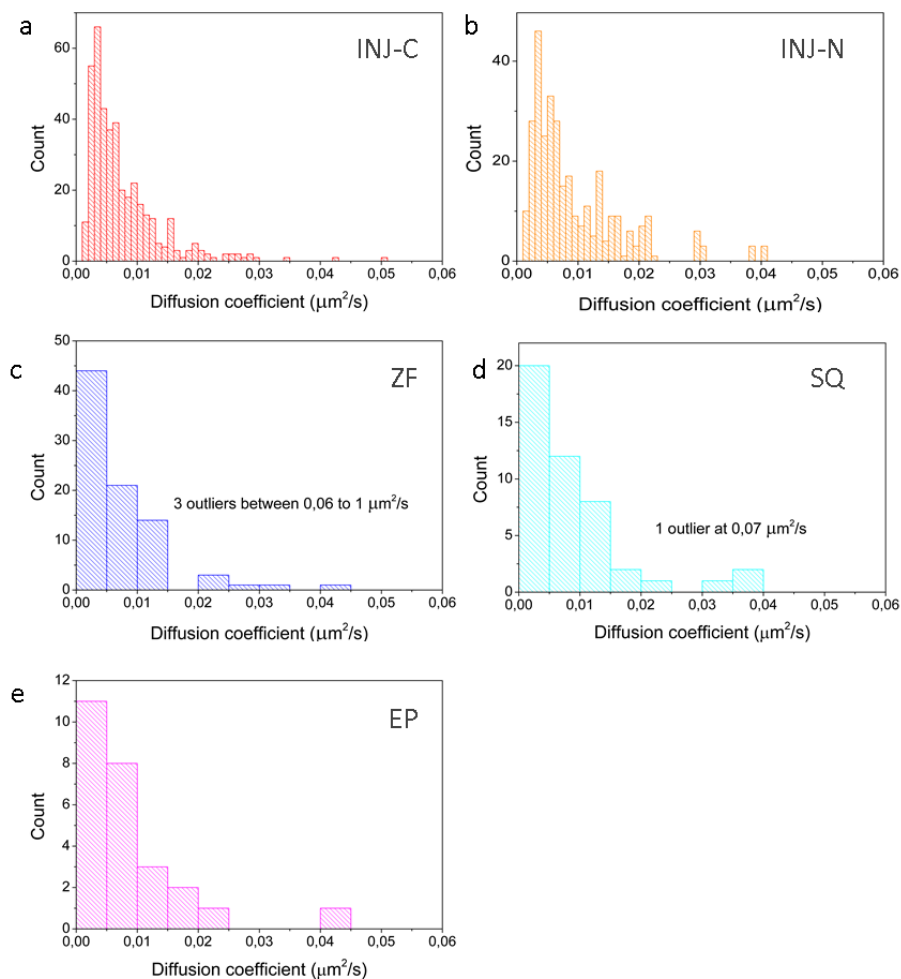
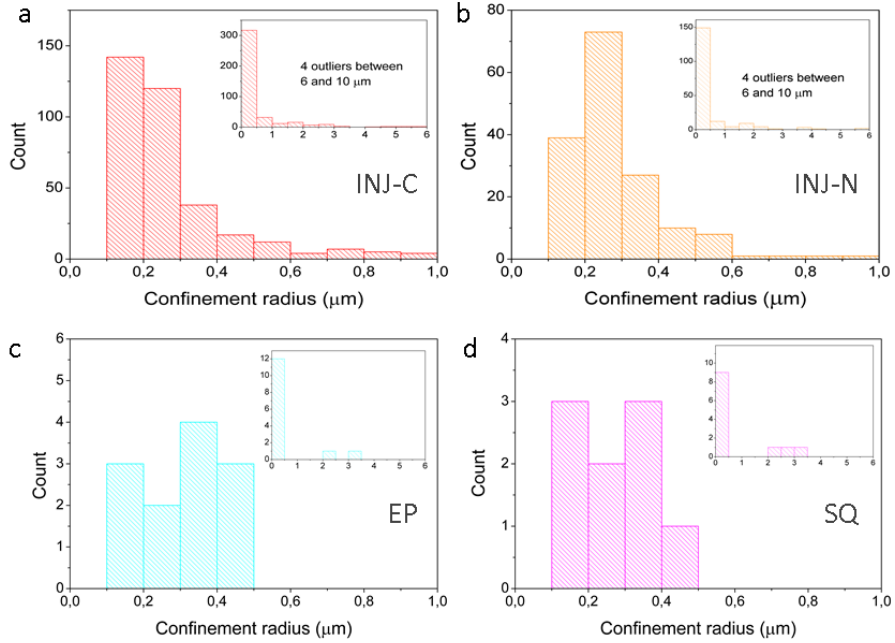


Figure S3

Histograms of distributions of the diffusion coefficients for GNRs microinjected in a) cytoplasm and b) nucleus of HeLa cells, c) injected in the yolk of zebrafish embryos cells, d) delivered in squeezed cells and e) in electroporated cells. The bin size is changed between experiments depending on the sample size: 0,001 in a,b and 0,005 in c,d,e.

**Figure S4**

Histograms of distributions of the confinement radii for GNRs a) microinjected in the cytoplasm or b) microinjected in the nucleus of HeLa cells, c) in squeezed cells or d) in electroporated cells, in the range between 0 and 1 μm . Insets show zoom-outs of the histograms.

BIBLIOGRAPHY

- [1] Raphaël Lévy et al. “Gold nanoparticles delivery in mammalian live cells: a critical review.” In: *Nano reviews* 1 (Jan. 2010). ISSN: 2000-5121.
- [2] Wei Qian et al. “Dark-field light scattering imaging of living cancer cell component from birth through division using bioconjugated gold nanopores”. In: *Journal of Biomedical Optics* 15.4 (2010), p. 046025. ISSN: 10833668.
- [3] Paola Nativo, Ian Prior, and Mathias Brust. “Uptake and intracellular fate of surface-modified gold nanoparticles.” In: *ACS nano* 2.8 (Aug. 2008), pp. 1639–44. ISSN: 1936-086X.
- [4] Cécile Leduc et al. “Single-molecule imaging in live cell using gold nanoparticles.” In: *Methods in cell biology* 125 (Jan. 2015), pp. 13–27. ISSN: 0091-679X.
- [5] Nardine S. Abadeer and Catherine J. Murphy. “Recent Progress in Cancer Thermal Therapy Using Gold Nanoparticles”. In: *The Journal of Physical Chemistry C* 120.9 (Mar. 2016), pp. 4691–4716. ISSN: 1932-7447.
- [6] Hong Ding et al. “Gold Nanorods Coated with Multilayer Polyelectrolyte as Contrast Agents for Multimodal Imaging”. In: *The Journal of Physical Chemistry C* 111.34 (Aug. 2007), pp. 12552–12557. ISSN: 1932-7447.
- [7] Adegboyega K. Oyelere et al. “Peptide-conjugated gold nanorods for nuclear targeting.” In: *Bioconjugate chemistry* 18.5 (2006), pp. 1490–7. ISSN: 1043-1802.
- [8] Xiaohua Huang et al. “Cancer cell imaging and photothermal therapy in the near-infrared region by using gold nanorods.” In: *Journal of the American Chemical Society* 128.6 (Feb. 2006), pp. 2115–20. ISSN: 0002-7863.

- [9] Nicholas J Durr et al. “Two-photon luminescence imaging of cancer cells using molecularly targeted gold nanorods.” In: *Nano letters* 7.4 (Apr. 2007), pp. 941–5. ISSN: 1530-6984.
- [10] Bram van den Broek et al. “Parallel nanometric 3D tracking of intracellular gold nanorods using multifocal two-photon microscopy.” In: *Nano letters* 13.3 (Mar. 2013), pp. 980–6. ISSN: 1530-6992.
- [11] Peter Sandin et al. “High-Speed Imaging of Rab Family Small GT-Pases Reveals Rare Events in Nanoparticle Trafficking in Living Cells”. In: *ACS Nano* 6.2 (Feb. 2012), pp. 1513–1521. ISSN: 1936-0851.
- [12] Babak Nikoobakht and Mostafa A. El-Sayed. “Preparation and Growth Mechanism of Gold Nanorods (NRs) Using Seed-Mediated Growth Method”. In: *Chemistry of Materials* 15.10 (May 2003), pp. 1957–1962. ISSN: 0897-4756.
- [13] Nicolas Bogliotti et al. “Optimizing the formation of biocompatible gold nanorods for cancer research: Functionalization, stabilization and purification”. In: *Journal of Colloid and Interface Science* 357.1 (2011), pp. 75–81. ISSN: 00219797.
- [14] Armon Sharei et al. “A vector-free microfluidic platform for intracellular delivery.” In: *Proceedings of the National Academy of Sciences of the United States of America* 110.6 (Feb. 2013), pp. 2082–7. ISSN: 1091-6490.
- [15] Jonathan N Rosen, Michael F Sweeney, and John D Mably. “Microinjection of zebrafish embryos to analyze gene function.” In: *Journal of visualized experiments : JoVE* 25 (Mar. 2009). ISSN: 1940-087X.
- [16] Xavier Michalet. “Mean square displacement analysis of single-particle trajectories with localization error: Brownian motion in an isotropic medium.” In: *Physical review. E, Statistical, nonlinear, and soft matter physics* 82.4 Pt 1 (Oct. 2010), p. 041914. ISSN: 1550-2376.
- [17] Thomas Bickel. “A note on confined diffusion”. In: *Physica A: Statistical Mechanics and its Applications* 377.1 (2007), pp. 24–32. ISSN: 03784371.

-
- [18] H Qian, M P Sheetz, and E L Elson. “Single particle tracking. Analysis of diffusion and flow in two-dimensional systems.” In: *Biophysical journal* 60.4 (Oct. 1991), pp. 910–21. ISSN: 0006-3495.
- [19] Felipe Moser et al. “Cellular Uptake of Gold Nanoparticles and Their Behavior as Labels for Localization Microscopy.” In: *Biophysical journal* 110.4 (Feb. 2016), pp. 947–53. ISSN: 1542-0086.
- [20] Yingbo Zu et al. “Gold nanoparticles enhanced electroporation for mammalian cell transfection.” In: *Journal of biomedical nanotechnology* 10.6 (June 2014), pp. 982–92. ISSN: 1550-7033.
- [21] Juqiang Lin et al. “Rapid delivery of silver nanoparticles into living cells by electroporation for surface-enhanced Raman spectroscopy”. In: *Biosensors and Bioelectronics* 25.2 (2009), pp. 388–394. ISSN: 09565663.
- [22] Gregory Lee Szeto et al. “Microfluidic squeezing for intracellular antigen loading in polyclonal B-cells as cellular vaccines”. In: *Scientific Reports* 5 (May 2015), p. 10276. ISSN: 2045-2322.
- [23] S. Link et al. “Laser-Induced Shape Changes of Colloidal Gold Nanorods Using Femtosecond and Nanosecond Laser Pulses”. In: *The Journal of Physical Chemistry B* 104.26 (July 2000), pp. 6152–6163. ISSN: 1520-6106.
- [24] Stephan Link, Zhong L. Wang, and Mostafa A. El-Sayed. “How Does a Gold Nanorod Melt?” In: *The Journal of Physical Chemistry B* 104.33 (Aug. 2000), pp. 7867–7870. ISSN: 1520-6106.
- [25] Marta Gordel et al. “Post-synthesis reshaping of gold nanorods using a femtosecond laser.” en. In: *Physical chemistry chemical physics : PCCP* 16.1 (Jan. 2014), pp. 71–8. ISSN: 1463-9084.
- [26] Peter Zijlstra, James W. M. Chon, and Min Gu. “White light scattering spectroscopy and electron microscopy of laser induced melting in single gold nanorods”. In: *Physical Chemistry Chemical Physics* 11.28 (2009), p. 5915. ISSN: 1463-9076.
- [27] Yukichi Horiguchi et al. “Photothermal Reshaping of Gold Nanorods Depends on the Passivating Layers of the Nanorod Surfaces”. In: *Langmuir* 24.20 (Oct. 2008), pp. 12026–12031. ISSN: 0743-7463.

- [28] E. O. Puchkov. “Intracellular viscosity: Methods of measurement and role in metabolism”. en. In: *Biochemistry (Moscow) Supplement Series A: Membrane and Cell Biology* 7.4 (Dec. 2013), pp. 270–279. ISSN: 1990-7478.
- [29] K. Fushimi. “Low viscosity in the aqueous domain of cell cytoplasm measured by picosecond polarization microfluorimetry”. In: *The Journal of Cell Biology* 112.4 (Feb. 1991), pp. 719–725. ISSN: 0021-9525.
- [30] R Swaminathan, C P Hoang, and A S Verkman. “Photobleaching recovery and anisotropy decay of green fluorescent protein GFP-S65T in solution and cells: cytoplasmic viscosity probed by green fluorescent protein translational and rotational diffusion.” In: *Biophysical journal* 72.4 (Apr. 1997), pp. 1900–7. ISSN: 0006-3495.
- [31] Kate Luby-Phelps. “The physical chemistry of cytoplasm and its influence on cell function: an update.” In: *Molecular biology of the cell* 24.17 (Sept. 2013), pp. 2593–6. ISSN: 1939-4586.
- [32] Katherine Luby-Phelps. *Microcompartmentation and Phase Separation in Cytoplasm*. Vol. 192. International Review of Cytology. Elsevier, 1999, pp. 189–221. ISBN: 9780123645968.
- [33] Qian Peter Su et al. “Vesicle Size Regulates Nanotube Formation in the Cell.” en. In: *Scientific reports* 6 (Apr. 2016), p. 24002. ISSN: 2045-2322.
- [34] A Dupont et al. “Three-dimensional single-particle tracking in live cells: news from the third dimension”. In: *New Journal of Physics* 15.7 (July 2013), p. 075008. ISSN: 1367-2630.

CHAPTER 4

FUNCTIONALIZATION AND NUCLEAR TARGETING OF SINGLE GOLD NANORODS IN LIVE CELLS

Functionalization of gold nanorods is a necessary step for targeted delivery and for their use as labels to follow specific molecules in cells. Here, we functionalized gold nanorods with nuclear localization signal peptides and delivered them in live HeLa cells by single-cell microinjection. We used a two-photon multifocal scanning microscope to acquire 3D images of gold nanorods in cells. The efficiency of single-cell microinjection showed some variability between experiments and influenced the nuclear targeting results. Nevertheless, we observed nuclear localization of gold nanorods only when functionalized with the peptide. The nuclear targeting efficiency was around 15%, probably limited by the size of the particles. We noticed clearance of gold nanorods from the cytoplasm over time, both functionalized and not functionalized. The mobility of the nanorods did not depend on their functionalization. Overall, these experiments show that functionalization of gold nanorods with nuclear localization signal can be used for nuclear targeting, but only with a small yield.

Single-Particle Tracking of Gold Nanorods in Live Cells, S. Carozza, V. Keizer, A. Boyle, A. Kros, M. Schaaf, J. van Noort. (in preparation partially based on this chapter).

4.1 Introduction

Gold nanorods (GNRs) have a high potential as labels for single-molecule imaging in live cells, thanks to their brightness, stability and excitation with low energy radiation that minimizes autofluorescence and photo-damage in the cells. For such an application, they can be functionalized to bind to specific proteins, organelles or cells.

Next to single-particle imaging, GNRs have been used to selectively kill cancer cells, through gene-therapy [1] or photothermal therapy, due to their capability to enhance electromagnetic fields and generate heat upon irradiation with nearIR light [2]. Applications in cancer therapy usually target nanoparticles to the nucleus, where the therapeutic effect is maximum [2]. Though nuclear targeting has been well established for these practices, its mechanism has, to the best of our knowledge, not been studied at the single particle level, which will bring insights in the efficiency of delivery and is a prerequisite for single-particle tracking applications of GNRs.

In this study, we tested the functionalization of GNRs with a nuclear localization signal (NLS), a peptide that signals transport of molecules from the cytoplasm to the nucleus [3]. Nuclear localization of GNRs is the evidence of a successful functionalization with NLS and subsequent integration in the cellular transport pathway. The efficiency of nuclear delivery depends on the size of the nanoparticles. Due to the complex structure of the nuclear pores, small particles can diffuse passively through the membrane, but an active transport mechanism is necessary for larger particles [4]. Literature reports passive diffusion to the nucleus for particles with a size up to 10 nm [4, 5].

Active transport in the nucleus is typically achieved through conjugation with nuclear localization peptides [6], but other conjugations can also be used [7]. Successful nuclear targeting of particles with sizes up to 40 nm, functionalized with NLS, has been reported in several studies [8–13].

The GNRs we use for our experiments are approximately 53 nm x 20 nm. Previously, we observed no passive translocation of 40 nm x 10 nm GNRs in the nucleus without NLS functionalization (see Chapter 3). In the current study, we quantified the uptake of NLS-GNRs in the nucleus of live HeLa cells over time, as compared to GNRs without NLS sequence. Although there are many recent reports on the use of nanoparticles in cells, few quantify their uptake over time. To be able

to enter the nucleus when equipped with NLS, GNRs must be free to diffuse in cell and not trapped inside vesicles. We delivered GNRs in cells through single-cell microinjection, to avoid the uptake into vesicles which is common to passive delivery methods such as incubation. In addition, we characterized the reproducibility of the injection method. To localize GNRs in cells we used images acquired with a two-photon multifocal scanning microscope [14]. This setup acquires 3D movies of cells which can subsequently be processed to yield GNR localization with nm accuracy. We studied the mobility of GNRs functionalized with NLS and control GNRs in the cytoplasm, and compared the results with the ones obtained previously with non-functionalized GNRs.

4.2 Materials and methods

NLS synthesis

The NLS peptide was synthesized with a peptide synthesizer (Liberty 1, CEM), on a Rink-amide resin using HCTU (1H-Benzotriazolium 1-[bis(dimethylamino)methylene] -5chloro-,hexafluorophosphate (1-), 3-oxide) as a coupling agent and DIPEA (Diisopropylethylamine) as base. After synthesis, the peptide was acetylated at the N-terminus using a solution of acetic anhydride (5%) and pyridine (6%) in DMF (Dimethylformamide). After one hour, the peptide was cleaved using a solution of 95% trifluoroacetic acid (TFA), 2.5% water and 2.5% triisopropylsilane (TIPS). After one hour, the peptide was precipitated into ice-cold diethyl-ether, the precipitate collected by centrifugation, redissolved in water and freeze-dried to obtain a powder. The peptide was then purified by reverse-phase HPLC (high-performance liquid chromatography) over 30 minutes.

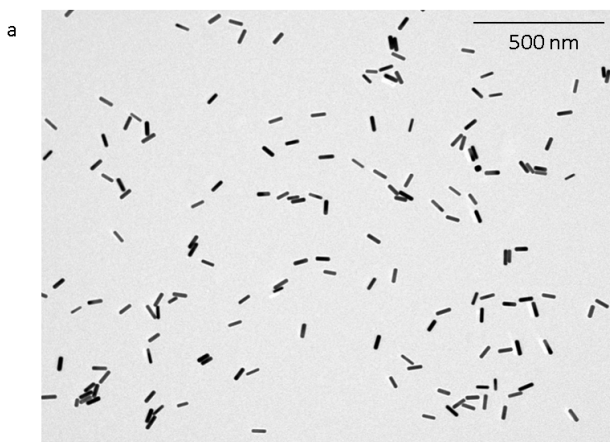
GNR preparation and functionalization

GNRs were produced by seed-mediated synthesis, as described in [15]. GNRs were then PEGylated, by addition to the solution of Polyethylene-Glycol 5000 in excess, to reduce toxicity of the particles [16]. PEG-GNRs were then functionalized with a sulfo-SMCC molecule, used as a cross-linker to the NLS. Conjugation with sulfo-SMCC was obtained by addition of 0.1 mg sulfo-SMCC solution to 5 ml 0.1 nM of PEG-GNR solution. The procedure was optimized to cover the entire surface of

the PEG-GNR with sulfo-SMCC. The solution was then left to stir for 30 minutes, centrifuged and the supernatant sulfo-SMCC was removed before resuspension of the solution in Phosphate-Buffered Saline (PBS).

For conjugation of NLS to GNRs, 1 ml of solution containing 1 mg of the NLS peptide was added to 4 ml of sulfo-SMCC-GNRs dissolved in PBS. The solution was then left to stir for 1 hour, centrifuged, the supernatant was removed and the solution resuspended in PBS. The NLS used here consists of the following amino acid sequence: GPKKKRKVGGC. An excess of NLS was used to assure the maximum coverage of the entire surface of the sulfo-SMCC-GNR. GNR Functionalization with sulfo-SMCC and NLS was performed on the day of the experiment.

Figure 4.1a shows a Transmission Electron Microscope (TEM, JEOL JEM 1010) image of a sample of GNRs. The size of the GNRs is about $53 (\pm 6) \times 20 (\pm 5)$ nm. GNRs were covered with a PEG layer, not visible in the TEM image. The size of PEG was previously estimated to be about 8 nm (Chapter 2, Supplementary Figure S1). A schematic depiction of the GNR functionalization is shown in Fig. 4.1b-d. PEG-GNRs functionalized with sulfo-SMCC but not with NLS were used as control. The successful functionalization of the GNRs with NLS was confirmed by the UV-Vis spectrum of the GNRs (Suppl. Fig. S1a). To show that the NLS was functional in HeLa cells, we injected NLS-carboxyl-fluorescein in HeLa cells and observed translocation to the nucleus, which did not occur injecting the dye only (Suppl. Fig. S1b, c).



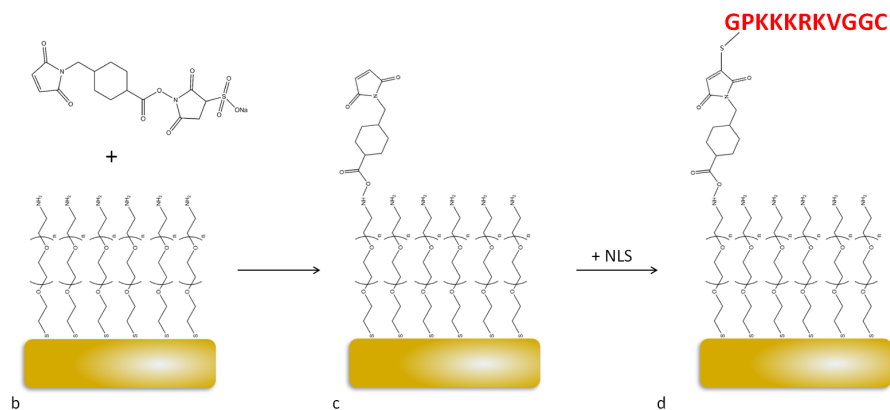


Figure 4.1

GNRs functionalization. a) TEM image of GNRs. b) PEG-GNR and a sulfo-SMCC molecule. c) A PEG-GNR functionalized with sulfo-SMCC-GNR. d) Functionalization of the PEG-GNR-sulfo-SMCC with NLS. The schemes are not in scale.

Cell culture and single-cell microinjection

On the day prior to injection, HeLa cells were plated in Dulbecco's modified eagle's medium (DMEM, Gibco) containing fetal calf serum (FCS) and kept at at 37 °C and 5% CO₂. Cells were incubated with Hoechst (3442, Thermofisher) for 20 minutes for nuclear staining, and subsequently washed 3 times and kept in DMEM. The injection was carried out as described in Chapter 3, Section 3.2.

Imaging

For confocal imaging, cells were imaged 20 minutes after injection on a Leica SPE microscope using a 63x objective (Leica) and a 488 nm laser.

A home-made two-photon multifocal scanning microscope [14] was used for two-photon imaging. The excitation beam, generated with a pulsed IR laser (Chameleon Ultra, Coherent), was split into an array of 25x25 focal spots by a diffractive optical element (custom-made by Holoeye Photonics). The array of beams was then scanned by a scanning mirror (FSM-300, Newport). A square wide-field illumination was thus obtained, covering an area in the sample of approximately 60 μm x 60

μm . A piezo-actuator (P-726 Pifoc, PI) was used to move the objective (60x APOTIRF, Nikon) in the z direction to acquire frames at different z positions. A LED light was used to obtain transmission images of the cells. More details on the setup can be found in Chapter 1, Section 1.2.3.

We acquired 3D movies of GNRs in cells, alternating 3D stacks of fluorescent images with transmission images of the cells. A fluorescent stack was made of typically 15 to 20 2D frames, spaced $0.5 \mu\text{m}$ between each other. The acquisition rate was 8 frames/s. Fluorescent images were acquired with a wavelength of 770 nm, exciting both GNRs and Hoechst. When the Hoechst intensity was too high to clearly distinguish GNRs, a long-pass filter at 515 nm was used to partially filter the dye.

Localization of GNRs inside cells

We distinguished the GNRs in the cytoplasm, in the nucleus and in the nuclear membrane using the 3D images of each cell. The peaks not overlapping with the Hoechst staining were counted as residing in the cytoplasm. GNRs on the edges of the Hoechst staining were counted as membrane-bound, while GNRs inside the regions labeled by Hoechst staining were counted as localized in the nucleus. It was not possible to distinguish between GNRs on the external or internal side of the nuclear membrane.

Mobility analysis

In every 3D stack of images the position of individual peaks was obtained by fitting with a 3D Gaussian function. The coordinates of GNRs in different 3D stacks were connected to obtain time trajectories. Traces shorter than 4 frames (about 8 seconds) were excluded from the analysis. In each movie we defined the regions corresponding to cell nuclei using the Hoechst staining. We analyzed the mobility of GNRs in the cytoplasm, both for NLS-GNRs and sulfo-SMCC-GNRs. We did not analyze the mobility of GNRs in the nucleus and nuclear membrane due to the difficulty to automatically distinguish between these populations. In few cases, GNRs were present outside the cells: we did not consider these in the analysis.

To analyze the mobility of the particles, we calculated the mean squared displacement (MSD), as described in Chapter 2 and 3. The MSD of a trajectory for a time step τ is the average of the squared

displacements covered by the particle in all steps with a delay of τ . In the case of a freely diffusing particle, the MSD exhibits a linear dependence on τ , that defines the diffusion coefficient D of the particle:

$$MSD(\tau) = 6\sigma^2 + 6D\tau \quad (4.1)$$

From fitting the MSD we obtain the diffusion coefficient D . The localization accuracy σ was for every single GNR fixed to the value based on its photon emission, as described in Chapter 2.

To identify immobile GNRs we used a threshold based on the localization accuracy of the setup. Based on the typical photon emission of the GNRs we use for our experiments, the localization accuracy in 3D is approximately 40 nm. GNRs showing a MSD at any time point lower than 6 times the square of the localization accuracy ($0.0096 \mu\text{m}^2$) were considered immobile.

The presence of a confinement limiting the particle mobility results in a negative curvature in the MSD that depends on the confinement radius R (Chapter 3, Eq. 3.3). If an active component is present in the motion, a positive curvature will be introduced, that depends on the velocity of the particle (Chapter 3, Eq. 3.2). However, using the current measurement parameters, it was not possible to accurately obtain R or v from individual traces. The movies were acquired for typically 2 to 3 minutes, and GNRs traces were typically less than 10 points long. As anticipated in Chapters 2 and 3, the error on each MSD point is strongly influenced by the length of the trajectory. Therefore, it was not possible to distinguish a curvature in MSD plots from stochastic variations of a single trace and to reliably determine the mobility mode (free diffusion or confined diffusion) from the curvature. Instead, we analyzed the ensemble distribution of MSD values at each time step to distinguish populations with different mobility modes by thresholding the MSD at the largest τ . We then fitted the MSD plot of individual traces with the corresponding mode and quantified the mobility parameters. This approach is the same we used in Chapter 3. Unfortunately, it does not allow to distinguish active populations.

The MSD analysis of GNRs traces was performed in LabVIEW. To assess the significance of differences in results between GNRs from different samples we used a Single-Factor Analysis of Variance (ANOVA), with a p-value threshold of 0.05. For non-Gaussian distributions, a non-

parametric ANOVA (Kruskal-Wallis test) was used.

4.3 Results

4.3.1 Reproducibility of single-cell microinjection

We characterized the reproducibility of the injection yield, comparing experiments carried out under the same conditions. Within each experiment, we injected NLS-GNRs and sulfo-SMCC-GNRs (used as control) in separate cell samples coming from the same culture. NLS-GNRs and sulfo-SMCC-GNRs originated from the same GNR batch. The experiment was repeated at least 4 times. The number of injected GNRs per cell showed significant differences between NLS-GNRs and sulfo-SMCC-GNRs within a single experiment (Fig. 4.2a,b). In some cases the number of injected sulfo-SMCC-GNRs was significantly lower than the number of NLS-GNRs. Also the number of cells containing GNRs (positive cells) was larger in NLS experiments than in control experiments (Suppl. Fig. S2a,b). Interestingly, for NLS-GNRs, the number of positive cells appeared to increase after 1 hour, while for sulfo-SMCC-GNRs this number decreased. The variation of total number of GNRs per experiment is shown in Suppl. Fig. S2c,d. Some differences in the GNRs samples might be attributed to different properties of the GNR samples. The UV-Vis spectra of the solutions (Supplementary Fig. S2e,f) feature a red-shift of the sample used in the first experiment, compared to the sample used for the later experiments. In addition, the size of the GNRs increased from 53 ± 6 nm x 20 ± 5 nm to approximately 60 ± 6 nm x 23 ± 5 nm. Though, it is not straightforward to relate these properties to injection yield.

We checked whether the presence of more NLS-GNRs in the nucleus as compared to sulfo-SMCC-GNRs was due to the larger number of NLS-GNRs in cells. The correlation between the number of NLS-GNRs localized in the nucleus and the total number of NLS-GNRs per cell is plotted in Fig. 4.2c. The plots, split up per experiment, are in Supplementary Fig. S2 g-j. Experiment 1 shows the most successful translocation of NLS-GNRs in the nucleus and a clear correlation between the total number of NLS-GNRs in the cell and the number of NLS-GNRs in the nucleus, but nuclear localization is not always found in cells with the highest number of GNRs. The microinjection yield of the other experiments is much smaller, precluding a proper analysis due

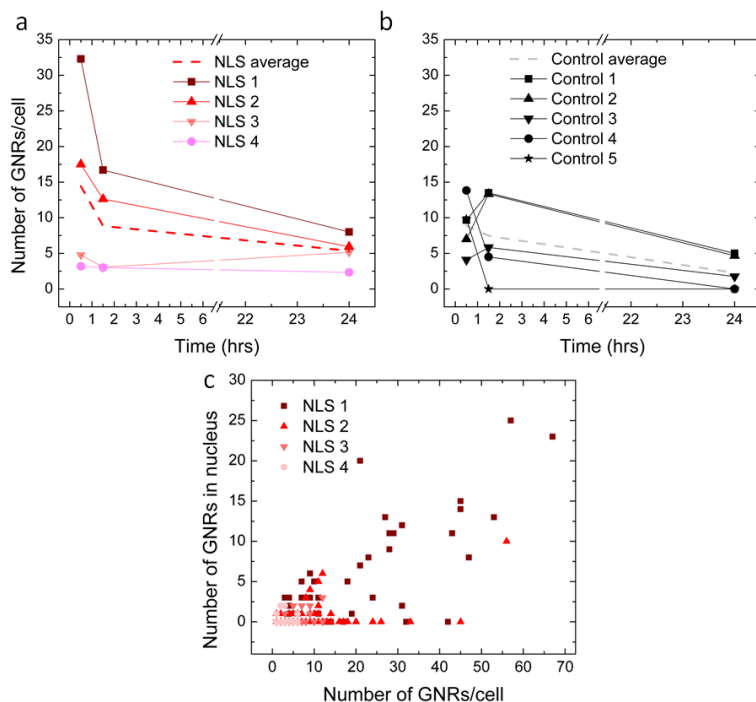


Figure 4.2

The injection efficiency varies between experiments. Variations in the number of GNRs injected per cell between different a) NLS experiments and b) control experiments. c) Number of NLS-GNRs found in the nucleus as a function of the total number of NLS-GNRs per cell among the 4 NLS experiments.

to the small number of GNRs. In the following, we either pooled all experiments or analyzed one experiment in detail, to recover details of the faith of GNRs in cells.

4.3.2 Localization of functionalized gold nanorods inside cells

Figure 4.3 shows some representative images of cells injected with NLS-GNRs (4.3a-c) and sulfo-SMCC-GNRs (4.3d-f). To localize GNRs in the nucleus or on the membrane, the 3D movie was used. We imaged the cells at three time points after injection: 0.5, 1.5 and 24 hours. The Hoechst staining indicates the cell nuclei, but gets weaker over time due to bleach-

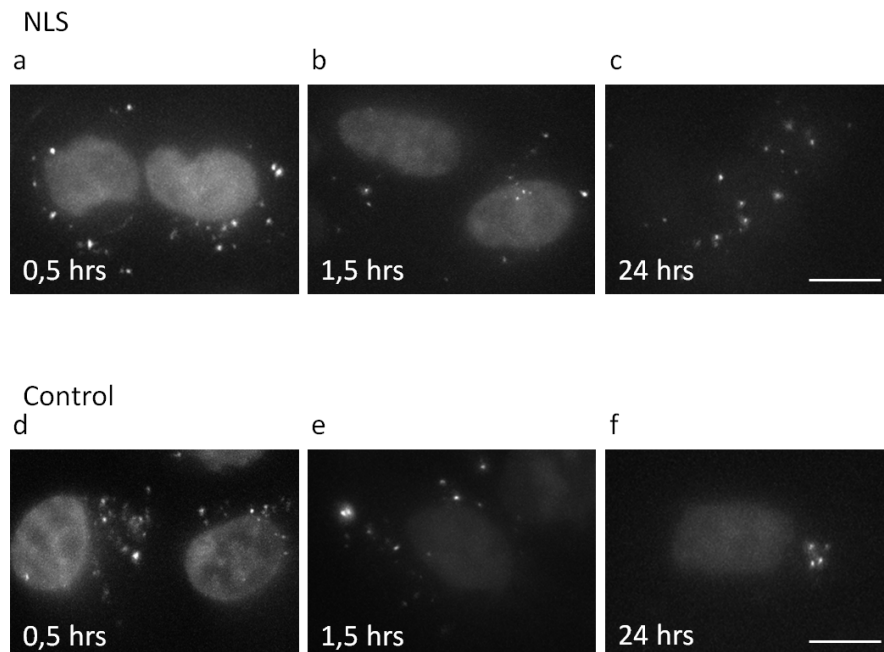


Figure 4.3

Two-photon images of HeLa cells injected with NLS-GNRs and sulfo-SMCC-GNRs, imaged at different time points after injection. a-c) Cells with NLS-GNRs, d-f) cells with Sulfo-SMCC-GNRs. Images at 0.5, 1.5 and 24 hours post injection are shown. Cell nuclei were stained with Hoechst. The scale bars correspond to 10 μm .

ing. NLS-GNRs were found in the cytoplasm, around the nuclear membrane and in the nucleus of cells. In contrast, sulfo-SMCC-GNRs were only found in the cytoplasm or around the nuclear membrane, with few exceptions. Even though not all cells showed healthy morphology after injection, injected cells with good viability, as judged by their shape, were found till up to 120 hours after injection in the case of NLS-GNRs (Supplementary Figure S3a) and up to 48 hours in the case of sulfo-SMCC-GNRs (Supplementary Figure S3b), well beyond the duration of our experiment.

We quantified the number of GNRs in the nucleus, nuclear membrane and cytoplasm of cells over time, pooling all experiments, and

compared the results for NLS-GNRs and sulfo-SMCC-GNRs, which was used as control. The results are shown in Figure 4.4. We found an average of 2 NLS-GNRs in the nucleus at all three time points (Figure 4.4a), though the variation in the number of nuclear NLS-GNRs was very large (up to about 30 GNRs in experiment 1). We only observed a few nuclear sulfo-SMCC-GNRs: the difference with the number of nuclear NLS-GNRs is statistically significant. Note that the 3D stack of images is necessary to distinguish GNRs in the nucleus or bound to the nuclear membrane: for this reason, some GNRs that seem to localize in the nucleus in a projected image (see example in Fig. 4.3d,e) are instead membrane-bound. Both NLS-GNRs and sulfo-SMCC-GNRs were found in or around the nuclear membrane (Figure 4.4b). An average of 5 NLS-GNRs and 3 sulfo-SMCC-GNRs were in the membrane at 0.5 hours post injection; both numbers decreased over time, but no significant difference was found between NLS-GNRs and sulfo-SMCC-GNRs in this compartment. In the cytoplasm, (Figure 4.4c) we counted an average of 7 NLS-GNRs and 5 sulfo-SMCC-GNRs at 0.5 hours post injection, both decreasing significantly over time. No significant difference was observed between NLS-GNRs and sulfo-SMCC-GNRs in the cytoplasm. The details of the distribution of GNRs in each compartment in time can be found in Supplementary Fig. S4a-c.

Overall, the percentage of GNRs translocating to the nucleus is about 15% when functionalized with NLS and less than 2% for sulfo-SMCC-GNRs (Fig. 4.4d). This result demonstrates successful targeting of GNRs in the nucleus, albeit with relatively low yield. Note that the percentage of nuclear NLS-GNRs at 24 hours after injection increases due to the loss of GNRs in the cytoplasm. The increase in percentage of sulfo-SMCC-GNRs in the membrane is due to the same reason.

4.3.3 Mobility of functionalized gold nanorods

We analyzed the mobility of NLS-GNRs and sulfo-SMCC-GNR in the cytoplasm of injected cells. Visual inspection of the MSD histograms suggests the presence of two populations both in NLS-GNRs and sulfo-SMCC-GNRs (Supplementary Figure S5). A population with MSD lower than $0.2 \mu\text{m}^2$ is stable in time, consistent with confined GNRs, while MSDs larger than $0.2 \mu\text{m}^2$ increase over time, typical for free diffusion. In addition to mobile GNRs, an immobile fraction was found with a constant MSD that does not exceed the positional accuracy. Though we

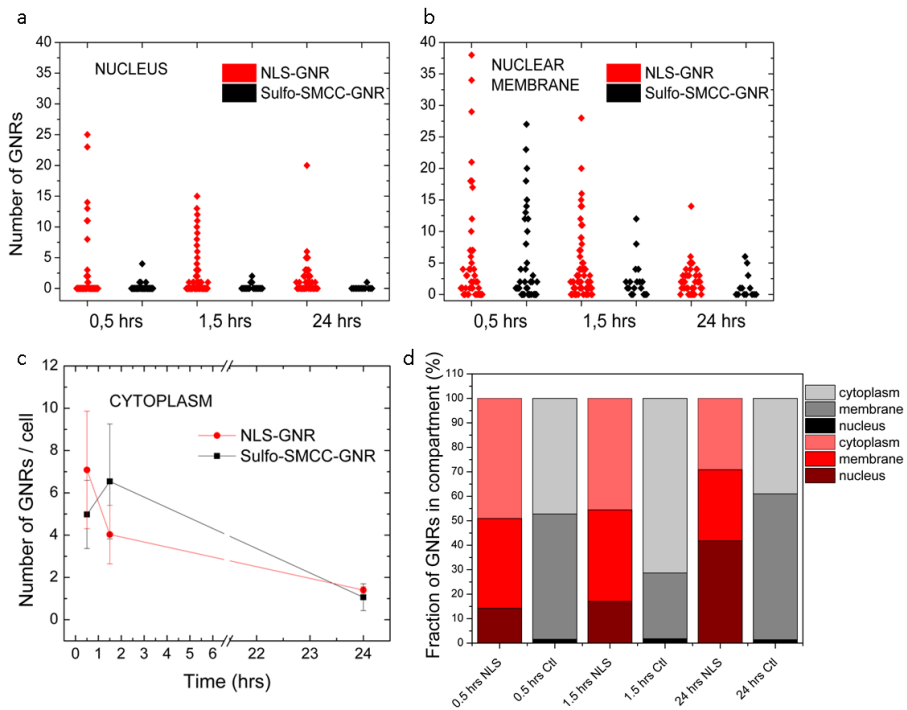


Figure 4.4

Difference in the distribution of NLS-GNRs and sulfo-SMCC-GNRs in cells over time. a) Number of GNRs in the nucleus over time, in NLS (red) and control experiment (black). b) Number of GNRs in the nuclear membrane over time. c) Number of GNRs in the cytoplasm over time. The numbers are the mean and standard deviation in 5 control and 4 NLS experiments. d) Bar plot of percentages of GNRs in each compartment over time, in NLS (NLS-GNRs) and control experiments (sulfo-SMCC-GNRs).

observed some variations, it appears that the MSD of the GNRs does not change with time after injection.

Next, we fitted the MSD of single traces to obtain the diffusion coefficients or the confinement sizes. For the traces that were assigned to be confined, we observed a constant MSD that exceeded the positional accuracy. This implies a D that is faster than can be resolved given the time resolution of our experiment. Therefore we only fitted the confinement sizes in these cases. Table 4.1 reports the mobility results. The number of immobile GNRs and the corresponding percentage of the total number of traces is shown for the immobile fraction. The number of traces in each population and the corresponding percentage, the median, 1st and 3rd quartiles of the diffusion coefficients and confinement sizes are reported for mobile GNRs. Note that all the distributions exhibited a longer tail of large values, thus they deviate from normal distributions (see histograms in Supplementary Fig. S6). The distributions of diffusion coefficients and confinement sizes are shown in the box plots in Fig. 4.5a,b. No significant difference was found among the parameters at different time points for both NLS-GNRs and sulfo-SMCC-GNRs (Supplementary Figure S7 and Supplementary Tables S2 and S3), so we pooled the results from all time points.

The percentages relative to each population are summarized in Fig. 4.5c. The detailed percentages relative to each time point are reported in Supplementary Fig. S8. The immobile population amounts to 17% in NLS-GNRs and 9% in sulfo-SMCC-GNRs. The confined population is about 46% of the total number of NLS-GNRs and 53% of the population of sulfo-SMCC-GNRs. The median of the confinement radius is 0.4 μm both in cells injected with NLS-GNRs and sulfo-SMCC-GNRs. The distribution of confinement radii is larger for NLS-GNRs (Fig. 4.5b), but the difference is not statistically significant. The freely diffusing population is 37% of the NLS-GNRs and 38% of the NLS-GNRs. The median of the diffusion coefficients is 0.005 $\mu\text{m}^2/\text{s}$ in both cases: this value is compatible with the diffusion coefficients of GNRs freely diffusing in cells we obtained previously (see Chapter 3, Section 3.3.2), as shown in Supplementary Fig. S9. Mobility values of PEG-GNR without functionalization, sulfo-SMCC-GNRs and NLS-GNRs do not show any significant difference (see Supplementary Table S4).

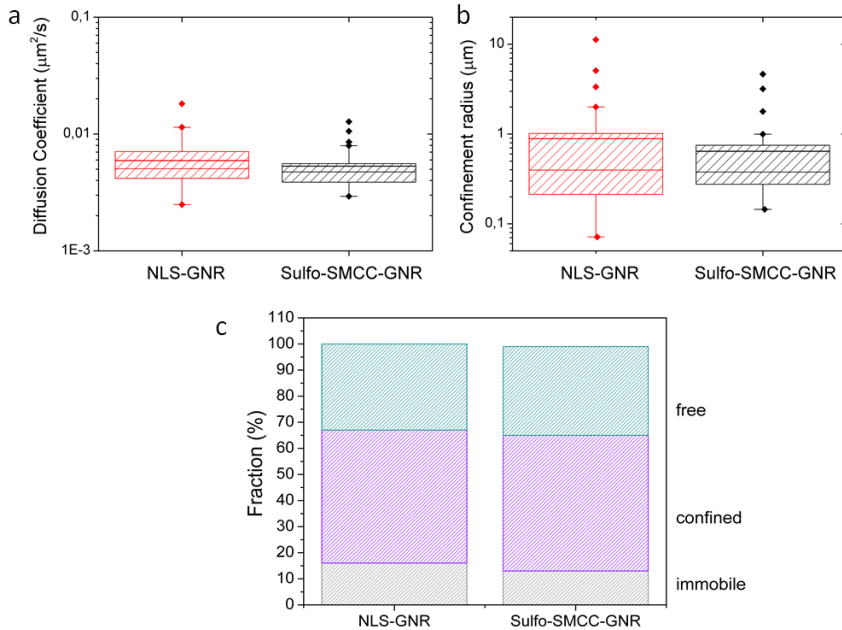


Figure 4.5

Mobility of NLS-GNRs and sulfo-SMCC-GNRs in the cytoplasm. a) Distribution of diffusion coefficients of freely diffusing NLS-GNRs and sulfo-SMCC-GNRs. b) Distribution of the confinement radii for the NLS-GNRs and sulfo-SMCC-GNRs with confined mobility. c) Percentages relative to each GNR population (immobile, freely diffusing and confined) for NLS-GNRs and sulfo-SMCC-GNRs.

4.4 Discussion and conclusion

We used single-cell microinjection to deliver gold nanorods in the cytoplasm of HeLa cells. We tested the fate of gold nanorods functionalized with nuclear localization signal peptides, that induce nuclear targeting. The results were compared with results obtained from gold nanorods not functionalized with the peptides. First, we characterized the reproducibility of the injection procedure, by analyzing differences in outcome between individual repeated experiments. We observed a large variability both in the number of positive cells and in the number of NLS-GNRs and sulfo-SMCC-GNRs injected in cells. We attributed the differences to the composition of the GNRs samples. For GNRs samples that exhibited

Population	Parameter	NLS-GNR	sulfo-SMCC-GNR
Immobile	Pop. Size	25; 17%	7; 9%
Confined	Pop. Size	66; 46%	39; 53%
	Confinement (μm)	0.4 (0.2-1)	0.4 (0.3-0.7)
Freely Diffusing	Pop. Size	53; 37%	28; 38%
	D ($\mu\text{m}^2/\text{s}$)	0.005 (0.004-0.007)	0.005 (0.004-0.006)

Table 4.1

Mobility parameters obtained for NLS-GNRs and sulfo-SMCC-GNRs. The table reports the number of traces corresponding to each population and the relative percentages. For the confined populations, the median, 1st and 3rd quartiles of the confinement sizes are reported. For the freely diffusing populations, the median, 1st and 3rd quartiles of the diffusion coefficients are reported.

a blue-shift, the excitation was less efficient at 770 nm wavelength, and might explain the reduced number of GNRs we see in later experiments. The blue-shift can be due to the growth of particles in the samples over time after synthesis, due to the presence of free gold in the growth solution that was not properly removed. TEM images of the samples used for the last experiments showed indeed an increased particle size.

The number of positive cells varied between the NLS and control experiments, but also within the same experiments over time. Cases of reduction in the number of positive cells over time can be due to cell death, while cases of increase of positive cells can be explained in two ways. Cells may release some GNRs, which could subsequently be taken up by other cells (as also hypothesized in [13]). Alternatively, we could have missed positive cells at some time point, due to the difficulty in finding the injected cells not in close proximity to the marker in the sample. For control experiments the low number of positive cells at 24 hours can result from a loss of sulfo-SMCC-GNRs in the cytoplasm. However, given the small number of cells, due to the relatively low throughput of the microinjection technique, and the large number of parameters that could affect injection efficiency and the fate of GNRs, it is at this point not possible to substantiate such scenarios.

Due to the difficulty in obtaining the same conditions in individual experiments, the results from different individual experiments exhibited some variations. Nevertheless, in all experiments we observed translocation of NLS-GNRs to the nucleus of HeLa cells. The translocation efficiency was variable between different experiments, yet generally low. Adding all individual experiments, the absolute number of NLS-GNRs localized in the nucleus is low (2 on average). In percentage, this corresponds to an efficiency of about 15%. This value is significantly different from the percentage of sulfo-SMCC-GNRs found in the nucleus, that is less than 2%. The large size of the GNRs (from approximately 53 nm x 20 nm to 60 nm x 23 nm, plus a PEG layer of about 8 nm) might explain the low efficiency of nuclear delivery. Some NLS-GNRs were found in the nuclear membrane: this could be due to the impossibility of entering the nucleus when the GNRs are too large. It is possible that only GNRs with a favorable orientation (perpendicular to the surface of the membrane) could enter the nuclear pores. However, there is no significant difference with the number of sulfo-SMCC-GNRs located around the membrane. We tested smaller GNRs but these proved a higher stickiness that affected severely the delivery efficiency by microinjection (data not shown).

Previously, successful nuclear targeting was reported for particles with sizes up to 40 nm [17], mostly using nanospheres [9, 11, 12]. Oyelere et al [8] reported successful nuclear translocation of GNRs functionalized with NLS and delivered in cells through incubation. However, these GNRs were smaller than the ones we used (about 40 nm x 15 nm) and not PEGylated (the PEG layer increases the final size of the particles of about 8 nm for each side). In addition, 2D images were used to assess the location of the GNRs, it was therefore hard to distinguish GNRs in the nucleus or bound to the nuclear membrane. The translocation into the nucleus of NLS-GNRs that we observed occurred within the first half an hour, in agreement with previous findings [17].

The number of GNRs in the cytoplasm showed no difference between NLS and control experiments, and in both cases this number decreased in time. As there was no significant change over time in the number of GNRs in the nucleus and in the nuclear membrane, the decreasing number of particles in the cytoplasm cannot be due to translocation to the other compartments. The loss of GNRs in the cytoplasm might be due to exocytosis. Exocytosis of particles localized in the cytoplasm was

observed previously [13, 18]. The impossibility for particles larger than 10 nm to cross the nuclear membrane in absence of a specialized localization signal (the NLS works only to signal towards the nucleus and not back [4]), explains the absence of exocytosis of nuclear GNRs. GNRs localized on the external surface of the nuclear membrane might be stuck, therefore they cannot be excreted.

We analyzed the mobility of the GNRs in the cytoplasm of the injected cells. We found an immobile population, equal to 17% of the NLS-GNRs and 9% of the sulfo-SMCC-GNRs. These results are obtained pooling all time points, and their difference is mainly due to the absence of immobile sulfo-SMCC-GNRs at 24 hours, a result probably related to the loss of particles that resided in the cytoplasm. The presence of a significant fraction of immobile GNRs is compatible with our previous results obtained with non-functionalized GNRs (Chapter 3), and might be explained by sticking of GNRs to immobile structures in the cells, like organelles or filaments [19].

The fraction of freely diffusing GNRs is comparable in NLS and control experiments (46% and 53%). The diffusion coefficient we obtained has in both cases a median value of $0.005 \mu\text{m}^2/\text{s}$. This value is about 3 orders of magnitude lower than the expected ones for GNRs of similar size in cells, and it is comparable to our previous findings (see Chapter 3, [14]), in which we observed the same diffusion coefficients both in cytoplasm and nucleus of HeLa cells: hence it cannot be due to internalization into vesicles. We instead hypothesized a reduction in the diffusion due to the presence of obstacles in cell and the stickiness of the PEG-GNRs. This explanation may also be valid for the results presented here for nanorods functionalized with sulfo-SMCC and NLS.

A third population of GNRs shows a motion limited by spatial confinement. This could be explained by internalization of GNRs into vesicles, or by hindered diffusion due to obstacles encountered in the cytoplasm [20]. The range of confinement sizes we obtain is compatible with typical sizes of organelles or free spaces in the cytoplasm. Some large outliers (less than 10%) with confinement sizes from 1 to $10 \mu\text{m}$ are present. We attribute these outliers to free particles with a MSD lower than $0,2 \mu\text{m}^2$, that can hardly be distinguished from confined GNRs.

The study of the fate of functionalized GNRs would benefit from the

possibility to follow the same individual cells over a longer time. Longer traces could then be acquired, allowing for more precise MSD analysis and making it possible to determine the mobility mode of each individual GNR. To follow the same cells over time it is necessary to incorporate an incubator on the two-photon microscope, in order to maintain the cells in the proper growing conditions during the experiments.

The successful translocation of NLS-GNRs is important for the use of GNRs as labels to follow the dynamics of proteins in live cells. In addition, the use of GNRs for targeted-drug delivery and cytotoxicity studies can benefit from better knowledge about translocation into the nucleus.

4.5 Supplementary figures

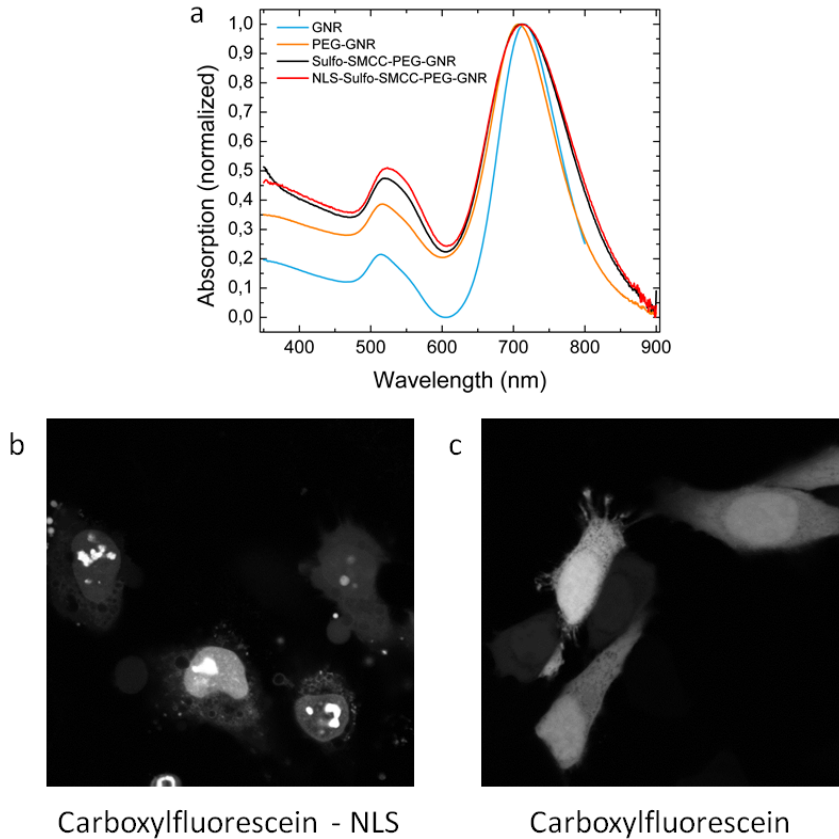
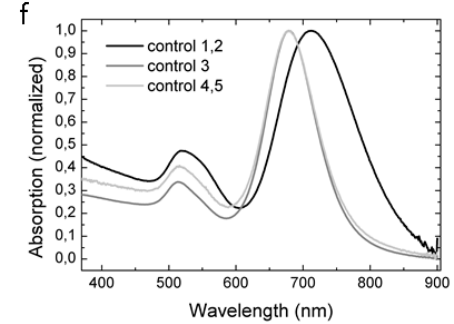
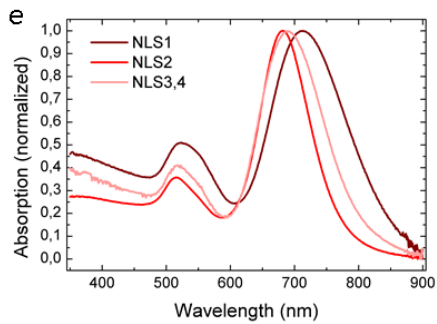
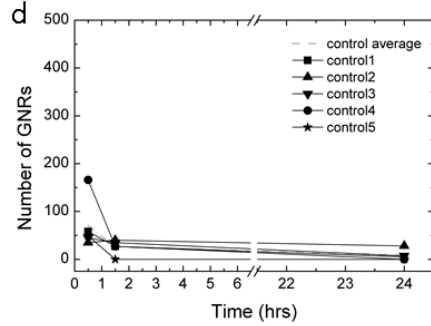
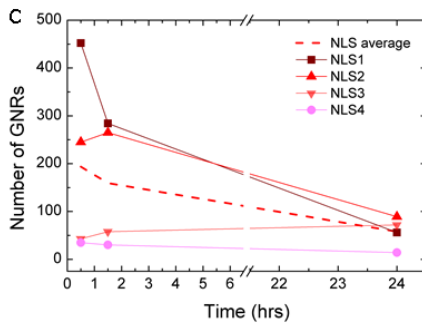
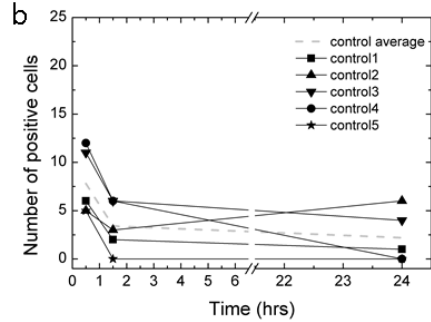
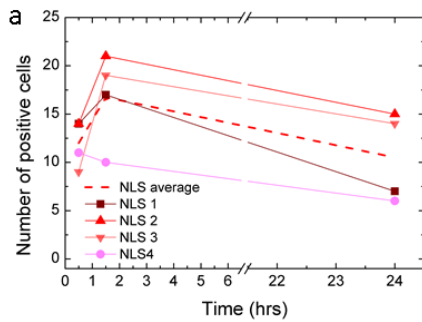


Figure S1

Confirmation of the functionalization of GNRs with sulfo-SMCC and NLS. a) The UV-Vis spectrum of the GNR solution broadens after PEGylation and functionalization with sulfo-SMCC and NLS. Confocal microscope images of HeLa cells injected with b) carboxylfluorescein-NLS and c) only carboxyl-fluorescein show that the NLS peptide induces nuclear translocation, which is absent when only the dye is injected.



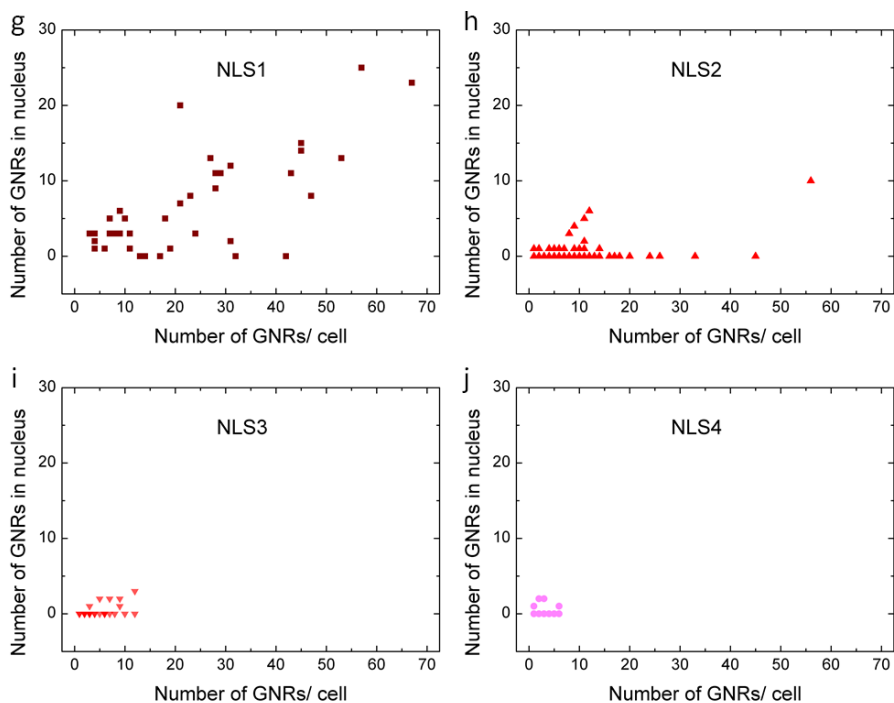


Figure S2

Reproducibility of the injection technique. Number of cells containing GNRs (positive cells) found during a) NLS experiments and b) control experiments. Total number of GNRs found in cells during c) NLS and d) control experiments. UV-Vis spectra of the GNR solutions after functionalization with e) sulfo-SMCC-NLS and f) only sulfo-SMCC. A blue-shift is verified between the sample used for the first and the last experiments. g-j) Number of NLS-GNRs found in cells nuclei in each NLS experiment.

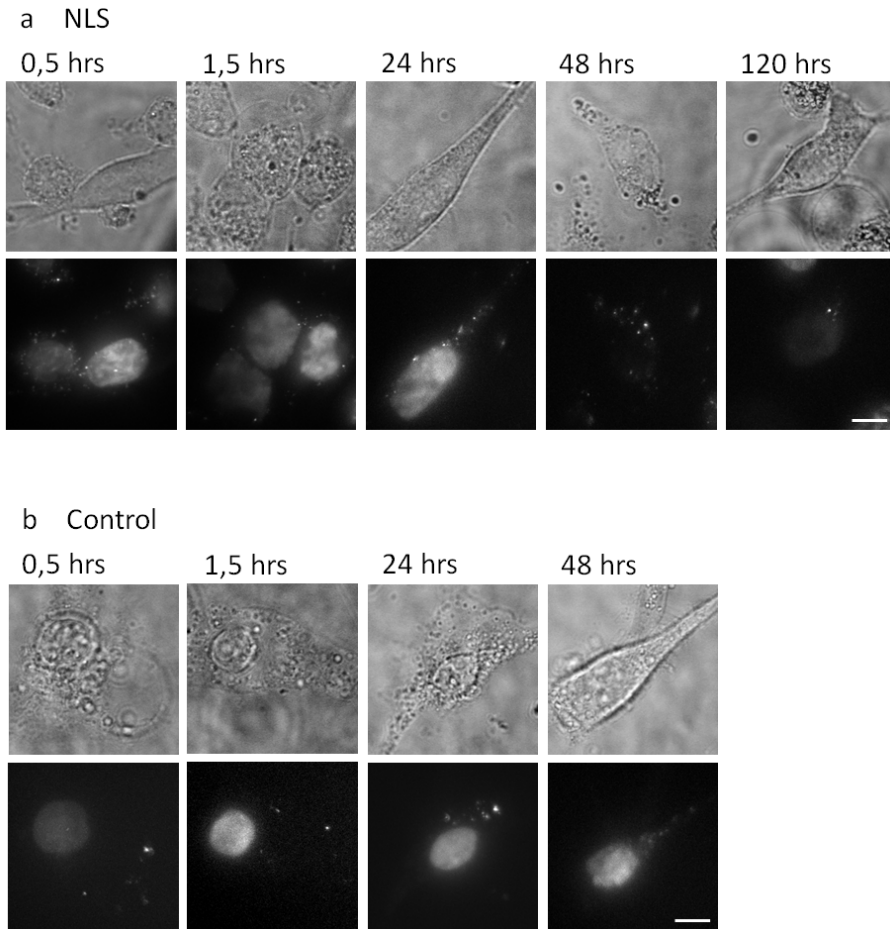


Figure S3

There are variations in the viability of injected cells, however cells with good viability can be found till up to 120 hours after injection with GNRs. Time sequence of transmission and two-photon luminescence images of cells injected with a) NLS-GNRs and b) sulfo-SMCC-GNRs. The size bars are 10 μ m.

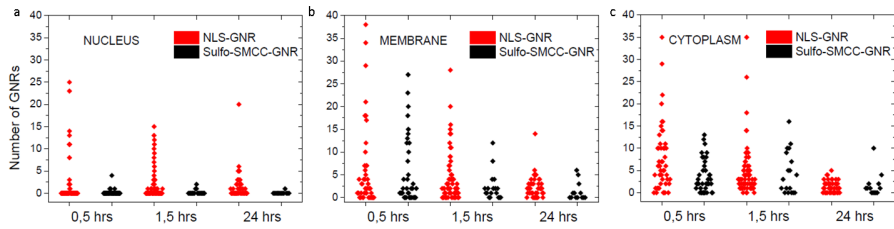


Figure S4

Difference in the distribution of the number of NLS-GNRs and sulfo-SMCC-GNRs per cell over time in each compartment at three time points after injection: in a) nucleus, b) nuclear membrane and c) cytoplasm.

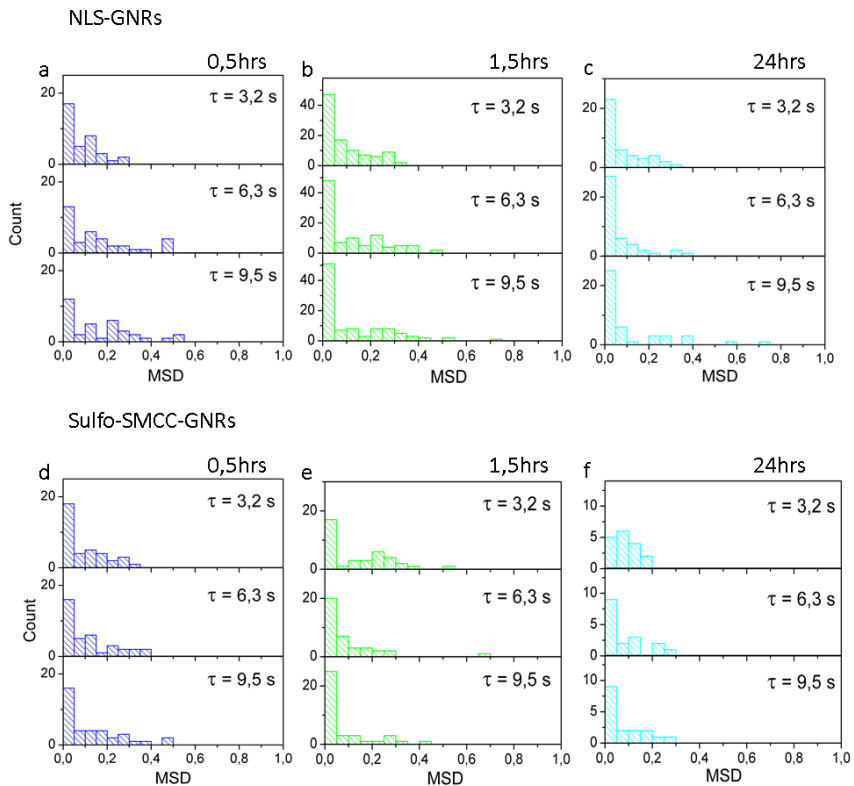
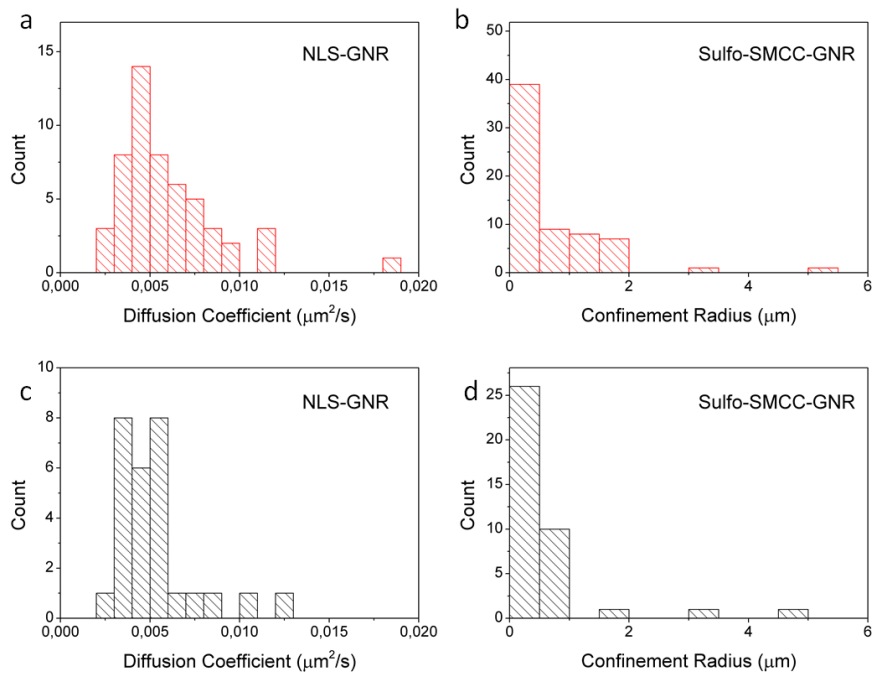


Figure S5

MSD histograms of a-c) NLS-GNRs traces and d-f) sulfo-SMCC-GNRs traces, divided by time after injection.

**Figure S6**

Histograms of diffusion coefficients and confinement sizes for a,b) NLS-GNRs and c,d) sulfo-SMCC-GNRs.

Population	Parameter	NLS-GNR		
		0.5	1.5	24
Immobile	Pop. Size	6; 17%	13; 18%	8; 18%
Confined	Pop. Size	15; 45%	28; 41%	23; 52%
	Confinement (μm)	0.4 (0.2-1.2)	0.4 (0.2-1.2)	0.4 (0.2-1)
Freely Diffusing	Pop. Size	12; 38%	28; 41%	13; 30%
	D ($\mu\text{m}^2/\text{s}$)	0.005 (0.005-0.007)	0.005 (0.004-0.007)	0.006 (0.004-0007)

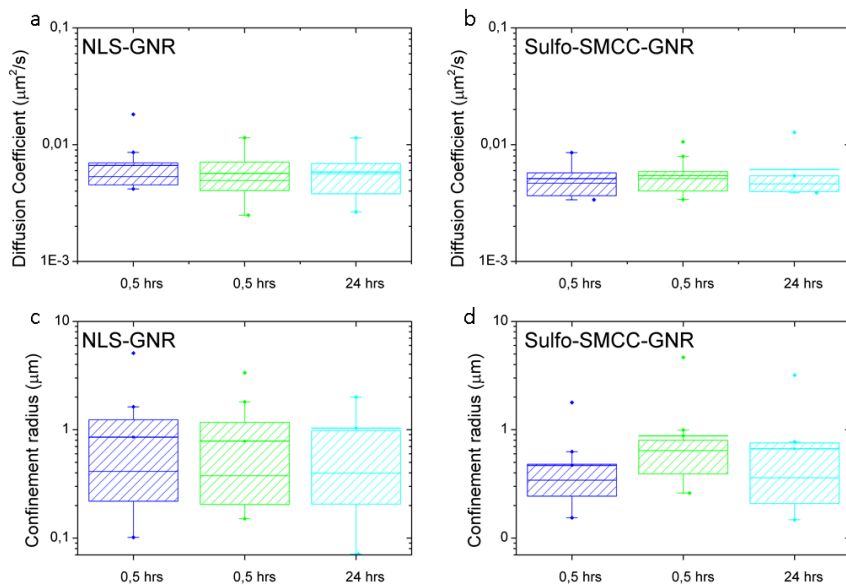
Table S2

Mobility parameters obtained from NLS-GNRs at three different time points after injection. The number of traces corresponding to each population and the relative percentages are reported. The table reports the median, 1st and 3rd quartile of the confinement size of the confined populations, and the median, 1st and 3rd quartile of the diffusion coefficients of the freely diffusing populations.

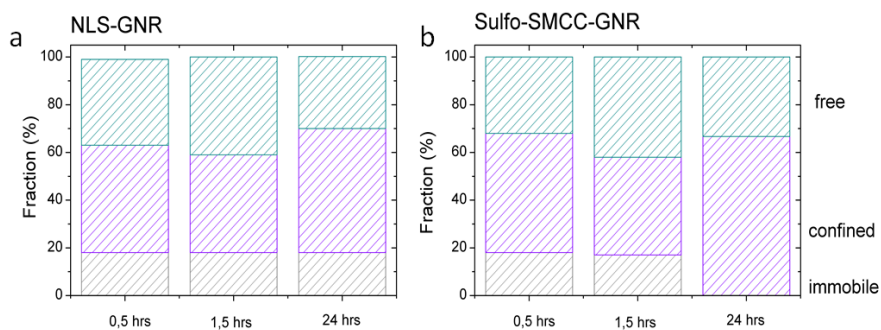
Population	Parameter	sulfo-SMCC-GNR		
		0.5	1.5	24
Immobile	Pop. Size	4; 18%	6; 18%	0
Confined	Pop. Size	11; 50%	14; 41%	10; 67%
	Confinement (μm)	0.3 (0.2-0.5)	0.7 (0.4-0.8)	0.4 (0.2-0.8)
Freely Diffusing	Pop. Size	7; 32%	14; 41%	5; 33%
	D ($\mu\text{m}^2/\text{s}$)	0.005 (0.004-0.006)	0.005 (0.004-0.006)	0.005 (0.004-0005)

Table S3

Mobility parameters obtained from sulfo-SMCC-GNRs at three different time points after injection. The number of traces corresponding to each population and the relative percentages are reported. The table reports the median, 1st and 3rd quartile of the confinement size of the confined populations, and the median, 1st and 3rd quartile of the diffusion coefficients of the freely diffusing populations.

**Figure S7**

Distribution of diffusion coefficients and confinement radii at each time point after injection, for a,c) NLS-GNRs and b,d) sulfo-SMCC-GNR.

**Figure S8**

Percentages relative to each GNR population (immobility, freely diffusing or confined) for a) NLS-GNRs and b) sulfo-SMCC-GNRs, divided by time after injection.

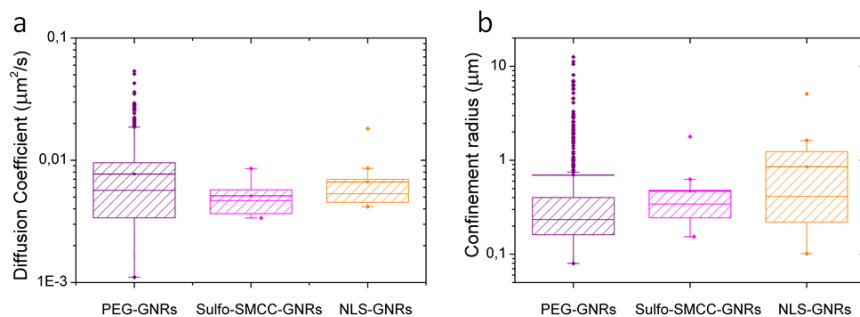


Figure S9

Influence of the functionalization on GNRs mobility. Comparison between the distributions of a) diffusion coefficients and b) confinement radii of PEG-GNRs, PEG-GNRs functionalized with sulfo-SMCC and functionalized with sulfo-SMCC-NLS. The results relative to PEG-GNRs were presented in Chapter 3, Section 3.3.2. In the case of PEG-GNRs, we analyzed the mobility shortly after injection. We compared these results with the ones obtained from sulfo-SMCC-GNRs and NLS-GNRs at 0.5 hours after injection. There are no significant differences in the distributions.

Population	Parameter	PEG-GNR	sulfo-SMCC-GNR	NLS-GNR
Immobile	Pop. Size	125; 13%	4; 18%	6; 18%
Confined	Pop. Size	449; 45%	11; 50%	15; 45%
	Confinement (μm)	0.2 (0.2-0.4)	0.3 (0.2-0.5)	0.4 (0.2-1.2)
Freely Diffusing	Pop. Size	418; 42%	7; 32%	12; 37%
	D (μm ² /s)	0.006 (0.004-0.009)	0.005 (0.004-0.006)	0.005 (0.004-0.007)

Table S4

Mobility parameters obtained from PEG-GNRs, sulfo-SMCC-GNRs and NLS-GNRs, measured 0,5 hours after injection. The table reports the number of traces corresponding to each population and the relative percentages. The median, 1st and 3rd quartile of the confinement sized for the confined populations, and the median, 1st and 3rd quartile of the diffusion coefficients for the freely diffusing populations are reported. The results for PEG-GNRs were presented in Chapter 3, Section 3.3.2.

BIBLIOGRAPHY

- [1] Ning Zhao et al. "Gold nanoparticles for cancer theranostics: A brief update". In: *Sensors and Actuators B*. (2013).
- [2] Mohamed Kodiha et al. "Off to the Organelles: Killing Cancer Cells with Targeted Gold Nanoparticles". In: *Theranostics* 5.4 (2015), pp. 357–370. ISSN: 1838-7640.
- [3] Allison Lange et al. "Classical Nuclear Localization Signals: Definition, Function, and Interaction with Importin Alpha". In: *Journal of Biological Chemistry* (2006).
- [4] Shuaidong Huo et al. "Ultrasmall Gold Nanoparticles as Carriers for Nucleus-Based Gene Therapy Due to Size-Dependent Nuclear Entry". In: *ACS Nano* 8.6 (June 2014), pp. 5852–5862. ISSN: 1936-0851.
- [5] Yan-Juan Gu et al. "Nuclear penetration of surface functionalized gold nanoparticles". In: *Toxicology and Applied Pharmacology* 237.2 (2009), pp. 196–204. ISSN: 0041008X.
- [6] Alexander G Tkachenko et al. "Multifunctional gold nanoparticle-peptide complexes for nuclear targeting." In: *Journal of the American Chemical Society* 125.16 (Apr. 2003), pp. 4700–1. ISSN: 0002-7863.
- [7] Wei Qian et al. "Dark-field light scattering imaging of living cancer cell component from birth through division using bioconjugated gold nanoprobe". In: *Journal of Biomedical Optics* 15.4 (2010), p. 046025. ISSN: 10833668.
- [8] Adegboyega K. Oyelere et al. "Peptide-conjugated gold nanorods for nuclear targeting." In: *Bioconjugate chemistry* 18.5 (2006), pp. 1490–7. ISSN: 1043-1802.
- [9] Wei Xie et al. "Nuclear Targeted Nanoprobe for Single Living Cell Detection by Surface-Enhanced Raman Scattering". In: *Bioconjugate Chemistry* 20.4 (Apr. 2009), pp. 768–773. ISSN: 1043-1802.

- [10] Paola Nativo, Ian Prior, and Mathias Brust. “Uptake and intracellular fate of surface-modified gold nanoparticles.” In: *ACS nano* 2.8 (Aug. 2008), pp. 1639–44. ISSN: 1936-086X.
- [11] Bin Kang, Megan Mackey, and Mostafa A. El-Sayed. “Nuclear Targeting of Gold Nanoparticles in Cancer Cells Induces DNA Damage, Causing Cytokinesis Arrest and Apoptosis”. In: *Journal of the American Chemical Society* 132.5 (Feb. 2010), pp. 1517–1519. ISSN: 0002-7863.
- [12] Megan Mackey and Mostafa El-Sayed. “Chemosensitization of cancer cells via gold nanoparticle-induced cell cycle regulation.” In: *Photochemistry and photobiology* 90.2 (2014), pp. 306–12. ISSN: 1751-1097.
- [13] C. Yang et al. “Peptide modified gold nanoparticles for improved cellular uptake, nuclear transport, and intracellular retention”. In: *Nanoscale* 6.20 (Aug. 2014), pp. 12026–12033. ISSN: 2040-3364.
- [14] Bram van den Broek et al. “Parallel nanometric 3D tracking of intracellular gold nanorods using multifocal two-photon microscopy.” In: *Nano letters* 13.3 (Mar. 2013), pp. 980–6. ISSN: 1530-6992.
- [15] Babak Nikoobakht and Mostafa A. El-Sayed. “Preparation and Growth Mechanism of Gold Nanorods (NRs) Using Seed-Mediated Growth Method”. In: *Chemistry of Materials* 15.10 (May 2003), pp. 1957–1962. ISSN: 0897-4756.
- [16] Nicolas Bogliotti et al. “Optimizing the formation of biocompatible gold nanorods for cancer research: Functionalization, stabilization and purification”. In: *Journal of Colloid and Interface Science* 357.1 (2011), pp. 75–81. ISSN: 00219797.
- [17] Nelly Pante and Michael Kann. “Nuclear pore complex is able to transport macromolecules with diameters of about 39 nm.” In: *Molecular biology of the cell* 13.2 (Feb. 2002), pp. 425–34. ISSN: 1059-1524.
- [18] Zhiqin Chu et al. “Unambiguous observation of shape effects on cellular fate of nanoparticles”. In: *Scientific Reports* 4 (Mar. 2014), pp. 3050–3061. ISSN: 2045-2322.
- [19] Peter H. Hemmerich et al. “Defining the Subcellular Interface of Nanoparticles by Live-Cell Imaging”. In: *PLoS ONE* 8.4 (Apr. 2013). Ed. by Bing Xu, e62018. ISSN: 1932-6203.

- [20] Gernot Guigas and Matthias Weiss. “Sampling the Cell with Anomalous Diffusion-The Discovery of Slowness”. In: *Biophysical Journal* 94.1 (2008), pp. 90–94. ISSN: 00063495.

CHAPTER 5

TWO-PHOTON EXCITATION SPECTROSCOPY OF SINGLE GOLD NANORODS WITH MULTIFOCAL SCANNING MICROSCOPE

Gold nanorods are a promising tool for label-free biosensing, with potential applications in cells. The position of their plasmon spectrum shifts in response to changes in the dielectric constant of the environment, caused for example by the interaction with biomolecules. Using single gold nanorods, the shift in the spectrum peak can be used to detect low concentrations of ligands, down to single-molecule level. Two-photon excitation spectra exhibit narrower peaks than one-photon or scattering spectra, and a peak shift can be measured with higher accuracy. We explored the possibility of acquiring two-photon excitation spectra with our two-photon multifocal scanning microscope. When testing different gold nanorods samples, the spectra showed unexpected complexity, apparently unrelated to the sample features. To explain the origin of such spectra, we first verified the two-photon nature of the excitation produced in the sample. Then, we checked for the presence of gold nanorods clusters using electron microscopy images of the sample. Finally, we characterized the response of different elements in the setup to vari-

Two-Photon Excitation Spectroscopy of Single Gold Nanorods for Sensing Applications, S. Carozza, R. Vlieg, J. van Noort. (in preparation partially based on this chapter).

ations in the excitation wavelength. Our results showed that the modulations in excitation power while scanning the wavelength strongly correlate with the shape of the spectra. We pinpointed the elements in the setup responsible for these modulations, hypothesizing that a back-reflection from these elements enters the laser cavity and compromises the two-photon laser output. The experiments reported here were necessary steps for the future successful acquisition of excitation spectra of gold nanorods.

5.1 Introduction

The plasmon resonance of gold nanoparticles (GNPs) depends on the dielectric constant of the surrounding environment (see Chapter 1, Section 1.3.1). Thanks to this feature, GNPs can be used as label-free sensors: molecules binding to the GNP or in its vicinity can be detected by monitoring the shift in the GNP plasmon resonance. This opens up many opportunities in biomedical and chemical research: depending on their functionalization, GNPs can be used to detect molecules such as proteins and DNA [1–3] or chemicals such as heavy metal ions [4]. Interactions between molecules can also be detected, for example antibody-protein interactions, once the GNP sensor is functionalized with the antibody.

Among GNPs, gold nanorods (GNRs) show a notably high sensitivity to dielectric constant changes [3], [5]. The first bio-sensing experiments using GNRs were performed in bulk [1, 6]. The results, however, were partially obscured by the spectral distribution of the particles in the solution. The use of single GNRs improved the detection limit, down to single-molecule level [7].

The sensitivity of a GNR sensor can be maximized by optimizing the GNR size, aspect ratio [8] and functionalization, for example by limiting it to the GNR tips, where the sensitivity is the highest [5]. High resolution in the measurement of the plasmon spectrum is needed to be able to detect small spectral shifts, when the ligand binds to the GNR. Scattering and absorption spectra of GNRs collected by photothermal microscopy [9, 10] and dark-field spectroscopy [7] have been used for sensing experiments. However, due to the non-linear nature of two-photon (TP) excitation, TP spectra of GNRs exhibit a peak which is about 60% narrower than scattering or one-photon excitation spectra [10]. Therefore, we expect TP excitation spectra of GNRs to offer better spectral sensitivity. To our knowledge, plasmon sensing using GNRs was never performed by TP excitation spectroscopy.

When using single GNRs as sensors, multiplexing is advantageous because it provides high throughput. To combine the advantages of TP with wide field imaging, we developed a two-photon multi-focal scanning microscope. The wavelength of our laser source can be tuned automatically and quickly, which allows for acquiring TP excitation spectra with high temporal and spectral resolution. The wide-field excitation makes it possible to acquire images and spectra of all the GNRs in the field of

view in parallel.

In this chapter we investigated the TP excitation spectra of GNRs with different aspect ratios. The position of the peak in a GNR spectrum is proportional to the aspect ratio. The one-photon excitation spectrum of a GNR has a Lorentzian shape [11], so we expected the TP excitation spectrum of a single GNR to follow a squared Lorentzian shape. However, our spectra show multiple, asymmetric peaks. Therefore, we first investigated whether the unexpected spectral features were due to contaminations in the sample or to clustering of GNRs. Then we carried out a detailed characterization of our setup to check for the presence of undesired modulations of the laser intensity in the excitation path that could generate such spectra.

5.2 Materials and methods

Experimental setup

We used a home-made two-photon multifocal scanning microscope to acquire TP images and excitation spectra. A scheme of the setup is shown in Fig. 5.1. A pulsed IR laser (Chameleon Ultra, Coherent) is used for the excitation, with the possibility of automated tuning of the wavelength. A half-wave plate and a polarizing beam splitter (enclosed by a dashed line in Fig. 5.1) are used to tune the light intensity. A quarter wave plate is used to change the light polarization to circular (WPQ05M, Thorlabs). A long-pass filter (LP692, Semrock) blocks the residual visible light in the excitation beam. A diffractive optical element (DOE, custom-made by Holoeye Photonics) is then used to split the laser beam into an array of 25x25 focal spots. The DOE is optimized in the wavelength range 720-800 nm. The array is then scanned by a fast scanning mirror (FSM-300, Newport), to generate a homogenous illumination on the sample, covering an area of about 60 μm x 60 μm . A short-pass filter (SP720, Semrock) is used to filter the residual excitation light. A photodetector (PDA36A, Thorlabs) placed above the sample stage is used to measure the excitation intensity. The same photodetector is used to measure the beam intensity in other positions in the setup, when needed. The setup is described in more details in Chapter 1, Section 1.2.3.

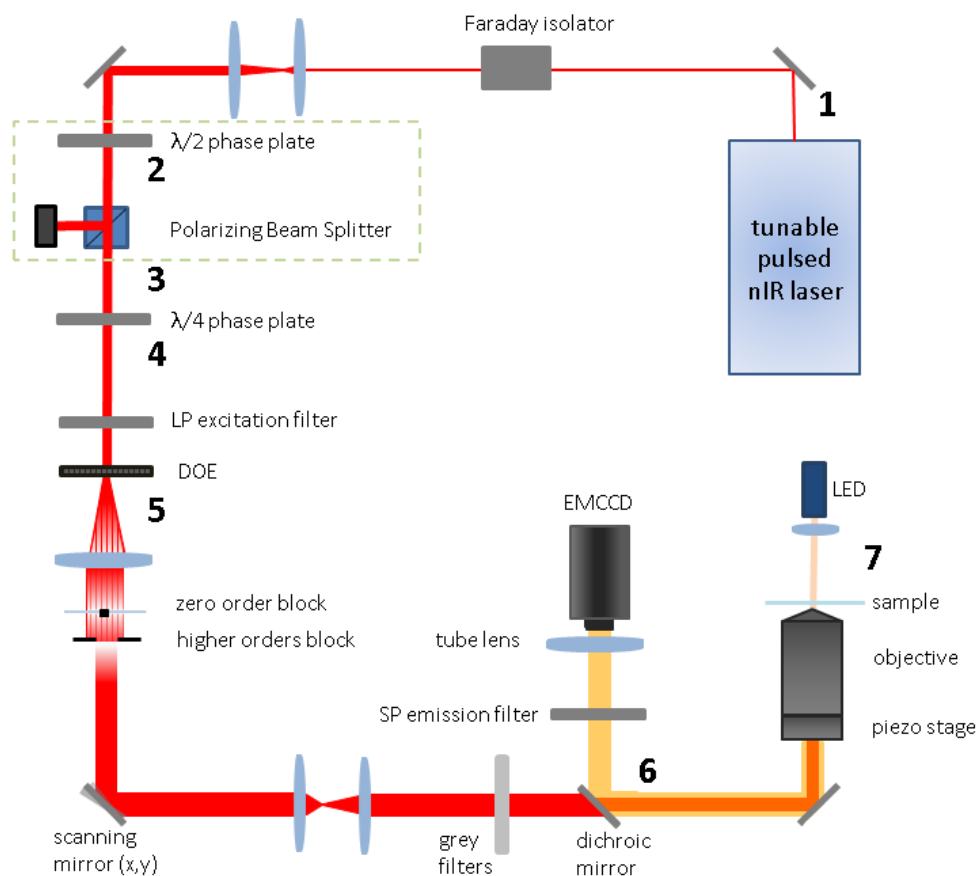


Figure 5.1

Scheme of the two-photon multi-focal scanning setup. Some positions in the setup are marked, and will be referred to in Fig. 5.10.

Sample preparation

Various GNRs samples were used: 780-CTAB, 808-CTAB and 850-CTAB were manufactured by Nanopartz (respectively: A12-25 -780-CTAB, A12-10 -808-CTAB, A12-10 -850-CTAB), 780-PEG and 850-PEG were manufactured by Nanohybrid (78124 and 68630). CTAB (cetyltrimethylammonium bromide) is a surfactant used during seed-mediated synthesis of GNRs. PEG (polyethylene-glycol) is a bio-compatible polymer used to

functionalize GNRs, replacing the CTAB layer.

Samples of GNRs fixed on glass were prepared through the following steps. First, a glass slide was sonicated for 30 minutes in methanol, to remove any pollution from the surface. Then it was sterilized for 30 minutes in a UV-cleaner (Uvo-cleaner, Jelight). To reduce the aggregation between the particles, CTAB-GNRs were diluted in CTAB solution, to adjust the CTAB concentration to 100 μM . The dilution was obtained through a series of (typically 3) dilution and centrifugation steps. The centrifugation was performed at 8000 rpm for 3 minutes. In PEG-GNRs samples, the aggregation was less, thanks to the PEG coating around the particles. After placing a drop of the GNR solution (typically about 30 μl) on the glass slide, the slide was spin-coated in three steps: 200 rpm for 5 seconds, 600 rpm for 15 seconds and 1000 rpm for 60 seconds. The sample was then rinsed gently with demineralized water, dried with a stream of N_2 gas and finally sterilized in the UV-cleaner for 30 minutes. For experiments combining scanning electron microscopy (SEM) or transmission electron microscopy (TEM) and TP imaging, samples were prepared on silicon nitride (SiN) EM grids (home-made as described in [12]), by simply immersing the grid in a GNR solution and drying it with a stream of N_2 gas. To reduce GNRs heating by the laser excitation, a drop of demineralized water was deposited on the slide when performing TP imaging.

TP spectroscopy and imaging with electron microscopes

Spectra were acquired by tuning the laser wavelength while acquiring TP images of the sample. Spectra acquisition and analysis were performed in LabVIEW. The power dependencies were measured by turning a grey filter wheel in the excitation path. UV-Vis spectra were acquired in a UV-Vis spectrophotometer (Cary, Agilent technologies). SEM images were acquired using a NOVA NanoSEM 200 (FEI). TEM images were acquired using a Tecnai 12 TEM (FEI).

5.3 Results and discussion

5.3.1 Excitation spectra of gold nanorods

Fig. 5.2a is a typical image of 780-CTAB GNRs, showing the two-photon signal of all the particles in the field of view. The difference in intensity between GNRs is due to their individual properties: the emission intensity depends both on the particle volume and on the spectral position of the plasmon peak. As we performed experiments with circularly polarized light and we assume the GNRs sticking to the glass slide, the luminescence does not depend on the spatial orientation of the particles. GNRs can form clusters that are brighter than single particles [13]: for this reason, when looking for single GNRs, we ignored very bright and large peaks. The TP excitation spectra of the highlighted particles are displayed in Fig. 5.2b. The different intensities between particles are reflected in the different amplitudes of the peaks in the spectra. We expected spectra with single Lorentzian squared peaks, but in most of the cases the spectra show multiple, asymmetric peaks.

The width of all the peaks is equal or less than 20 nm, as expected for single GNRs according to literature [5]. According to the UV-VIS spectrum of the GNRs sample (Fig. 5.3a), the plasmon peak for this GNR sample is at 750 nm. This position is marked with a blue line in the spectra in Fig. 5.2b: in four cases (GNRs 1, 2, 4, 6) the spectra exhibit a peak in the vicinity.

More spectra from the same sample are shown in Fig. 5.3b. The excitation spectrum and the absorption spectrum of GNRs should overlap, as discussed in Chapter 1, Section 1.3.1. The maximum of the UV-Vis spectrum indicates the position of the plasmon peak, in this case 750 nm (Fig. 5.3a). 10 typical spectra of GNRs in the sample are plotted in Fig. 5.3b. Most of the spectra include multiple peaks, mostly around 760 nm, 790 nm and 830 nm.

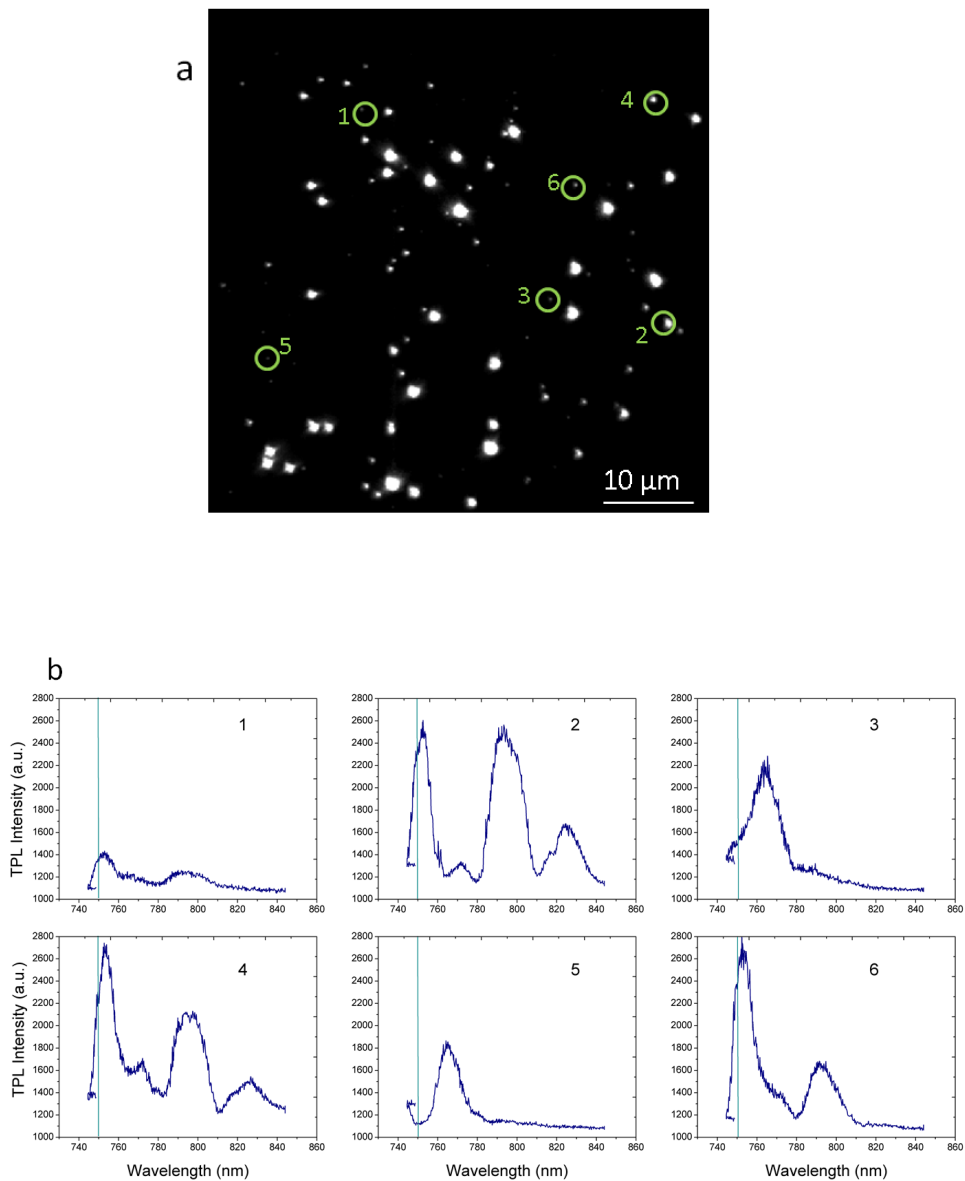
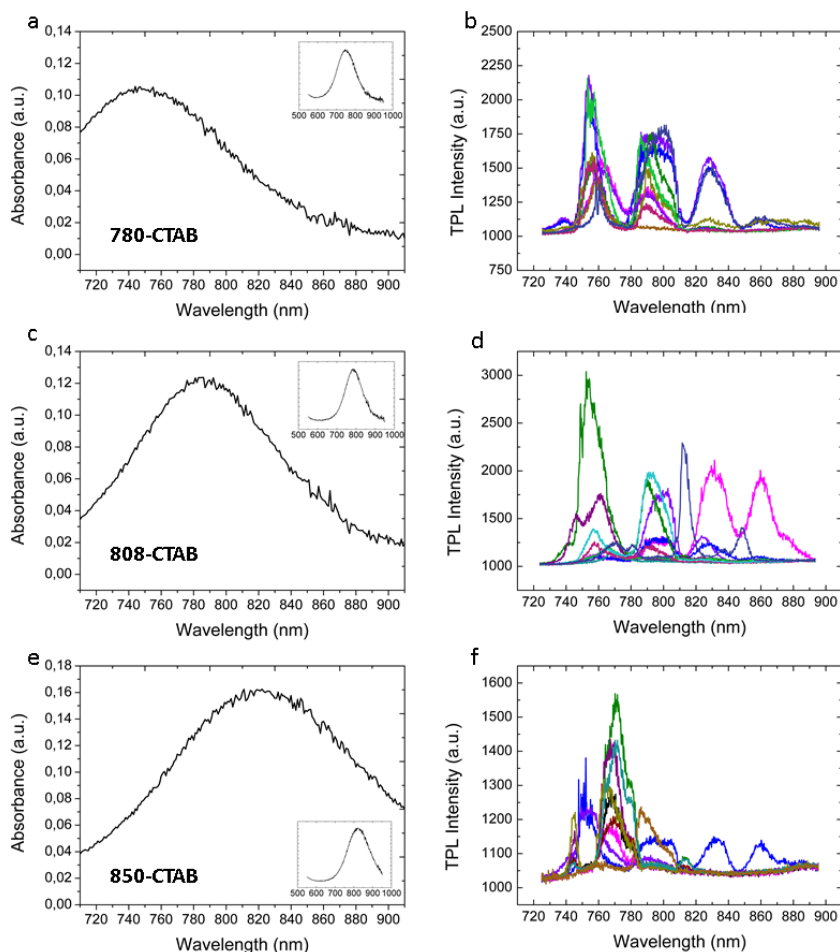


Figure 5.2

A typical TP image and the corresponding excitation spectra of GNRs. a) A TP image of GNRs in a field of view of $60 \mu\text{m} \times 60 \mu\text{m}$. b) Spectra of the GNRs labeled in a). The expected peak position is marked by a blue line in the spectra. The image in a) was acquired at this wavelength (750 nm).

To check whether the unexpected spectral features are characteristic of the 780-CTAB sample, we acquired spectra of different GNRs samples. Fig. 5.3d shows the results obtained using a sample of 808-CTAB GNRs. The plasmon peak of this sample is at 790 nm, as indicated by the UV-Vis spectrum (Fig. 5.3c). Most of the spectra exhibit multiple peaks (Fig. 5.3d), mostly around 770 nm, 800 nm and 820 nm. Similar results were observed using a sample of 850-CTAB GNRs: while we expected a peak at 820 nm (Fig. 5.3e), most of the peaks are around 750 nm and 770 nm (Fig. 5.3f).



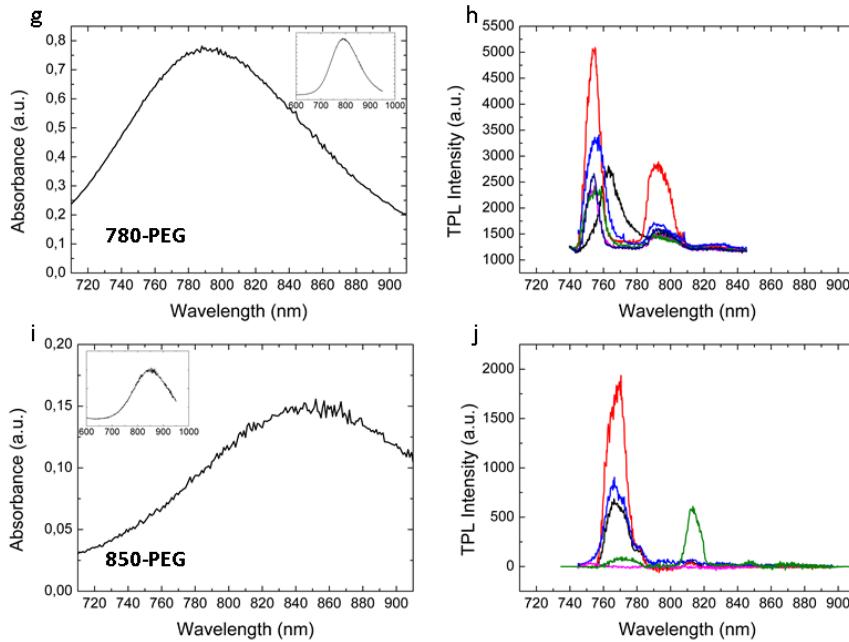


Figure 5.3

Spectroscopy of different GNRs samples: 780-CTAB, 808-CTAB, 850-CTAB, 780-PEG and 850-PEG. a,c,e,g,i) The UV-Vis spectra of the bulk solution indicate the expected peak. The insets show the UV-Vis spectrum from 600 to 1000 nm. b,d,f,h,j) 10 representative TP excitation spectra of GNRs from each sample.

The spectra we obtained do not yield the expected dependence of the plasmon on the aspect ratio of the GNRs. On the contrary, among the three samples a trend in the distribution of the peaks can be noticed: most of the GNRs show three excitation peaks, typically around 760-770 nm, around 800 nm and around 830-860 nm. To find the origin of this discrepancy we tested various hypotheses.

First, we verified whether contaminations in the GNRs sample influenced the spectral features. All three samples were manufactured by Nanopartz and synthesized using CTAB: we therefore analyzed the spectra of two additional samples from a different manufacturer (Nanohybrid), in which the CTAB was replaced with PEG: 780-PEG and 850-PEG. The spectra of these GNRs show similar properties to the previous ones. The UV-Vis spectrum of the 780-PEG GNRs features a peak at

790 nm (Fig. 5.3g), but the single spectra display multiple peaks, including many around 770 nm and 800 nm (Fig. 5.3h). The spectra of 850-PEG GNRs, expected to have a peak at 850 nm (Fig. 5.3i), typically show multiple peaks mostly at 770 and 820 nm (Fig. 5.3j). Hence, we cannot attribute the occurrence of multiple peaks to the presence of CTAB or to the particular production process of a specific batch.

Next, we verified the presence of one-photon emission or scattering light from the GNRs which was not properly blocked by our emission filter. A way to check the nature of the GNR signal is to measure its dependence on the excitation intensity: the emission intensity should follow a quadratic dependence on the excitation intensity. A linear component in the signal will decrease the power dependence of the peak intensity to an exponent closer to 1. We checked the nature of the excitation of GNRs in the 780-CTAB sample, for each wavelength of the spectral peaks: an example is shown in Fig. 5.4. All the three peaks in the spectrum (Fig. 5.4a) exhibit a quadratic dependence on the excitation intensity (Fig. 5.4b, c, d). Moreover, adding an extra emission filter did not remove any of the peaks in the spectra (data not shown). From these results we can exclude the presence of a one-photon excitation or scattering component in the peaks of the spectrum, which could obscure the two-photon luminescence.

We then checked whether the peaks in the spectra are also present in the background signal. The background spectrum of the TP image in Fig. 5.2 is plotted in Fig. 5.5a, together with the spectrum of the GNR number 5 before and after subtraction of the background. The background of our TP images features a weak dependence on the excitation wavelength. The wavelength dependence of the background hardly affects the shape of the spectra. In the rest of this chapter, the background is subtracted from the spectra.

Because of the sharp plasmon peak, we expected little influence of the excitation power profile as the wavelength is scanned. The more so, as the output spectrum of the laser (as provided by Coherent), only features a gradual change over its wavelength range. When we measured the excitation power by putting a photodiode above the sample however, the spectrum showed a noticeable dependence on the excitation wavelength, with peaks at 765 nm, 796 nm and 825 nm (Fig. 5.5b), i.e. at positions comparable to the peaks in the spectra. To account for the differences

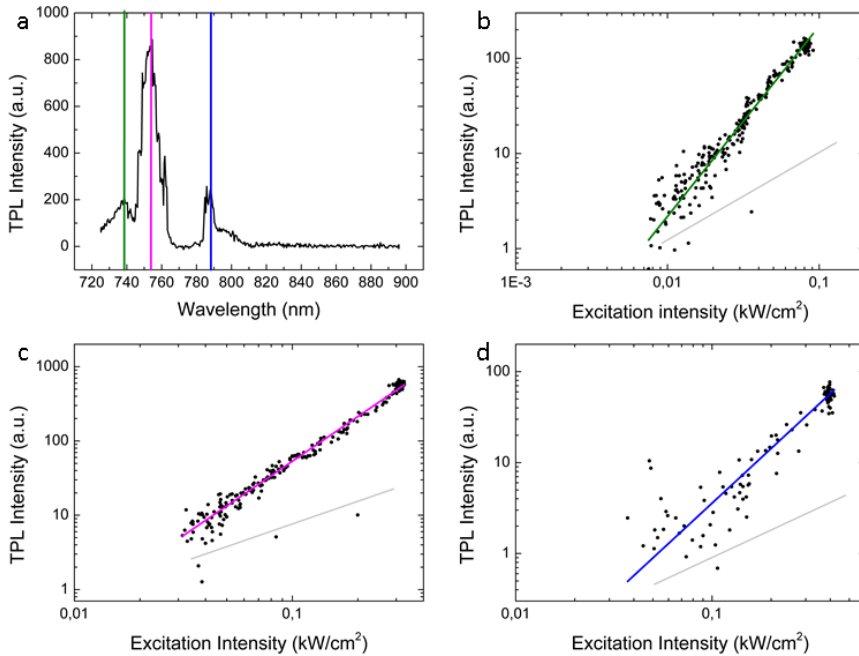


Figure 5.4

Quadratic dependence of the peaks in a GNR spectrum. b-d) The power dependence of all three peaks in a GNR spectrum (a) are analyzed to check the nature of the excitation process. The power dependences have been acquired at the wavelengths highlighted in a). In each case, the colored line indicates the fit with slope 2. For comparison, a line with slope 1 is also depicted in grey in every image.

in excitation power, the emission signal was corrected according to:

$$I_{corrected}(\lambda) = I(\lambda)/(I_{excitation}(\lambda))^2 \quad (5.1)$$

which takes into consideration the non-linear nature of excitation. Nevertheless, correcting the spectra changes their shape only slightly: in Fig. 5.5b and Fig. 5.5c the spectra of GNRs 5 and 4 from Fig. 5.2 are shown, before and after the correction. The three peaks remain, though the intensity is redistributed among the peaks.

The fact that the peaks in the excitation profile partially overlap with the peaks in the GNRs spectra and that these peaks cannot be eliminated by dividing the GNR spectra by the square of the excitation profile suggests a more severe influence of the laser modulation.

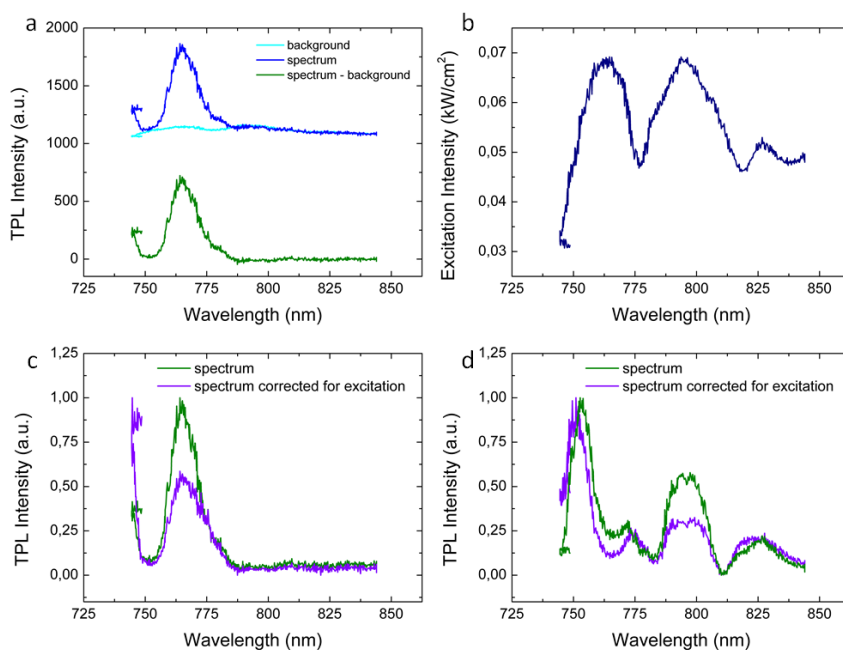


Figure 5.5

The influence of background and excitation intensity profile on GNR spectra. a) Dependence of the background signal on the wavelength and its influence on the spectrum of GNR 5 from Fig. 5.2. The background spectrum (light blue curve) was measured in a part of the sample without GNRs. The original GNR spectrum (blue curve) and the result of the subtraction by the background (green curve) are shown. b) Dependence of the excitation intensity on the wavelength. The excitation profile was measured with a photodetector placed above the sample stage. c,d) Two examples of spectra corrected by the excitation intensity. The spectra correspond to GNR 5 and GNR 4 in Fig. 5.2).

5.3.2 Characterization of gold nanorod samples with electron microscopy

As opposed to single particles, the excitation of GNRs clusters can cause an unpredictable spectral response that depends on the number of particles in the cluster and their spatial arrangement. It was reported that GNRs clusters present multiple and asymmetric spectra [14], similarly to what we observe. A way to directly check for the presence of clusters is to look at the GNRs with an electron microscope. We acquired SEM images of a 780-CTAB GNR sample. We observed a variety of particles configurations, as shown in Fig. 5.6. We zoomed in on 37 particles in different areas of the sample. Half of them were single: 15 GNRs and 3 spheres. There were 19 clusters, among which 6 doublets and 3 made by single GNRs, not connected, but too close to be resolved by optical microscopy. Therefore, even though there are many clusters, the number of single GNRs is large enough to expect some single GNRs spectra.

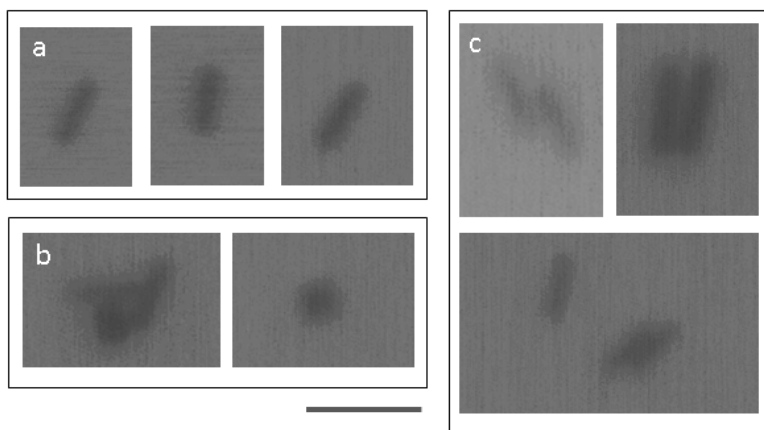


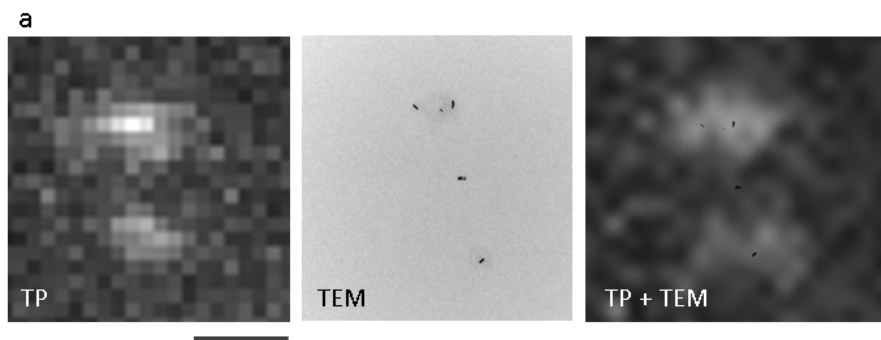
Figure 5.6

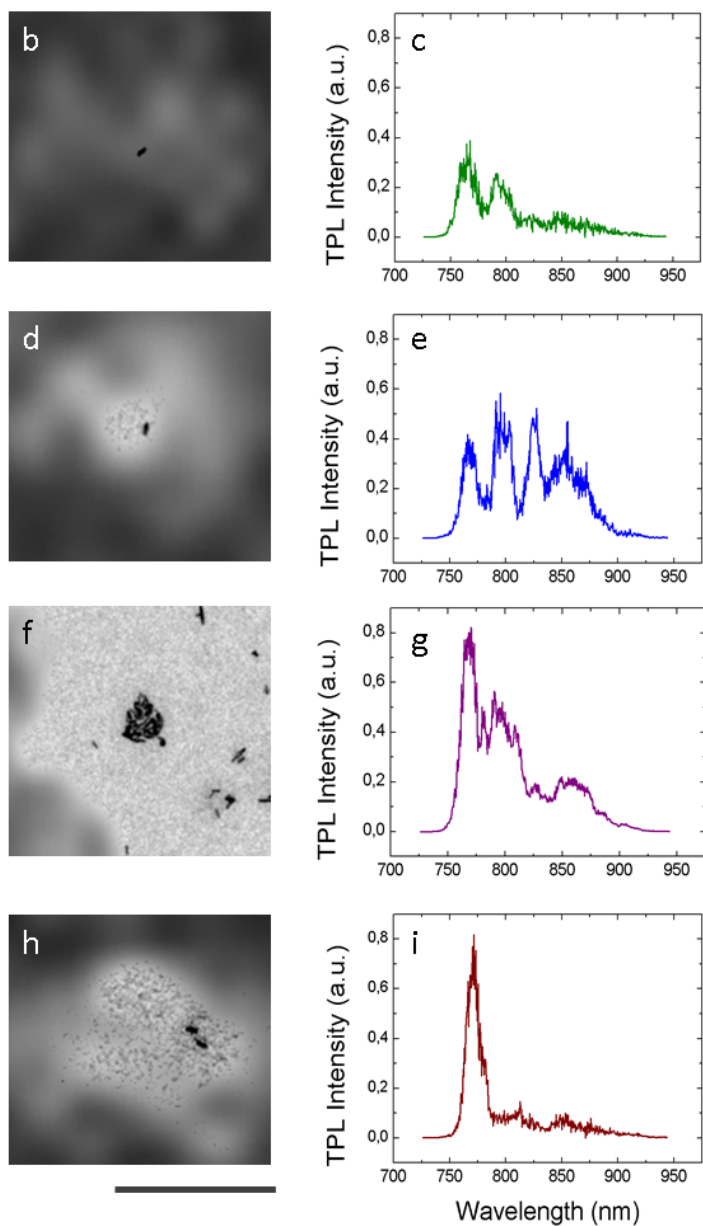
SEM images reveal the composition of a GNR sample. A sample of 780-CTAB GNRs was prepared on a TEM grid. Examples of configurations are shown: a) single GNRs, b) clusters and single spheres, c) GNRs doublets. The size bar corresponds to 50 nm.

The only definitive way to check whether our spectra relate to single GNRs or clusters was to correlate electron microscope images with spectra of the same particles. For this experiment we used a TEM. We first acquired a TP image, together with the excitation spectra of all the GNRs in a marked area in the sample. Then we acquired TEM images of the same area, and we overlapped them to the TP images, as in Fig. 5.7a. The overlapped TEM and TP image of 2 single GNRs are shown in Fig. 5.7b and Fig. 5.7d; the overlapped images of 2 clusters are shown in Fig. 5.7f and Fig. 5.7h. The excitation spectra (Fig. 5.7c,e,g,i) are reported next to these images. No clear difference was found between the spectra of single GNRs and those of clusters, neither in the number of peaks nor in their shape.

Unexpectedly, the most symmetric spectrum (Fig. 5.7l) belongs to a cluster. The spectrum of the second cluster (Fig. 5.7h,i j) is not distinguishable from the spectra of the single particles.

In conclusion, we observed irregular spectra both for single GNRs and clusters. Therefore, such spectra cannot be explained by the presence of GNRs clusters.



**Figure 5.7**

Correlation between TEM images, TP images and spectra. TEM and TP images of the same GNRs from a 780-CTAB sample were acquired. a) Overlap of the TP and TEM images of the same area in the sample. (b-d) Overlap of TEM and TP images of two single particles and (f,h) two clusters, with their excitation spectra in c,e,g,i). The scale bar corresponds to 1 μm .

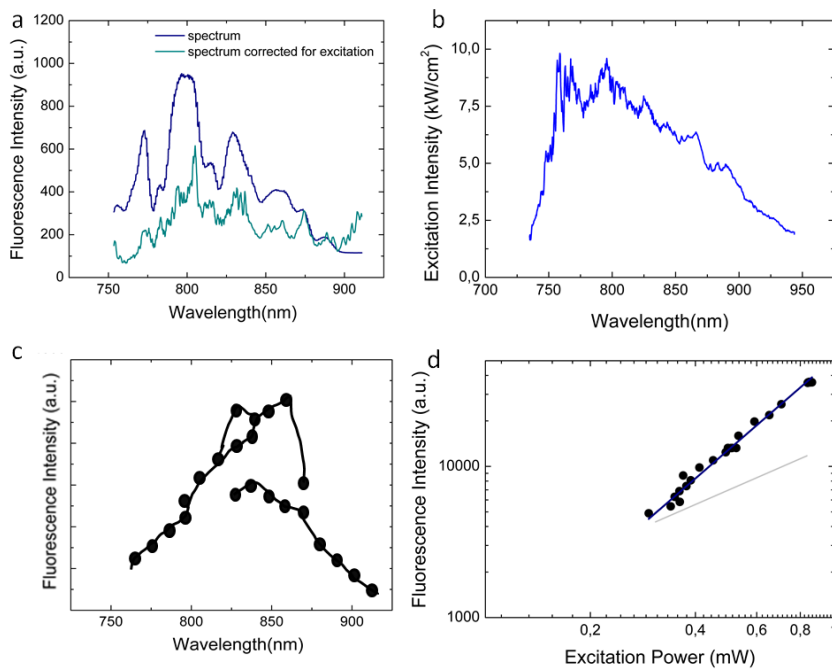


Figure 5.8

Experiments with Rhodamine-B solution. a) TP excitation spectrum of Rhodamine-B in methanol acquired in our setup, before (blue line) and after the correction (cyan line) by the excitation intensity. b) Excitation intensity profile. The expected TP excitation spectrum of Rhodamine-B in methanol follows the excitation cross-section spectrum shown in c, reconstructed from the original figure from [15]. d) Quadratic power dependence of Rhodamine-B in methanol.

5.3.3 Excitation spectrum of Rhodamine-B

As a last check to exclude the sample quality as source of irregularity in the spectra, we measured the spectrum of a homogenous dye solution. The TP excitation spectrum of Rhodamine-B is shown in Fig. 5.8a (blue line). As in the case of GNRs, we obtained multiple peaks that could not be removed by correcting the spectrum by the excitation intensity profile (plotted in Fig. 5.8b). The corrected spectrum is shown in Fig. 5.8a (cyan line). The TP excitation spectrum of Rhodamine-B reported in literature (Fig. 5.8c, a reconstructed detail from the original image from [15],) exhibits also multiple peaks, but in different positions than

the peaks we obtained. The positions of the peaks in our spectrum are comparable to the ones in GNRs spectra: an indication that the spectra hardly reflect the properties of the sample, and is therefore likely to be due only to signal modulations originating in the setup. The quadratic power dependence of TP fluorescence was verified (Fig. 5.8d).

5.3.4 Characterization of the setup

A multi-focus scanning system has not been used before to perform excitation spectroscopy. We therefore verified how scanning the wavelength affects the wide-field illumination. The pattern of focal spots created by the DOE features slightly different sizes and positions at different wavelengths. Fig. 5.9a shows the array of spots at 740, 780 and 890 nm, as measured by imaging the reflected beam on a glass slide. For this experiment, we removed the emission filter. The pattern increases in size when changing the wavelength from 740 nm to 890 nm, and it has a maximum intensity at around 780 nm. Fig. 5.9b shows the intensity profile along the marked line in every image. A misalignment in the x-y plane causes the appearance of the zero order diffraction peak in the center of the pattern (see last figure), that is normally filtered in the excitation path by a zero-order block.

To obtain a wide and homogeneous illumination we scan the focal spot pattern using a spiral function, as described in Chapter 1, Section 1.2.3. The effect of the spiral scanning on the excitation pattern at different wavelengths is shown in Fig. 5.9c. The widening of the pattern at larger wavelengths causes the scanned spirals to be smaller than the distance between the peaks of the diffraction pattern. To check whether this compromises the homogeneity of the excitation, we measured the intensity profile of the pattern along the marked line at different wavelengths (Fig. 5.9d). The homogeneity of the intensity profile changes, but not dramatically, and an adjustment of the amplitude of the spirals can solve this issue.

We measured the distance between focal spots in the plots of Fig. 5.9b, obtaining a value of 3.6 μm at 890 nm, about 0.9 μm larger than at 740 nm (Table S1). We also measured the width of the focal spots: the difference is 0.2 μm between the pattern at 740 and 890 nm. The spiral amplitude we use for our experiment is 2.4 μm . However, changing the amplitude of the scanning spirals does not influence the number, quality

and position of the peaks in a GNR spectrum (Fig. S1).

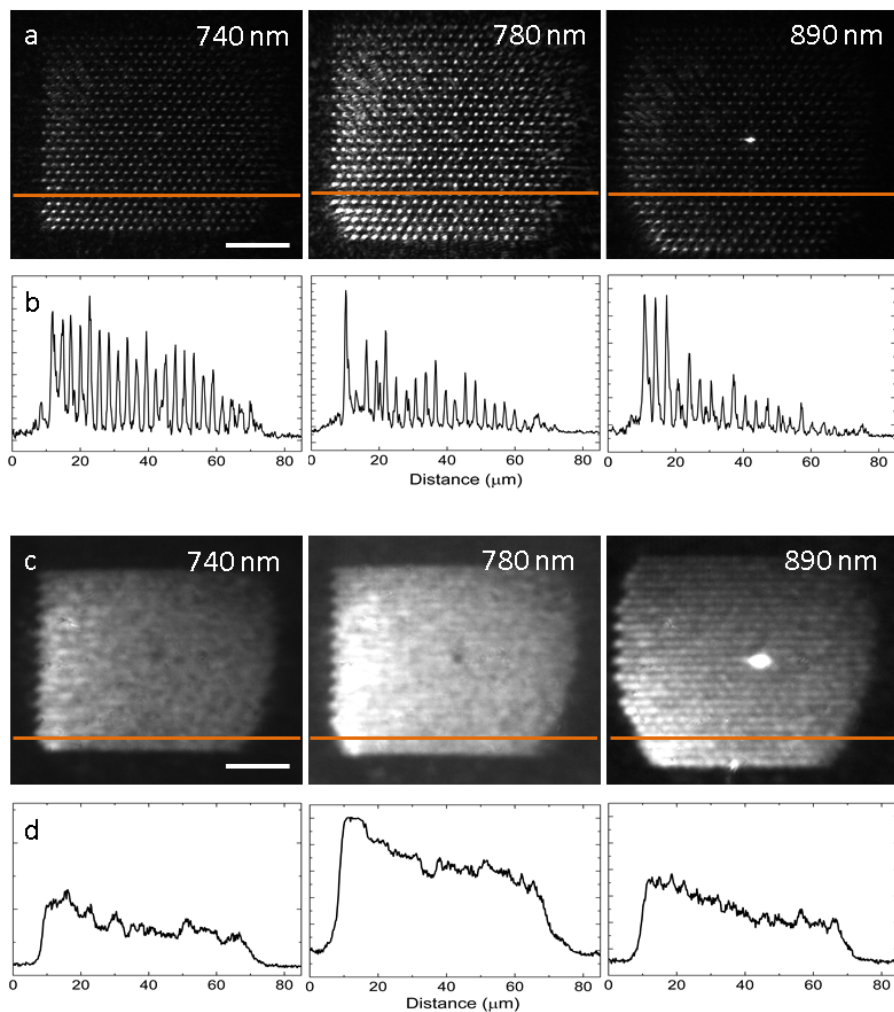


Figure 5.9

Size and homogeneity of the excitation pattern at different wavelengths. a) The array of focal spots generated at different wavelengths. b) Plot of the intensity profile along the marked line in each image. c) The effect of wavelength on the homogeneous pattern created by spiral scanning. d) Intensity profile along the marked line in each image is plotted. In both a and c, a decrease in intensity from right to left can be noticed, due to a slightly tilted position of the DOE. The scale bars are $10 \mu\text{m}$.

When tuning the wavelength, the excitation pattern also moves slightly in the z direction. However, the size of this shift is within the size of our focal spot (around $1\ \mu\text{m}$ in z) and therefore we do not expect it to affect the excitation of the sample. The spectra of the same GNR acquired at different z positions, shown in Fig. S1b, confirm this. Therefore, the multifocal system and the spiral scanning are not responsible for the peaks we observe in the spectra.

To exclude the DOE as one of the causes of artefacts in the spectrum, we tested two different configurations to obtain a wide-field excitation. An alternative method to obtain a pattern of focal spots is to use a micro lens array (MLA) instead than a DOE. However, the spectra obtained with this method showed similar features as obtained with the DOE (Fig. S2). Also using the setup in total internal reflection mode yielded the same results (data not shown).

We finally analyzed how the intensity of the laser light is affected by scanning the wavelength at each component of the setup. In Fig. 5.1 we labeled various locations in the setup. Their corresponding spectra are shown in Fig. 5.10. The spectrum at the laser output (1) shows a quite homogeneous bell-shape, centered at $824\ \text{nm}$. This profile is unmodified till after the polarizing beam splitter (3): here three peaks appear in the profile, around 795 , 825 and $865\ \text{nm}$. The peak at $825\ \text{nm}$ becomes more pronounced after the half-wave plate (4), while modulations appear in the other two peaks. A spectrum with three main peaks at 765 , 795 and $825\ \text{nm}$ is maintained throughout the setup till after the objective (7), while the peak at $865\ \text{nm}$ undergoes some variations. These peaks coincide with the ones we see in most of our spectra. Thus, the polarizing beam splitter and the quarter-wave plate appeared to be responsible for the modulations in the laser intensity.

Later experiments carried out in our group showed a major improvement in the spectra after removing the polarizing beam splitter and the quarter-wave plate. Unfortunately, these experiments were performed after finishing the experimental work presented in this thesis.

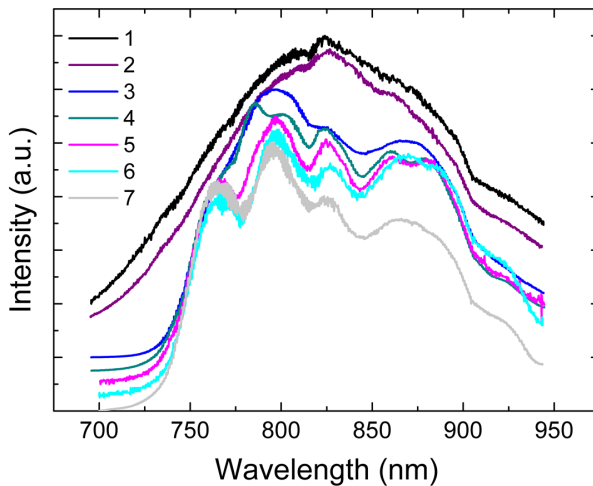


Figure 5.10

Excitation profile transmitted by some elements in the setup. The curves refer to the elements marked with numbers in the setup scheme of Fig. 5.1.

5.4 Conclusion

Using a multifocus scanning TP microscope, we acquired GNRs spectra that exhibited multiple unexpected, asymmetric peaks. These peaks were found for GNRs with different aspect ratios, and therefore do not represent the characteristics of the GNRs in the sample.

Multiple and asymmetric peaks in GNRs spectra were previously observed as a consequence of Fano-resonance, a result of the interference between resonances modes in the particle [16]: however the Fano spectra had different shape than the spectra we observe. Furthermore, this phenomenon was observed only for long GNRs deposited on substrates with a large dielectric constant, and not on glass [17]: Fano resonance therefore cannot explain our spectra.

We tested several other hypotheses on the origin of these peaks in the excitation spectra:

1. signal from a contamination present in the GNR samples;
2. one-photon luminescence or scattering signal from the GNRs;
3. signal emitted by clusters of GNRs;

4. artifacts caused by one or more elements in the setup.

We tested the first hypothesis by performing experiments on samples of PEG-GNRs produced by a different manufacturer, but the spectra exhibited the same features.

We observed modulations in the excitation intensity spectrum that could be amplified by the non-linear character of the TP excitation. However, corrections by dividing the GNR spectra by the square of the excitation intensity was not enough to yield a single, sharp spectrum. This correction could fail if the emission resulted from a mixture of one-photon and two-photon excitation processes. Nevertheless, all peaks featured a quadratic dependence on excitation power: the two photon signal was therefore not mixed with a linear component. The excitation profile we used for our correction was measured above the sample and it could be an inaccurate approximation of the actual excitation profile in the sample. Thermal reshaping of the GNRs could also induce an unstable, broadened spectrum. However, the similarities in the spectra obtained from GNRs with different aspect ratio and the partial overlap of the spectra with the excitation profile are likely to exclude these two hypotheses. The presence of clusters as the reason for the observed spectra was excluded by correlating TP spectra with TEM images of the same GNRs.

The spectrum of Rhodamine-B solution showed spectral features similar to those of GNRs, confirming that these features can not to be attributed to the sample but they originate in the setup.

We therefore performed a detailed characterization of our setup when scanning the wavelength. We first investigated how the wavelength scanning affects the spatial homogeneity of the illumination. Changing the wavelength slightly affected the size of the excitation pattern, but this did not influence the shape of the spectra.

We then analyzed how the spectral excitation intensity modulation developed through the optical path. We checked the spectrum at every component in the excitation path and identified the components where first the peaks appear: the polarizing beam splitter used to control the laser intensity and the quarter-wave plate used to change the light polarization. In our group it was later shown that removing these elements eliminated the unexpected peaks in the GNRs spectra.

The reason why removing the elements responsible for the modula-

tions improved the spectra but correcting the spectra for the square of the modulation profile did not, is not straightforward. We hypothesize that a backreflection, originating from these elements for some specific wavelengths, entered the laser cavity and compromised the quality of the laser beam. We checked the beam intensity at the laser output, but not the pulse width nor the mode and how these parameters were influenced by the presence of the polarization optics. During future spectral measurements these parameters should be accurately monitored. We used a broadband Faraday isolator to filter the backreflections, but we could not find details on its efficiency within the spectral range we use. Moreover, the efficiency of the isolator depends on the polarization of the beam, hence the reflected light coming from the polarizing optics may not be blocked properly. The polarizing beam splitter and the half-wave plate were removed from the setup, but they could be useful in the future to automatically tune the excitation intensity and to acquire circular polarized spectra of the GNRs. The proposed checks should then be carried out, to be able to eliminate the modulations produced by these elements.

A laser intensity modulator might be used to reduce the modulations introduced by the optics. Also an analysis of the transmission of the elements along the emission path may be carried out, to verify whether additional modulations are introduced along the emission path. This check can be done placing a white light source instead of the laser and analyzing the transmissivity of each element in the path. Alternatively, each element might be taken out of the setup and into a spectrometer for proper characterization.

In conclusion, the experiments we presented here, including EM characterization of the GNRs sample to check for single particles and a detailed analysis of the setup response to wavelength scanning, were a necessary step for successful spectroscopy experiments. We localized the elements in the setup where the unexpected peaks in the spectra originated, and removing them brought major improvements. When new experiments show sharp and narrow peaks of single GNRs, it will be possible to explore the potential that TP excitation spectra offer for biosensing applications.

5.5 Supplementary figures

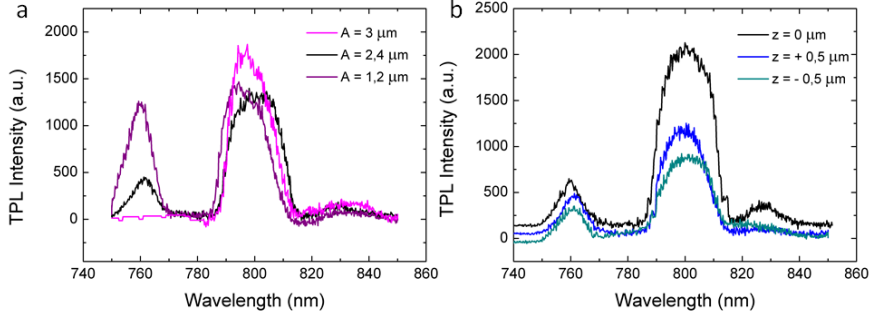


Figure S1

a) TP excitation spectra of a GNR acquired with different amplitude of the scanning spirals. The number and shape of the peaks in the spectra is not influenced by the scanning amplitude. The initial flat part in the curve with $A=0.3 \mu\text{m}$ is due to a laser problem, not to the amplitude of the spirals. In b) the spectra of the same GNRs are acquired at different heights: in focus ($z = 0 \mu\text{m}$), and $0.5 \mu\text{m}$ above or below the focus.

Wavelength (nm)	Distance between spots (μm)	Spot width (μm)
740	2.7 ± 0.1	0.7 ± 0.1
780	3.1 ± 0.03	0.7 ± 0.1
890	3.6 ± 0.4	0.9 ± 0.02

Table S1

Distance between spots and spots widths measured along the lines in Fig. 5.9.

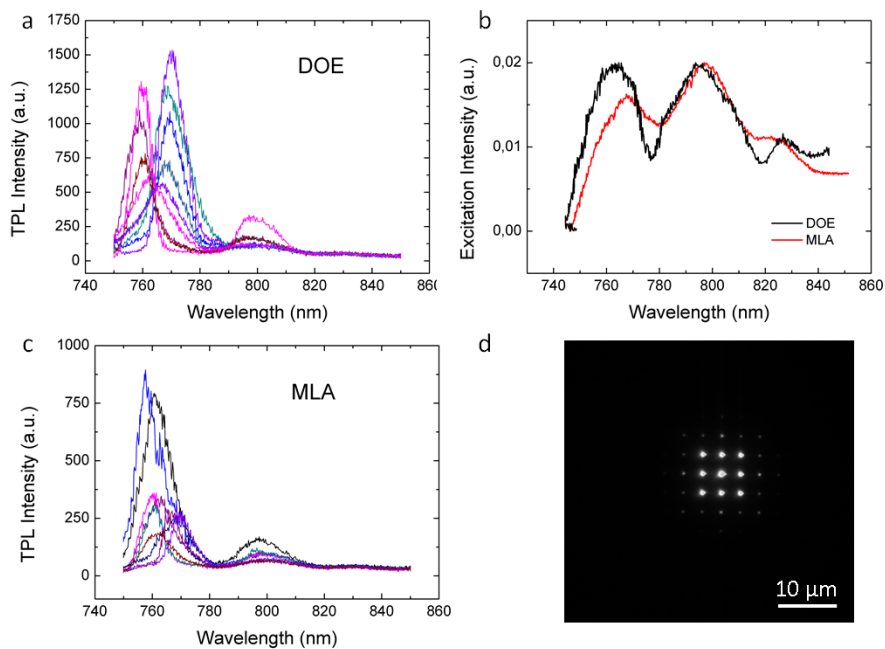


Figure S2

Difference between spectra acquired with a DOE and with a microlens array (MLA). Spectra of 780-CTAB samples were measured using a) a DOE and c) a MLA for the excitation. In the two cases, the GNRs are not the same particles. b) Comparison of the excitation intensity profiles produced by the DOE and by the MLA, as measured above the sample. d) Pattern of excitation produced by the MLA.

BIBLIOGRAPHY

- [1] Cheng-Dah Chen et al. "Sensing capability of the localized surface plasmon resonance of gold nanorods." In: *Biosensors & bioelectronics* 22.6 (Jan. 2007), pp. 926–32. ISSN: 0956-5663.
- [2] Nguyen Thi Kim Thanh and Zeev Rosenzweig. "Development of an Aggregation-Based Immunoassay for Anti-Protein A Using Gold Nanoparticles". In: *Analytical Chemistry* 74.7 (Apr. 2002), pp. 1624–1628. ISSN: 0003-2700.
- [3] Shuwen Zeng et al. "A Review on Functionalized Gold Nanoparticles for Biosensing Applications". en. In: *Plasmonics* 6.3 (Apr. 2011), pp. 491–506. ISSN: 1557-1955.
- [4] Gopala Krishna Darbha et al. "Selective detection of mercury (II) ion using nonlinear optical properties of gold nanoparticles." In: *Journal of the American Chemical Society* 130.25 (June 2008), pp. 8038–43. ISSN: 1520-5126.
- [5] P Zijlstra and M Orrit. "Single metal nanoparticles: optical detection, spectroscopy and applications". en. In: *Reports on Progress in Physics* 74.10 (Oct. 2011), p. 106401. ISSN: 0034-4885.
- [6] Nidhi Nath and Ashutosh Chilkoti. "A Colorimetric Gold Nanoparticle Sensor To Interrogate Biomolecular Interactions in Real Time on a Surface". In: *Analytical Chemistry* 74.3 (Feb. 2002), pp. 504–509. ISSN: 0003-2700.
- [7] Irene Ament et al. "Single unlabeled protein detection on individual plasmonic nanoparticles." In: *Nano letters* 12.2 (Feb. 2012), pp. 1092–5. ISSN: 1530-6992.
- [8] Kyeong-Seok Lee and Mostafa A El-Sayed. "Gold and silver nanoparticles in sensing and imaging: sensitivity of plasmon response to size, shape, and metal composition." In: *The journal of physical chemistry. B* 110.39 (Oct. 2006), pp. 19220–5. ISSN: 1520-6106.

- [9] Michael A Beuwer, Menno W J Prins, and Peter Zijlstra. “Stochastic Protein Interactions Monitored by Hundreds of Single-Molecule Plasmonic Biosensors.” In: *Nano letters* 15.5 (Apr. 2015), pp. 3507–3511. ISSN: 1530-6992.
- [10] Peter Zijlstra, James W M Chon, and Min Gu. “Five-dimensional optical recording mediated by surface plasmons in gold nanorods.” In: *Nature* 459.7245 (May 2009), pp. 410–3. ISSN: 1476-4687.
- [11] Carolina Novo et al. “Contributions from radiation damping and surface scattering to the linewidth of the longitudinal plasmon band of gold nanorods: a single particle study”. en. In: *Physical Chemistry Chemical Physics* 8.30 (July 2006), p. 3540. ISSN: 1463-9076.
- [12] Roman I. Koning, Gert T. Oostergetel, and Alain Brisson. “Preparation of flat carbon support films”. In: *Ultramicroscopy* 94.3-4 (Apr. 2003), pp. 183–191. ISSN: 03043991.
- [13] Babak Nikoobakht and Mostafa A. El-Sayed. “Preparation and Growth Mechanism of Gold Nanorods (NRs) Using Seed-Mediated Growth Method”. In: *Chemistry of Materials* 15.10 (May 2003), pp. 1957–1962. ISSN: 0897-4756.
- [14] Alison M Funston et al. “Plasmon coupling of gold nanorods at short distances and in different geometries.” In: *Nano letters* 9.4 (Apr. 2009), pp. 1651–8. ISSN: 1530-6992.
- [15] Chris Xu and Watt W. Webb. “Measurement of two-photon excitation cross sections of molecular fluorophores with data from 690 to 1050 nm”. In: *Journal of the Optical Society of America B* 13.3 (Mar. 1996), p. 481. ISSN: 0740-3224.
- [16] F López-Tejeira et al. “Fano-like interference of plasmon resonances at a single rod-shaped nanoantenna”. en. In: *New Journal of Physics* 14.2 (Feb. 2012), p. 023035. ISSN: 1367-2630.
- [17] Huanjun Chen et al. “Observation of the Fano resonance in gold nanorods supported on high-dielectric-constant substrates.” In: *ACS nano* 5.8 (Aug. 2011), pp. 6754–63. ISSN: 1936-086X.

SUMMARY

Biomolecular processes occurring inside cells are the basis of life for all organisms, and regulate growth, diseases and death. The main protagonists of these processes are proteins and nucleic acids. When advances in microscopy techniques made it possible to follow single biomolecules during cellular processes, many new insights in life were gained that were unimaginable with ensemble techniques. To perform single-molecule microscopy, biomolecules such as proteins must be functionalized with a suitable optical label. Metal nanoparticles were proposed as promising labels, due to their brightness and photostability as compared to traditionally used fluorescent proteins and dyes. Among nanoparticles, gold nanorods are often preferred, because they can be easily functionalized and they can be excited with low energy photons. In addition, the spectral response of gold nanorods depends on the dielectric constant of their immediate surroundings. This property makes them useful as sensors: measuring the spectrum of gold nanorods can reveal interactions with biomolecules.

In this thesis, we explored the use of gold nanorods as labels for single-particle tracking in live cells and tested the acquisition of excitation spectra of single gold nanorods for sensing applications. We took advantage of two-photon excitation of gold nanorods: non-linear excitation provides a better image contrast and therefore a higher 3-dimensional accuracy, as well as the possibility to use low-energy light, with consequently lower photodamage of cells. Moreover, two-photon excitation spectra are narrower than one-photon spectra, and they therefore provide a more sensitive spectral response. We used a multifocal scanning microscope to perform 3D imaging inside cells with nanometer positional accuracy.

When performing single-particle tracking, mean squared displacement analysis is the most common method to obtain mobility infor-

mation from trajectories of tracked particles, such as the diffusion coefficient. The precision of the diffusion coefficient sets a limit to discriminate changes in mobility, caused by biological events, from the statistical variation inherent to diffusion. This issue is therefore of particular importance in experiments aiming to quantify dynamic processes. In **Chapter 2** we presented simulations and 3D tracking experiments *in vitro*, using gold nanorods freely diffusing in glycerol solution, to establish the best analysis parameters to extract the diffusion coefficient. We applied this knowledge to the detection of a temporary change in diffusion, as it can occur due to the transient binding of a protein to an immobile structure within the cell. The simulations showed that the spatial accuracy of the particle tracking generally does not limit the detection of such binding events. However, changes in mobility can only be detected reliably when they last for a sufficient number of frames.

Having established the possibilities and limitations of single-particle tracking of gold nanorods *in vitro*, a next step is to move *in vivo*. In **Chapter 3** we tested delivery of gold nanorods in live cells with different techniques: incubation, electroporation, cell-squeezing and single-cell microinjection in HeLa cells and COS1 cells. We also tested injection in the yolk of zebrafish embryo cells. For each technique we evaluated the delivery efficiency and the short-term consequences for cell viability. When the delivery of gold nanorods was successful, we analyzed their mobility by mean squared displacement analysis. We found three populations of nanorods: immobile, freely diffusing and diffusing within a confinement. In zebrafish embryo cells all the mobile rods were freely diffusing. In HeLa cells the diffusing rods were about 50% and in COS1 cells about 70% of the total. The diffusion coefficients were around $0.006 \mu\text{m}^2/\text{s}$, lower than the expected values for unrestricted diffusion, but compatible with our previous findings. The confinement radius was around $0.3 \mu\text{m}$. The mobility parameters we obtained were the same in cytoplasm and nucleus of HeLa cells.

Functionalization of gold nanorods is a necessary step for targeted delivery and for their use as labels to follow selected proteins in cells. **Chapter 4** describes the functionalization of gold nanorods with nuclear localization signal. These peptides signal transport of biomolecules to the cell nucleus. Single-cell microinjection was used to deliver gold

nanorods in live HeLa cells. The efficiency of microinjection showed some variability between experiments and influenced the nuclear targeting results. Nevertheless, we observed a significant increase of nuclear localization of gold nanorods when functionalized with the nuclear localization signal. The nuclear targeting efficiency was around 15%, and was probably limited by the size of the particles. We noticed clearance of gold nanorods from the cytoplasm over time, for both functionalized and non-functionalized particles. The mobility of gold nanorods did not depend on their functionalization. Overall, these experiments showed that gold nanorods functionalization with nuclear localization signal can be used for nuclear targeting, but only with a small yield.

When performing a single-particle tracking experiment, the possibility to verify whether the particles are bound to the biomolecules of interest can be of great help. Gold nanorods have sensing capabilities that are particularly precious for this aim. The position of their plasmon spectrum shifts in response to changes in the dielectric constant of the environment, caused for example by the interaction with biomolecules. Using single gold nanorods, the shift in the spectrum peak can be used to detect low concentrations of ligands, down to the single-molecule level. Two-photon excitation spectra have been shown to exhibit narrower peaks than one-photon or scattering spectra, and a peak shift can be measured with higher accuracy. In **Chapter 5** we explored the possibility to perform two-photon excitation spectroscopy with our multifocal scanning microscope, testing different gold nanorod samples. The spectra showed unexpected complexity, apparently unrelated to the sample features. To explain the origin of such spectra, we first verified the two-photon nature of the excitation produced in the sample. Then, we checked for the presence of gold nanorod clusters, by correlating the spectra to electron microscopy images of the sample. Finally, we characterized the response of different elements in the setup to variations in the excitation wavelength. Our results showed that the modulations in excitation power, while scanning the wavelength, strongly correlate with the shape of the spectra. We pinpointed the origin of these modulations to some elements in the setup. By removing these elements we could later obtain spectra of single gold nanorods.

The use of gold nanorods for *in vivo* single-particle tracking proved

to be challenging, mainly due to the large size of the particles and their stickiness before and after functionalization. In our work, we chose particles with sizes ranging from 10 nm x 40 nm to about 20 nm x 60 nm to favor high brightness and consequently high localization and tracking accuracy. This choice brought the disadvantage of slower diffusion and less efficient nuclear targeting when functionalized with nuclear localization signal peptides. However, we observed an increased stickiness for nanorods of smaller sizes. To fully exploit the promises of gold nanorods, a better compromise must be reached between size and brightness. To this aim, it would be interesting to study the fate of gold nanorods in cells as a function of their size.

Nevertheless, our results are encouraging. Efficient delivery of gold nanorods inside living cells was obtained through single-cell microinjection, electroporation and injection in the yolk of zebrafish embryo cells, with limited effect on cell viability. The mobility results that we obtained for gold nanorods in different cells were comparable, but quite different from the mobility we observed in glycerol. Successful functionalization of gold nanorods with nuclear localization signal peptides was proved by nuclear localization. Moreover, we illustrated the possibility to detect changes of mobility within gold nanorod traces and established the limitations of such analysis.

The successful delivery and functionalization of gold nanorods are the first steps to a number of possible experiments inside living cells. Nanometer-accuracy single-particle tracking of gold nanorods functionalized with proteins may give detailed insight into the dynamics of proteins. For example, gold nanorods can be functionalized to bind to nuclear proteins or to specific DNA sequences to follow protein-DNA interactions in the cell nucleus for longer time and with higher spatial resolution compared to other labels. Conjugation of gold nanorods to transcription factors (such as the glucocorticoid receptor) could reveal new mechanistic details of transcription regulation and on the fate of the receptor after this process. Gold nanorods bound to DNA sequences could also be used to study chromatin condensation.

The high potential of two-photon microscopy of gold nanorods must be further investigated before it can be used for sensing experiments. We encountered challenges in acquiring spectra of single gold nanorods, due to imperfect spectral properties of our setup. Recently, removing the polarization elements in the setup yielded better spectra. With this

advancement, the spectra of single gold nanorods may prove to be sensitive to the interaction with molecules. This opens up new possibilities, such as single-molecule sensing in live cells.

SAMENVATTING

Aan de basis van het leven van elk organisme staan biomoleculaire processen die groei, ziekte en dood reguleren. De belangrijkste spelers in deze processen zijn eiwitten en nucleïnezuren. Met de uitvinding van microscopie-technieken die het mogelijk maken om individuele biomoleculen tijdens cellulaire processen te volgen, zijn vele biologische inzichten verworven die verscholen gaan in bulkmetingen. Om individuele biomoleculen, zoals eiwitten, te kunnen volgen, moeten ze worden gefunctionaliseerd met een geschikt optisch label. Metalen nanodeeltjes zijn veelbelovende labels, omdat hun helderheid en fotostabiliteit aanzienlijk beter zijn dan die van traditionele fluorescente eiwitten en labels. Gouden nanostaafjes zijn extra aantrekkelijk, omdat ze gemakkelijk kunnen worden gefunctionaliseerd. Daarnaast hangt de spectrale respons van gouden nanostaafjes af van de elektrische permittiviteit van hun omgeving. Deze eigenschap maakt ze nuttig als sensoren: door de spectra van gouden nanostaafjes te meten kunnen interacties met biomoleculen worden gedetecteerd.

In dit proefschrift hebben we de bruikbaarheid van gouden nanostaafjes onderzocht als labels voor het volgen van individuele deeltjes in levende cellen, en van hun spectra voor toepassing van de staafjes als sensoren. We hebben gebruik gemaakt van de twee-foton-excitatie van gouden nanostaafjes: deze niet-lineaire excitatie biedt een hoger contrast en daarmee een grotere driedimensionale nauwkeurigheid, alsmede de mogelijkheid om laag-energetisch licht te gebruiken, hetgeen minder schade aan de cellen oplevert. Bovendien zijn twee-fotonspectra minder breed dan één-fotonspectra, en bieden ze dus een gevoeliger spectrale respons. We hebben gebruik gemaakt van een multifocale scanning microscoop om in 3D, tot op nanometer nauwkeurig, afbeeldingen van cellen te maken.

Bij het volgen van individuele deeltjes is de meestgebruikte methode om mobiliteitsinformatie, zoals diffusiecoëfficiënten, uit de trajecten van deeltjes af te leiden, een analyse van de gemiddelde gekwadraterde verplaatsing. De precisie waarmee de diffusiecoëfficiënt kan worden bepaald stelt een limiet aan het vermogen om veranderingen in mobiliteit, als gevolg van biologische gebeurtenissen, te onderscheiden van de statistische fluctuaties inherent aan diffusie. Deze precisie is daarom van groot belang in experimenten die dynamische biologische processen kwantificeren. In **Hoofdstuk 2** presenteren we simulaties en in vitro experimenten aan gouden nanostaafjes die vrij konden diffunderen in een glycerol-oplossing. Hiermee hebben we de meest gunstige analyse-parameters vastgesteld voor het meten van de diffusiecoëfficiënt. Deze hebben we toegepast om tijdelijke veranderingen in de diffusiesnelheid te detecteren, welke bijvoorbeeld plaatsvinden wanneer eiwitten zich tijdelijk binden aan een onbeweeglijke structuur in een cel. De simulaties lieten zien dat de nauwkeurigheid die we kunnen bereiken bij het volgen van deeltjes over het algemeen niet beperkend is voor het detecteren van dergelijke gebeurtenissen. Veranderingen in mobiliteit kunnen echter alleen worden gedetecteerd als hun tijdsduur een voldoende aantal opvolgende afbeeldingen bestrijkt.

Nadat we de mogelijkheden en de beperkingen van het volgen van gouden nanostaafjes in vitro hadden vastgesteld, konden we de stap naar in vivo maken. In **Hoofdstuk 3** hebben we het inbrengen van gouden nanostaafjes in levende cellen getest met verschillende methoden: incubatie, electroporatie, cell-squeezing en microinjectie, in HeLa-cellen en COS1-cellen. Ook hebben we injectie getest in de dooierzak van zebravisembryo's. Voor elk van deze technieken hebben we de efficiëntie van het inbrengen van de deeltjes en de kortetermijnconsequenties voor de levensvatbaarheid van de cellen geëvalueerd.

Wanneer het inbrengen van de gouden nanostaafjes succesvol was, hebben we hun mobiliteit gemeten via analyse van de gemiddelde gekwadraterde verplaatsing. We vonden drie populaties van nanostaafjes: onbeweeglijk, vrij diffunderend en diffunderend binnen een beperkt gebied. In de embryonale cellen van zebravissen waren alle diffunderende staafjes vrij. In HeLa-cellen was ongeveer 50% van de diffunderende staafjes vrij, en in COS1-cellen ongeveer 70%. De diffusiecoëfficiënten lagen rond $0.006 \mu\text{m}^2/\text{s}$. Dit is lager dan verwacht voor vrije diffusie,

maar in overeenstemming met onze voorgaande bevindingen. De staafjes die beperkt diffundeerden deden dit in een gebied met een straal van ongeveer $0.3 \mu\text{m}$. De mobiliteitsparameters waren gelijk in het cytoplasma en in de celkern van HeLa-cellen.

Om de gouden nanostaafjes op de juiste plaats te krijgen en om ze als labels te kunnen gebruiken om specifieke eiwitten te volgen, is het nodig om ze te functionaliseren. **Hoofdstuk 4** beschrijft het functionaliseren van gouden nanostaafjes met een nucleair lokalisatiesignaal. Dit is een peptide die aangeeft dat een biomolecuul naar de celkern moet worden getransporteerd. De gouden nanostaafjes werden via microinjectie in levende HeLa-cellen geïnjecteerd. De efficiëntie van de microinjectie vertoonde variabiliteit tussen verschillende experimenten en had invloed op het succes van de nucleaire lokalisatie. We zagen desondanks een significante toename van gouden nanostaafjes in de celkern wanneer deze waren gefunctionaliseerd met een nucleair lokalisatiesignaal. Ongeveer 15% van de deeltjes bereikten de celkern; dit percentage werd waarschijnlijk gelimiteerd door de grootte van de nanostaafjes. Ook zagen we dat de gouden nanostaafjes uit het cytoplasma verdwenen naarmate de tijd verstreek, ongeacht of ze waren gefunctionaliseerd of niet. Tenslotte bleek de mobiliteit van de deeltjes niet af te hangen van de functionalisatie. Samengevat lieten deze experimenten zien dat het functionaliseren van gouden nanostaafjes met een nucleair lokalisatiesignaal kan worden gebruikt om de deeltjes naar de celkern te laten vervoeren, maar slechts met beperkt rendement.

In experimenten waarbij men individuele deeltjes wil volgen, is het erg nuttig om te kunnen verifiëren dat de deeltjes aan de juiste biomoleculen zijn gebonden. Gouden nanostaafjes zijn hiervoor waardevol omdat ze van zichzelf sensoren zijn: hun plasmonspectrum verschuift wanneer de elektrische permittiviteit van de omgeving verandert, bijvoorbeeld vanwege interacties met biomoleculen. De verschuiving in het spectrum van individuele gouden nanostaafjes kan worden gebruikt om lage concentraties van een ligand te detecteren, tot een enkel molecuul aan toe. Twee-fotonspectra hebben smallere resonantiepieken dan één-foton- of verstrooiingsspectra, waardoor een piekverschuiving met grotere nauwkeurigheid kan worden gemeten. In **Hoofdstuk 5** hebben we de mogelijkheid onderzocht om spectroscopie met twee-foton-excitatie uit te

voeren met onze multifocale scanning microscoop, waarbij we verschillende soorten gouden nanostaafjes hebben getest. De spectra vertoonden onverwachte complexiteit, schijnbaar ongerelateerd aan de eigenschappen van de gouden nanostaafjes. Om de oorsprong van deze spectra te achterhalen, hebben we eerst geverifieerd dat de excitatie in de monsters inderdaad ten gevolge van de absorptie van twee fotonen was. Vervolgens hebben we gecontroleerd of de nanostaafjes clusters vormden, door de spectra met elektronenmicroscopische afbeeldingen van de monsters te correleren. Tenslotte hebben we de respons van verschillende elementen in de opstelling op variaties in de excitatiegolflengte gekarakteriseerd. Onze resultaten lieten zien dat het vermogen van de excitatie tijdens het doorlopen van het spectrum sterke correlatie vertoonde met de vorm van het spectrum. We konden de oorsprong van deze modulatie herleiden tot enkele componenten in de opstelling. Door deze componenten te verwijderen konden we uiteindelijk de spectra meten van individuele gouden nanostaafjes.

Het is een grote uitdaging gebleken om gouden nanostaafjes te gebruiken om in vivo deeltjes te volgen, voornamelijk vanwege de grootte van de staafjes en hun clustering zowel voor als na het functionaliseren. In onze experimenten hebben we voor nanostaafjes gekozen met afmetingen van 10 nm x 40 nm tot ongeveer 20 nm x 60 nm. Een kleinere omvang gaat ten koste van de helderheid van de deeltjes en de daarvan afhankelijke nauwkeurigheid in het lokaliseren en volgen ervan. Nadelen van deze keuze zijn de lage diffusiesnelheden en een laag rendement van het nucleair lokalisatiesignaal. We zagen echter ook een verhoogde clustering van nanostaafjes met kleinere afmetingen. Om de gouden nanostaafjes optimaal te benutten is een betere balans tussen de grootte van de deeltjes en hun helderheid nodig. Met dit doel voor ogen zou het interessant zijn om te onderzoeken wat er met gouden nanostaafjes in cellen gebeurt als functie van hun afmetingen.

Ondanks de hierboven beschreven uitdagingen, zijn onze resultaten bemoedigend. We hebben gouden nanostaafjes efficiënt in levende cellen kunnen inbrengen via microinjectie, electroporatie en injectie in de dooierzak van het zebrafish-embryo, met beperkt effect op de levensvatbaarheid van de cellen. De mobiliteit van de gouden nanostaafjes was vergelijkbaar in verschillende soorten cellen, maar significant verschillend van het resultaat in glycerol. Ook hebben we het succesvol func-

tionaliseren van gouden nanostaafjes met een nucleair lokalisatiesignaal gedemonstreerd. Bovendien hebben we laten zien dat het mogelijk is om veranderingen in de mobiliteit van gouden nanostaafjes te detecteren, en hebben we de beperkingen van een dergelijke analyse vastgesteld.

Het succesvol inbrengen en functionaliseren van gouden nanostaafjes is de eerste stap om meer geavanceerde experimenten in levende cellen mogelijk te maken. Het op de nanometer nauwkeurig volgen van nanodeeltjes gefunctionaliseerd met eiwitten zou gedetailleerd inzicht in de dynamica van deze eiwitten kunnen geven. Gouden nanostaafjes zouden bijvoorbeeld kunnen worden gefunctionaliseerd om zich te binden aan nucleaire eiwitten of specifieke DNA-sequenties. Zo zouden de interacties tussen eiwitten en DNA in de celkern kunnen worden gevolgd voor een langere tijdsduur en met een grotere ruimtelijke nauwkeurigheid dan mogelijk is met andere labels. Ook zouden met gouden nanostaafjes die zich aan transcriptiefactoren (zoals de glucocorticoid receptor) binden, nieuwe mechanistische details kunnen worden onthuld van transcriptieregulatie, en van wat er na dit proces met de transcriptiefactor gebeurt. Ook zou de mogelijkheid om gouden nanostaafjes te binden aan specifieke DNA-sequenties kunnen worden gebruikt om het condenseren van chromatine te bestuderen.

Het potentieel van twee-fotonmicroscopie met gouden nanostaafjes zal verder moeten worden onderzocht voordat de methode kan worden toegepast bij het gebruik van de staafjes als sensoren. We stuiten bij het meten van de spectra van individuele gouden nanostaafjes op de imperfecte spectrale respons van onze opstelling. Recentelijk hebben we de spectra beter kunnen meten door elementen uit de opstelling te verwijderen. Dit biedt de mogelijkheid de spectra te gebruiken om interacties van de nanostaafjes met moleculen te detecteren. Dit zou nieuwe mogelijkheden aanboren, zoals het detecteren van individuele moleculen in levende cellen.

LIST OF PUBLICATIONS

1. "Accuracy of the Detection of Binding Events Using 3D Single-Particle Tracking"
S.Carozza, J. Culkin, J. van Noort
BMC Biophysics 10(3), (2017)
2. "Single-Particle Tracking of Gold Nanorods in Live Cells"
S.Carozza¹, V.I.P. Keizer¹, A. Boyle¹, A. Kros, M. Schaaf, J. van Noort
in preparation
3. "Two-Photon Excitation Spectroscopy of Single Gold Nanorods for Sensing Applications"
S.Carozza¹, R.Vlieg¹, J. van Noort
in preparation

¹ These authors contributed equally to this work

CURRICULUM VITAE

Sara Carozza was born on October 10th, 1987 in Bergamo, Italy. She studied Physics at Università degli Studi di Milano-Bicocca from 2006 to 2011, specializing in Biophysics. She joined the group of Prof. Giuseppe Chirico for both her bachelor's and master's thesis. Her bachelor's thesis was focused on the characterization of gold nanorods and the study of their diffusion using fluorescence correlation spectroscopy. For her master's thesis she studied the emission of a mutant fluorescent protein under varying pH conditions in cellular environment, for pH sensing and imaging applications. In 2012 she joined the group of Dr. ir. John van Noort at Leiden University as a PhD student. In her PhD project she worked on the application of two-photon luminescence of gold nanorods for single-particle imaging and tracking in vitro and in live cells. During her PhD, she was teaching assistant in a bachelor LabVIEW class for 3 years and supervised a master student during his thesis project. She presented her work at several conferences in the Netherlands, Germany and US. Currently, she is working as Data Scientist at Anchormen where she is involved in a project at Friesland Campina.

ACKNOWLEDGEMENTS

I would like to thank John van Noort for trusting me and inviting me to join the Physics of Life Processes group. With his support, knowledge and enthusiasm he guided me through my projects, helping me to see the opportunities beyond the obstacles.

Many thanks to our collaborators Marcel Schaaf, Michel Orrit, Alexander Kros, Peter Zijlstra and Aquiles Carattino for the helpful discussions, interesting insights and new ideas. Without Aimee Boyle's expertise in chemistry and Veer Keizer's in biology, most of this work wouldn't have been possible. Aimee synthesized and functionalized the gold nanorods used for most experiments. Veer prepared and took care of the cells and helped during the imaging experiments and the analysis.

I would like to thank post-doc Jeremie Capoulade, who helped improving the setup and shared with me his deep knowledge of optics. Thanks to master student Jamie Culkin for his hard work on simulations, and to my successor Redmar Vlieg for helping with the acquisition of spectra and of EM images.

The colleagues in the Physics of Life Processes group enriched me as a researcher thanks to their ideas, critical minds and helpfulness. They were great colleagues inside the office, and wonderful friends outside. Thanks to Lena, Wietzke, Meng, Wim, Hedde, Olga, Stefano, Artur, Rolf, Thomas, Kirsten, Babette, Klas, Ruth, Dominique, Maria, Nelli, Joeri, Noemi, Patrick, Kate, Doris, Stefan, and to our neighbors Emrah, Mihela, Marija and Saptaswa. I am grateful to Thomas Schmidt for his assistance and for the precious discussions, and to Sylvie Olthuis and Ineke de Boer for their technical support. A special thanks to Yvonne Kerkhof, who kindly helped me in all the bureaucracy matters.

Thanks to Marco Tompitak and Veer Keizer for the Dutch translation of the summary of this thesis.

Last but not least, I would like to thank my parents and Marco for their endless love and support during this important part of my life.

